JUSTUS-LIEBIG-
UNIVERSITÄT
GIESSEN

An *ab initio* approach to spin transport in magnetic tunnel junctions with disorder

Eine *ab initio* Betrachtung von Spintransport in magnetischen Tunnelkontakten mit Unordnung

DISSERTATION

submitted for the degree of

Doctor rerum naturalium
Doktors der Naturwissenschaften

by

Dipl.-Phys. Christian Franz

Supervisor: Prof. Dr. Christian Heiliger
AG Theoretische Festkörperphysik

I. Physikalisches Institut
Justus-Liebig-Universität Gießen

Gießen, December 2015

Contents

1 Introduction – Spintronics

The topic of this thesis is centered in the research and technology field of *spintronics*[1] [143, 138, 118]. In conventional electronics, only the charge of electrons is used, whereas their spin is disregarded. In contrast, in magnetism the spin is utilized via the magnetization e.g. to store information; however, here only stationary (equilibrium) electrons are relevant [50]. Spintronics (spin-transport electronics), on the other hand, specifically employs the spin of transport (non-equilibrium) electrons to gather, transport, and manipulate information. This additional degree of freedom offers potential for new or improved functionalities, ranging from simple magnetic field sensors to spin-based logic devices and even quantum computing. While the former are widely used in applications, the more advanced concepts are an active field of basic and applied research. In this section we give a brief overview of spintronics to outline the context of the present topic and its relevance for other areas of the field; for more details we refer to the literature [50, 10, 9, 131, 125, 65].

Designing a spintronic device naturally requires some effect coupling to the electron spin. This may be e.g. exchange coupling in an (anti-)ferromagnet, an external magnetic field, or spin-orbit interaction. This effect fixes a spin quantization direction and leads to different equilibrium and transport properties for spin-up and spin-down electrons[2]. It is often useful to describe these systems in terms of two separate spin channels conducting in parallel (two-current model), which have different properties and are weakly coupled by spin mixing (spin-flip scattering) [47]. This can lead to unequal currents in both channels, i.e. a net spin(-polarized) current, which is a central quantity in spintronics. It may also lead to different non-equilibrium occupations for both spins called a spin accumulation. The length scale on which a spin polarization or accumulation can persist is called spin-diffusion length and gives an upper limit for many spintronic effects. Some devices, however, are based on quantum-mechanical effects and thus restricted to the shorter mean free path.

Early studies investigated spin-dependent resistance in bulk ferromagnetic materials, i.e. different resistances in both spin channels [47]. In contrast, magnetoresistive effects describe a dependence of the total resistance of a device on an external magnetic field or the magnetic configuration. Anisotropic magnetoresistance caused by spin-orbit coupling in a single ferromagnetic layer has been discovered long before the spin itself [129] and is used for magnetic field sensors. The development of methods to create thin layers (e.g. molecular beam epitaxy) enabled to investigate magnetoresistive effects in multilayer systems [47], which show a much larger effect (i.e. relative change in the resistance). This led to the discovery of giant magnetoresistance (GMR) [47]. In the simplest case, a GMR structure consists of two ferromagnetic layers separated by a non-magnetic metal layer. Resistances measured along the layers as well as perpendicular both show a dependence on the relative orientation of the two magnetizations. Usually, the resistance is largest when both magnetizations are anti-parallel to each other. The GMR effect can be understood from spin-dependent resistance in the ferromagnets and at the interfaces [47].

Even larger (tunnel) magnetoresistance (TMR) [60] can be obtained in magnetic tunnel junctions (MTJ) [154], where the ferromagnetic layers are separated by a thin insulating layer and electrons need to tunnel through this barrier. This effect is discussed in detail in the next section (1.1). Because of their large TMR effect and relatively simple manufacturing, MTJs are currently used as read heads for hard disk drives [147].

In both types of junctions (GMR and TMR), the current through the non-magnetic layer can be spin-polarized and thus transfer angular momentum. If the magnetizations in both leads are non-collinear, this leads to a torque on the magnetizations in the ferromagnetic layers called spin-transfer torque (STT) [110, 59]. This goes beyond the two-current model, as considering the full vector of the non-equilibrium magnetization is essential ('spin coherence' [7]). The STT may switch the orientation of the magnetization in one of the layers (free layer). This can be used in magnetic random-access memory (MRAM) [104, 27, 65], where a bit is encoded in the

[1] We do not distinguish spintronics and magnetoelectronics; the magnetoresistive effects are sometimes sorted in the latter class [138, 50].

[2] Electrons which have their spin aligned parallel to the quantization direction are called majority or spin-up (↑) and those with anti-parallel alignment are called minority or spin-down (↓).

orientation of the free layer and read out by a magnetoresistance effect. MRAM is predicted to combine non-volatility, high storage density, speed, and energy efficiency, and might serve as a 'universal' memory [65]. Here, STT provides an alternative to switching with local magnetic fields [21, 72] with a preferable scaling behavior [65]. Another application of STT is the generation of microwave-frequency currents by exciting a steady precession of the magnetization in the free layer [77]. Beyond these broadly investigated applications STT, may also provide a key element in other advanced magnetic nanodevices [89].

Over the recent years, spintronics has developed into a broad and diverse research field with many directions and subfields. One goal of spintronics is to develop spin-based active components, in particular logic devices, which may supplement or even supersede current CMOS (complementary metal-oxide-semiconductor) electronics. This would add non-volatile memory functionality (with basically unlimited switching endurance [67]) to the logic device. Further, spintronic devices are predicted to outperform charge-based technology with respect to switching speed, scaling behavior, and energy consumption/heat creation [143, 67]. An early proposal of a spin field-effect transistor [32] is based on two ferromagnets connected by a semiconducting channel. The ferromagnets act as spin polarizer and analyzer, while inside the semiconductor the spin polarization is rotated by spin-orbit interaction (e.g. Rashba effect), which in turn is controlled by a gate voltage. This allows to manipulate the net current through the junction. Following this proposal, many devices based on various mechanisms have been proposed and are being investigated [138, 43, 11]. Many of these devices require integrating spintronics with semiconductor materials, preferably silicon [67]. Semiconductors offer many advantages [67], in particular a high degree of control over the electronic properties via structuring, doping/alloying, gate voltages, etc., and interaction with light; further, they often have a much longer spin-diffusion length than metals [7]. Important issues are the injection/extraction of spin-polarized currents into/from semiconductor materials [117] (ideally with a high spin filtering) and their detection, which are often solved by tunnel contacts [111, 67]. Alternatively, spin currents can be created (detected) by the (inverse) spin Hall effect [69] or other spin-orbit effects [6]. Further, illuminating a semiconductor with circularly polarized light induces a spin polarization [67] and vice versa, as utilized in spin light-emitting diodes [67] and lasers [118].

Another long-term goal of spintronics is to employ the full quantum-mechanical spin state as a qubit to perform quantum computations [8, 10]; a quantum computer would be able to solve certain problems much faster than a conventional one.

Spintronics is strongly interrelated with material science; many different classes of materials are being studied with regard to their benefits in spintronic applications, including half-metals (e.g. some Heusler alloys) [46], (diluted) (anti-)ferromagnetic semiconductors [91, 37], antiferromagnetic materials [92], topological insulators [107], and organic molecular materials [112, 16] (in particular graphene [107]).

A research field closely linked to spintronics is *magnonics*, which studies (elementary) excitations of the magnetic system (spin waves or magnons) and utilizes them to carry or even process information [85, 81, 89]. They can propagate without moving charge carriers e.g. in ferromagnetic insulators and can be controlled e.g. by magnetic metamaterials [80] (magnonic crystals). The STT may provide an interface between magnonics and spintronics [89].

The field of *spin caloritronics* studies the interplay of spin and heat currents [30, 12]. It yields a large number of novel effects, many of which can be discovered by considering the spin-dependent or magnetic-configuration-dependent version of a thermoelectric effect or by replacing the driving bias voltage in a spintronic effect by a temperature gradient. For example, in a magnetic device the Seebeck effect, i.e. the generation of a voltage or current by a temperature gradient, may be different for both spin channels, which yields the spin-dependent Seebeck effect [30]; this is also a spin caloritronic analogue of spin-dependent resistance and induces a spin accumulation or spin-polarized current. In a MTJ, one can also consider a dependence of the Seebeck effect on the alignment of the magnetizations, which is termed tunnel magneto-Seebeck effect [30, 139, A7] and an analogue of the TMR. Further, spin-polarized currents induced by a temperature gradient in a MTJ can create thermal spin-transfer torque [54, A8]. Similar generalizations can be found for other thermoelectric effects [12]. Recently, effects induced by

applying bias voltage and temperature gradient simultaneously were investigated, e.g. the bias-enhanced tunnel magneto-Seebeck effect [A1]. Other spin caloritronic effects are based on spin-orbit coupling or collective excitations [12].

1.1 Coherent magnetic tunnel junctions

In this work, we focus on *coherent* MTJs, which indicates that the transport through the tunnel barrier is coherent (or ballistic). The characteristic feature is a crystalline barrier with epitaxial interfaces. As a result of this high structural quality, the state (or symmetry) and in particular the Bloch $\vec{k}_{\parallel}$-vector of tunneling electrons is conserved. In contrast, in a *diffusive* MTJ, e.g. with an amorphous AlO_x barrier or low quality interfaces, electrons are (incoherently) scattered during the tunneling. In this case, the transport can be understood in terms of the Jullière model [68]. This model describes the conductance in terms of an (effective) density of states for each ferromagnetic lead and the TMR arises from the spin polarization of these densities. Thus, a high spin polarization (at the Fermi-energy) of the ferromagnetic material, ideally a half-metal, is required to obtain a high TMR. In a coherent MTJ, transport is mainly determined by quantum-mechanical boundary conditions at the interfaces, i.e. the matching between states in the ferromagnetic leads and evanescent states in the barrier, and decay rates of the latter. Since these decay rates can be very different, the contribution of various states in the ferromagnets depends on which evanescent states they couple to [95]; this effect is called symmetry selection by the barrier. Furthermore, the contribution of a state in one ferromagnetic lead depends on the available 'matching' states in the other, in particular for anti-parallel alignment. This mechanism was first investigated for the Fe/MgO system [25, 94], i.e. iron leads separated by a magnesium oxide barrier. In this case there is a single band of evanescent states (the 'Δ_1-like' states) in the MgO barrier, which has the smallest decay rate and dominates the transport. For these states iron is half-metallic, i.e. there are Δ_1-like states at the Fermi-energy for the majority spin but not for the minority spin. Consequently, the large (by comparison) Δ_1-like contributions are blocked for anti-parallel alignment, since tunneling majority Δ_1-like states have no 'matching' minority states in the other lead. Thus, calculations predicted a very large TMR effect [25, 94]. Fortunately, this system can be grown with high crystalline quality and experiments soon found large TMR effects [105, 149], which by far outperformed those of GMR and diffusive TMR junctions [60]. Importantly, these large effects can be obtained even in junctions prepared by sputtering technique [105], which facilitates production on an industrial scale. The dominating majority Δ_1-like contributions also lead to highly spin-polarized currents for parallel and non-collinear alignment (spin selection). This is beneficial for an efficient creation of STT and for spin injection and makes this system a building block in many spintronic device designs.

In most experiments $Fe_{1-x}Co_x$ alloys with various concentrations are used for the ferromagnetic leads[3] rather than pure iron, which is assumed in most calculations. The impact of disordered $Fe_{1-x}Co_x$ leads on the transport in these MTJs has not yet been investigated theoretically. It seems obvious that the presence of disorder should interfere with symmetry selection and other effects. Further, alloying changes the states available for transport at the Fermi-energy via band filling. Thus, in this work we investigate the impact of these leads using a realistic description of disordered alloys. We aim to disentangle the various effects of alloying and understand their impact on TMR and STT.

1.2 Outline

From the introduction above it is clear that a quantum-mechanical treatment of transport is necessary to obtain a meaningful description of coherent MTJs. In this work, we additionally aim for an *ab initio* treatment, which basically allows for an unbiased view of the relevant physical effects. The methods which we employ for this description are explained in section 2,

[3] Interestingly, the usage of FeCo as lead material is often motivated [148, 19] by an earlier theoretical study, which approximated the alloy by an ordered structure and predicted an increase of the TMR with the Co concentration[152]. However, from the perspective of the present work and recent experiments, these results seem inaccurate.

in particular the non-equilibrium Green's function method, which is used to calculate transport properties. We also introduce the treatment of symmetry via irreducible representations of the space group (section 2.5). This is an essential tool in explaining the effect of symmetry selection in the barrier. Disorder breaks the spatial symmetry in alloys, which makes their theoretical description considerably more difficult than for ideal crystals. In this work, we treat disordered alloys via a self-consistent effective-medium approach: the coherent potential approximation (CPA), which is introduced in section 3. This method requires some additional considerations in order to calculate transport properties (vertex corrections), these are derived in section 3.3. Calculating physical properties (e.g. densities) within the CPA often requires restricted averages, which describe atoms embedded in the effective medium (sections 3.4 and 3.5). In particular, these allow to calculate the (non-)equilibrium Bloch spectral density (section 3.6), which provides detailed information on electronic states and effects of disorder. Using these methods we give a thorough description of the electronic structure of $Fe_{1-x}Co_x$ alloys in section 4.1, which forms the basis for understanding the impact of alloying and disorder on transport processes. In section 4.2 we discuss the TMR effect for the well established Fe/MgO system. In particular, we explain the effect of symmetry filtering in the barrier (4.2.1) and other effects like interface-resonance states (4.2.2). The calculations are compared to experimental results in section 4.2.3 and we discuss open questions and possible explanations for observed discrepancies. In section 4.2.4 we briefly discuss the transport in the Fe/MgO system in a wide energy range to substantiate the understanding of the impact of various effects on the TMR. Based on this understanding, we then extend the discussion to MTJs with disordered $Fe_{1-x}Co_x$ alloy leads (section 4.3). We investigate the impact of disorder and band filling and their interplay with other effects. This interplay and the resulting TMR are discussed for zero bias (section 4.4) and in a wide range of bias voltages (section 4.5). These results for FeCo alloy leads are compared with experimental results in section 4.4.1. In section 5 we introduce STT in MTJs. The theoretical methods for its *ab initio* description are briefly discussed. Subsequently, a model is explained in section 5.2, which allows to determine the torque using only current channels for both collinear alignments. This allows to understand most effects which govern the STT from the explanations already established in the sections on TMR. The STT is discussed for varying bias voltage (section 5.3) and Co concentration (section 5.4). We conclude the section on STT with a general discussion and comparison with available experimental results (section 5.5).

2 Theory – Quantum transport

2.1 Introduction

In this work, we use an atomistic description of electronic transport in nanoscale devices based on quantum-mechanical *ab initio* calculations. This is in contrast e.g. to a semi-classical description via the Boltzmann transport equation [55] or using a tight-binding model [102]. This challenging task requires a series of approximations. The first step is to separate the motion of electrons and atomic nuclei via the Born-Oppenheimer approximation. Subsequently, the atomic positions are regarded as fixed; an influence of phonons or other elementary excitations on the electronic system is not considered in this work and we assume zero temperature.

The electron-electron interaction is treated within density functional theory (DFT) [78]. This allows a description of properties of the interacting system by functionals of its ground-state density (Hohenberg-Kohn theorems [66]). The latter in turn is determined by minimizing the total energy [86]. Via the Kohn-Sham ansatz DFT is used to map the interacting many-electron system to an effective non-interacting system described by a single-particle Schrödinger-like equation. This Kohn-Sham equation describes the interaction via a static effective potential [79], which includes the classical Coulomb repulsion and an exchange-correlation potential. It is calculated from the electronic density; this leads to a self-consistent system of equations [A3]. Throughout this work we use the local-spin-density approximation (LSDA) [79, 136, 137] for exchange-correlation functional and potential. Once the DFT self-consistent calculation is converged, we use the Kohn-Sham system as an approximation of the quasiparticle structure of the interacting system. In particular, the Kohn-Sham energies are shown as band structure, etc. and the states are used for subsequent transport calculations. For a discussion of this interpretation we refer to the literature [93, 34].

For transport calculations we use a non-equilibrium Green's function approach [31]. This provides access to currents and the density of conducting electrons in a system under finite bias or more generally under non-equilibrium conditions. This method is introduced in detail in the following sections.

All *ab initio* results shown in this work are obtained using a Green's function based Korringa-Kohn-Rostoker multiple-scattering method (KKR) [150], which was introduced in [A3]. For a description of this method and a more detailed discussion on DFT we refer to [A3] and the literature [150, 97] (KKR) and [106, 93] (DFT). To clarify the notation the key equations of the KKR method are sumarized in appendix A.2.

2.2 Non-equilibrium Green's functions

In this section we introduce various *Green's functions* (GF) [102, 42, 31] that are used in many-body theory. They are defined in terms of field operators $a^\dagger_{\vec{r}}$ and $a_{\vec{r}}$, which create and annihilate a particle at site $\vec{r}$. The definitions are summarized in table 1. The expectation value $\langle\cdot\rangle$ is taken at the initial time of the Heisenberg picture and may include a statistical ensemble average. The various GFs are connected by numerous relations, some are listed in table 1. All given GFs can be used for ground-state, equilibrium, and non-equilibrium systems; however, $G^{n/p}$ attain particular importance in non-equilibrium situations and are refereed to as *non-equilibrium Green's functions* (NEGF).

Given a complete orthonormal single-particle basis $\{\,|\alpha\rangle\,\}$, the field operators can be written as [102]

$$a_{\vec{r}} = \sum_\alpha \langle\vec{r}|\alpha\rangle\, a_\alpha = \sum_\alpha \phi_\alpha(\vec{r})\, a_\alpha \quad \Leftrightarrow \quad a_\alpha = \sum_{\vec{r}} \langle\alpha|\vec{r}\rangle\, a_{\vec{r}} = \sum_{\vec{r}} \phi_\alpha(\vec{r})^*\, a_{\vec{r}}. \tag{2.2}$$

Thus, we can obtain other representations of the GFs by replacing the field operators by creation and annihilation operators for a different basis. Different representations are related by the unitary transformation following from eq. (2.2). The above GFs are single-particle (or two point) GFs; they can be generalized by replacing the field operators by other operators including products of field operators [102].

Definitions		
G^r	$-i\,\theta(t_2-t_1)\left\langle\left[a_{\vec{r}_2}(t_2), a^\dagger_{\vec{r}_1}(t_1)\right]_+\right\rangle$	retarded GF
G^a	$i\,\theta(t_1-t_2)\left\langle\left[a_{\vec{r}_2}(t_2), a^\dagger_{\vec{r}_1}(t_1)\right]_+\right\rangle$	advanced GF
$G^n = -i\,G^<$	$\left\langle a^\dagger_{\vec{r}_1}(t_1)\, a_{\vec{r}_2}(t_2)\right\rangle$	electron GF
$G^p = i\,G^>$	$\left\langle a_{\vec{r}_2}(t_2)\, a^\dagger_{\vec{r}_1}(t_1)\right\rangle$	hole GF
A	$\left\langle\left[a_{\vec{r}_2}(t_2), a^\dagger_{\vec{r}_1}(t_1)\right]_+\right\rangle$	gDOS

Relations	
$A = i\left(G^r - G^a\right) = G^n + G^p$	(2.1a)
$G^r = -i\,\theta(t_2-t_1)\,A \qquad G^a = i\,\theta(t_1-t_2)\,A$	(2.1b)
$G^r(\vec{r}_2,t_2,\vec{r}_1,t_1) = \left(G^a(\vec{r}_1,t_1,\vec{r}_2,t_2)\right)^*$	(2.1c)
$G^n(\vec{r}_2,t_2,\vec{r}_1,t_1) = \left(G^n(\vec{r}_1,t_1,\vec{r}_2,t_2)\right)^* \qquad G^p(\vec{r}_2,t_2,\vec{r}_1,t_1) = \left(G^p(\vec{r}_1,t_1,\vec{r}_2,t_2)\right)^*$	(2.1d)
$A(\vec{r}_2,t_2,\vec{r}_1,t_1) = \left(A(\vec{r}_1,t_1,\vec{r}_2,t_2)\right)^*$	(2.1e)

Table 1: Time-dependent real-space single-particle fermionic Green's functions (GF) $G^\xi(\vec{r}_2,t_2,\vec{r}_1,t_1)$ and generalized density of states (gDOS) A: definitions and relations.
The field operators $a_{\vec{r}}(t)$, $a^\dagger_{\vec{r}}(t)$ are in the Heisenberg picture; we use a notation similar to [102] and add GFs ($G^{n/p}$) from [31], the more common definitions $G^{</>}$ are also shown [55].

For *time-independent* systems (including steady-state), the GFs depend only on the time difference $t_2 - t_1$ and we can investigate their Fourier transform, i.e. energy-dependent GFs. In this case, it follows from eq. (2.1b) that [102]

$$G^r(E;\vec{r}_2,\vec{r}_1) = G^z(E + i\,0^+;\vec{r}_2,\vec{r}_1) \quad \text{and} \quad G^a(E;\vec{r}_2,\vec{r}_1) = G^z(E - i\,0^+;\vec{r}_2,\vec{r}_1) \tag{2.3a}$$

$$\text{where} \quad G^z(z;\vec{r}_2,\vec{r}_1) = \int \frac{\mathrm{d}E'}{2\pi}\, \frac{A(E';\vec{r}_2,\vec{r}_1)}{z - E'}. \tag{2.3b}$$

This means that $G^{r/a}$ are the side limits of G^z, which is their common analytic continuation. G^z in turn can be determined from the generalized density of states (gDOS, or spectral function) A and has singularities (poles, branch cuts, etc.) on the real axis where A is non-zero [42]. The gDOS A again can be obtained from $G^{r/a}$ via eq. (2.1a).

If we assume that the system is in *thermal equilibrium* and can be described by a grand canonical ensemble, the expectation value is given by

$$\left\langle(\cdot)\right\rangle = \mathrm{Tr}\left[\rho\,(\cdot)\right] \quad \text{where} \quad \rho = e^{-\beta\,(H-\mu\,N)} / \,\mathrm{Tr}\left[e^{-\beta\,(H-\mu\,N)}\right] \tag{2.4}$$

(ρ density matrix, H Hamiltonian, N particle number operator, μ chemical potential, and $\beta = 1/k_B\,T$ inverse temperature). For this case, $G^{n/p}$ can likewise be expressed in terms of A as [42, 102]

$$G^n(E;\vec{r}_2,\vec{r}_1) = f(E)\,A(E;\vec{r}_2,\vec{r}_1) \quad \text{and} \quad G^p(E;\vec{r}_2,\vec{r}_1) = (1 - f(E))\,A(E;\vec{r}_2,\vec{r}_1), \tag{2.5}$$

where $f(E) = \left(e^{\beta\,(E-\mu)}+1\right)^{-1}$ is the Fermi distribution function. This result is called fluctuation-dissipation theorem [55] and can be obtained by writing the GFs in terms of exact energy and particle-number eigenstates [102]. Note that for $T \to 0$ ($\beta \to \infty$) the Fermi function turns into a unit step function $f(E) = \theta(\mu - E)$.

In the case of *independent* (i.e. non-interacting) *particles*, the (Hermitian) Hamiltonian can in principle be diagonalized by a basis of single-particle states [42]

$$H\,|n\rangle = \epsilon_n\,|n\rangle \quad \text{i.e.} \quad H = \sum_n \epsilon_n\, a^\dagger_n\, a_n. \tag{2.6}$$

	$G^\xi(E;n)$	$G^\xi(E)$
G^z	$1/\big(z-\epsilon_n\big)$	$\big(z-H\big)^{-1}$
$G^n/2\pi$	$\rho_n\,\delta(E-\epsilon_n)$	$f(E)\,\delta(E-H)$
$G^p/2\pi$	$\big(1-\rho_n\big)\,\delta(E-\epsilon_n)$	$\big(1-f(E)\big)\,\delta(E-H)$
$A/2\pi$	$\delta(E-\epsilon_n)$	$\delta(E-H)$

Table 2: Energy-dependent GFs for a system of independent particles ($G^{n/p}$ for thermal equilibrium only) in the basis of energy eigenstates $G^\xi(E;n)$ (second column) and as basis-independent operators $G^\xi(E)$ (last column). $G^{r/a}$ can be obtained from G^z via eq. (2.3a). ρ_n is the occupation of eigenstate n given by $\rho_n = \langle a_n^\dagger\, a_n\rangle$, which for the case of thermal equilibrium yields $\rho_n = f(\epsilon_n)$. The operators are related to real-space GFs through $G^\xi(E;\vec{r}_2,\vec{r}_1) = \langle\vec{r}_2|\, G^\xi(E)\,|\vec{r}_1\rangle$.

The Heisenberg equation of motion for annihilation (and creation) operators for these states can be solved

$$i\,\frac{\mathrm{d}}{\mathrm{d}t}a_n(t) = \big[a_n(t),H\big]_- = \epsilon_n\,a_n(t) \quad\Rightarrow\quad a_n(t) = e^{-i\,\epsilon_n\,t}a_n. \tag{2.7}$$

In this basis the GFs are diagonal and can be calculated analytically. They are summarized in table 2. It is convenient to introduce basis-independent operators, which are also listed in table 2 and used synonymous to the GFs. In this form GFs are used throughout most of this work.

The retarded (or advanced) GF has a remarkably simple structure, i.e. the inverse of an operator; it can be calculated without diagonalizing the Hamiltonian. Further, it can be obtained from the retarded GF of a simpler system using the Dyson equation (section 2.3). Its analytic properties can be used to reduce the computational effort for energy-integrated quantities by using contour integration [150]. For these and other reasons it is often employed in numerical calculations, in particular in the KKR method.

Many physical properties can be obtained from single-particle GFs. Particularly important is the density, which can be obtained from the diagonal elements

$$n_n(E,\vec{r}) = \frac{1}{2\pi}G^n(E;\vec{r},\vec{r}) \quad \Big(= -\frac{i}{2\pi}G^<(E;\vec{r},\vec{r})\Big) \qquad \text{occupied states} \tag{2.8a}$$

$$n(E,\vec{r}) = \frac{1}{2\pi}A(E;\vec{r},\vec{r}) = -\frac{1}{\pi}\,\mathrm{Im}\,G^r(E;\vec{r},\vec{r}) \qquad \text{all states.} \tag{2.8b}$$

From this, the real-space density can be obtained by integration over energy and the usual density of states by integrating over a unit cell. Similarly, the density in other representations is obtained from respective GFs. In general, the expectation value of any single-particle observable (and some many-particle observables) can be calculated from single-particle GFs [42].

The various GFs defined and discussed above can be easily extended to include the spin degree of freedom. To this end, we add a spin index $\sigma = \uparrow,\downarrow$ to the ladder operators in the definitions in table 1, which results in four combinations for each GF. The relations for the GFs in table 1 remain valid, where interchanging the two space and time coordinates also interchanges the spin indexes. In general, the four spin combinations for a GF are coupled and it is useful to introduce a combined GF, which is a matrix in spin space

$$\underline{G} = \begin{pmatrix} G_{\uparrow\uparrow} & G_{\uparrow\downarrow} \\ G_{\downarrow\uparrow} & G_{\downarrow\downarrow} \end{pmatrix}. \tag{2.9}$$

For a spin-dependent single-particle Hamiltonian we separate the spin-independent (H_0) and the spin-dependent ($\vec{\Delta}$) part (SI units)

$$\underline{H} = H_0\,\underline{1} - \vec{\Delta}\,\underline{\vec{m}}, \qquad \text{where}\quad \underline{1} = \left(\begin{smallmatrix}1&0\\0&1\end{smallmatrix}\right)\quad\text{and} \tag{2.10a}$$

$$\underline{\vec{m}} = -\,\gamma_S\,\underline{\vec{S}} = -\,\frac{g_S\,\mu_B}{\hbar}\,\frac{\hbar\,\underline{\vec{\sigma}}}{2} \approx -\,\mu_B\,\underline{\vec{\sigma}} \qquad \text{is the spin magnetization} \tag{2.10b}$$

(γ_S: electron spin gyromagnetic ratio, $\vec{\underline{S}}$: electron spin (operator), $g_S \approx 2$: electron spin g-factor, μ_B: Bohr magneton, $\vec{\underline{\sigma}}$: Pauli matrices).
The above statements for independent particles remain valid for combined spin-dependent GFs, in particular $\underline{G}^z = \left(z - \underline{H}\right)^{-1}$, where the inversion includes the spin space. Of course, spin-dependent properties can be calculated from the GF, in particular the spin magnetization

$$\vec{m}(E, \vec{r}) = -\mu_B \frac{1}{2\pi} \operatorname*{Tr}_S \left[\underline{G}^n(E; \vec{r}, \vec{r})\, \vec{\underline{\sigma}}\right], \tag{2.11}$$

where the trace is only over spin space; for the electron density a trace in spin space is added in eq. (2.8). Orbital magnetization is not considered in this work. If the spin-dependent part of the Hamiltonian is (globally) aligned with the z-axis, i.e. $\Delta_x = \Delta_y = 0$, the four spin components of the GFs are decoupled; the diagonal components $G_{\uparrow\uparrow}$ and $G_{\downarrow\downarrow}$ can be obtained independently while $G_{\uparrow\downarrow} = G_{\downarrow\uparrow} = 0$.

For convenience, the exchange field (or Weiss field) $\vec{\Delta}$ as defined in eq. (2.10) has units of a magnetic field and couples to the spin magnetization. However, in this work it is created by the spin-dependent exchange-correlation potential $\underline{V}_{xc}$ in LSDA [136]. The most important contribution to $\vec{\Delta}$ is the Fock (or exchange) term, which effectively reduces Coulomb repulsion for electrons with parallel spin via the Pauli principle [102, 15]; $\vec{\Delta}$ also includes higher-order correlations which couple to the spin. These quantum-mechanical many-particle effects are the cause for (anti-)ferromagnetism and much larger than typical magnetic fields, which are not considered in this work.

In equilibrium the magnetization is locally aligned with the exchange field [15, 28]. However, the orientation of both generally depends on the position. In many cases it is appropriate to assign a single orientation to each atom (rigid-spin approximation) [5] and assume that the magnetization is collinear within a surrounding volume (e.g. ASA sphere). For ferromagnets or other collinear configurations we choose the global polarization direction along the z-axis and the spins are decoupled in the non-relativistic calculations. For a bulk ferromagnet the majority spin is along $+\vec{e}_z$ and the magnetization is given by $\vec{m} = -\mu_B \left(n_\uparrow - n_\downarrow\right) \vec{e}_z$, where n_σ is the density for spin σ. By rewriting the spin-dependent exchange-correlation potential

$$\underline{V}_{\mathrm{xc}} = \begin{pmatrix} V_{\mathrm{xc}}^{\uparrow} & 0 \\ 0 & V_{\mathrm{xc}}^{\downarrow} \end{pmatrix} = \frac{V_{\mathrm{xc}}^{\downarrow} + V_{\mathrm{xc}}^{\uparrow}}{2}\, \underline{1} - \frac{V_{\mathrm{xc}}^{\downarrow} - V_{\mathrm{xc}}^{\uparrow}}{2}\, \underline{\sigma}_z$$

we identify the resulting exchange field

$$\vec{\Delta} = -\frac{1}{2\mu_B} \left(V_{\mathrm{xc}}^{\downarrow} - V_{\mathrm{xc}}^{\uparrow}\right) \vec{e}_z. \tag{2.12}$$

In the following sections we omit spin indexes; the derivations are valid for the combined spin-dependent GFs as well as individually for the diagonal components if the spins are decoupled.

2.3 Dyson and Keldysh equation

In this section we derive equations relating GFs for different systems. We consider the case of a steady-state system of independent particles. We assume that the difference between the two systems is described by an (in general) non-Hermitian and energy-dependent operator (e.g. a self-energy), i.e. $H_1 = H_0 + \Sigma$. For the retarded GF we use the operator form given in table 2 and obtain the *Dyson equation*

$$G_1^r = \left(E + i\,0^+ - H_0 - \Sigma^r\right)^{-1} = \left((G_0^r)^{-1} - \Sigma^r\right)^{-1} = G_0^r + G_0^r\, \Sigma^r\, G_1^r, \tag{2.13}$$

which can be recast in various ways [42, 150, A3]. An analogous equation applies to advanced GFs, where $\Sigma^a = (\Sigma^r)^\dagger$ must hold to conserve analytic properties of the GFs. Eq. (2.13) includes the case when Σ is Hermitian, e.g. a potential difference $\Sigma^r = \Sigma^a = \Delta V$. By combining eqs.

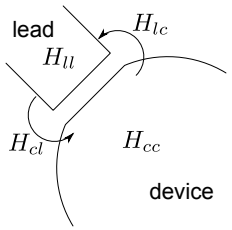

Figure 2.1: Illustration of the separation of the Hamiltonian into a detached lead, the rest of the device, and their mutual coupling.

(2.1a) and (2.13) we obtain an equation relating the gDOS in both systems

$$A_1 = i\left(G_1^r - G_1^a\right) = A_0 + A_0\,\Sigma^a\,G_1^a + G_0^r\,\Gamma\,G_1^a + G_0^r\,\Sigma^r\,A_1 \tag{2.14a}$$

$$= \left(1 + G_1^r\,\Sigma^r\right)A_0\left(1 + \Sigma^a\,G_1^a\right) + G_1^r\,\Gamma\,G_1^a \tag{2.14b}$$

$$\text{with} \quad A_0 = i\left(G_0^r - G_0^a\right) \quad \text{and} \quad \Gamma = i\left(\Sigma^r - \Sigma^a\right),$$

where the second line is obtained from the first using eq. (2.13). This is the *Keldysh equation*; it can be derived under more general conditions for interacting particles in time-dependent non-equilibrium systems [75, 55]. Again using eqs. (2.1a) and (2.13) we rewrite the first term in eq. (2.14b)

$$\left(1 + G_1^r\,\Sigma^r\right)A_0\left(1 + \Sigma^a\,G_1^a\right) = G_1^r\,(G_0^r)^{-1}\,A_0\,(G_0^a)^{-1}\,G_1^a = 0;$$

thus, we find that this term vanishes[4] and we obtain the *steady-state* Keldysh equation [31]

$$A_1 = G_1^r\,\Gamma\,G_1^a, \tag{2.14c}$$

which is applied in this work. If the decomposition $\Gamma = \Sigma^{in} + \Sigma^{out}$ into in-scattering and out-scattering contributions [31] is known (see section 2.4), the Keldysh equation (2.14c) can be decomposed into separate equations for the electron and hole GF[5] (compare eq. (2.1a))

$$G_1^n = G_1^r\,\Sigma^{in}\,G_1^a \quad \text{and} \quad G_1^p = G_1^r\,\Sigma^{out}\,G_1^a. \tag{2.14d}$$

Keeping track of the occupation of states is a major task of the NEGF method.

2.4 Quantum transport

In this section we describe how transport in microscopic and mesoscopic systems can be described quantum-mechanically using GFs [31]. We are interested in a device that contains a (central) region, where coherent transport is important and thus a quantum-mechanical description is necessary. The tunnel junctions investigated in this work are a prominent example of such systems. We assume that leads contacting this region can be treated as ideal conductors. To investigate the effect of a particular lead l on the device, the Hamiltonian of the system is split into a detached lead, the rest of the device, and their coupling as illustrated in figure 2.1. We assume a steady-state system of independent particles and investigate energy-dependent GFs. To calculate the retarded GF we need to solve the system of coupled equations

$$\begin{pmatrix} E + i\,0^+ - H_{ll} & -H_{lc} \\ -H_{cl} & E + i\,0^+ - \tilde{H}_{cc} \end{pmatrix} \begin{pmatrix} G_{ll}^r & G_{lc}^r \\ G_{cl}^r & \tilde{G}_{cc}^r \end{pmatrix} = \begin{pmatrix} 1 & 0 \\ 0 & 1 \end{pmatrix}. \tag{2.15}$$

From this we obtain [31]

$$\tilde{G}_{cc}^r = \left(E - \tilde{H}_{cc} - \Sigma_l^r\right)^{-1} \quad \text{with} \quad \Sigma_l^r = H_{cl}\,g_l^r\,H_{lc} \quad \text{and} \quad g_l^r = \left(E + i\,0^+ - H_{ll}\right)^{-1}, \tag{2.16}$$

[4] The first term in the (full) Keldysh equation (2.14b) can contribute in time-dependent systems, where it is related to the initial state [88, 76, 33].

[5] In standard notation $\Sigma^{in} = -i\,\Sigma^<$ and $\Sigma^{out} = +i\,\Sigma^>$.

where g_l^r is the GF of the isolated lead. Σ_l^r is called self-energy of the lead and describes the impact of the coupling to the lead on the device. This procedure can be applied to multiple leads; assuming that they are not directly coupled ($H_{ll'} \approx 0$) this leads to

$$G_{cc}^r = \left(E - H_{cc} - \Sigma^r\right)^{-1} \quad \text{with} \quad \Sigma^r = \sum_l \Sigma_l^r = \sum_l H_{cl}\, g_l^r\, H_{lc}, \tag{2.17}$$

where H_{cc} is the Hamiltonian of the central region with all leads detached and G_{cc}^r is the GF in this region including the coupling to all leads. An analogous equation can be obtained for the advanced GF. Next, we calculate the gDOS A_{cc} in the central region using the Keldysh equation (2.14c); we obtain

$$A_{cc} = G_{cc}^r\, \Gamma\, G_{cc}^a = \sum_l G_{cc}^r\, \Gamma_l\, G_{cc}^a = \sum_l A_{cc}^{(l)} \quad \text{where} \tag{2.18a}$$

$$\Gamma_l = i\left(\Sigma_l^r - \Sigma_l^a\right) = H_{cl}\, a_l\, H_{lc} \quad \text{with} \quad a_l = i\left(g_l^r - g_l^a\right). \tag{2.18b}$$

Thus, the gDOS in the central region can be decomposed into contributions connected to each lead. We assume that each lead is (and remains) in thermal equilibrium described by a distribution function $f_l = \left(e^{\beta_l\,(E-\mu_l)} + 1\right)^{-1}$. Hence, using eq. (2.5) the gDOS a_l of lead l and its contribution to the central region can be decomposed into occupied and unoccupied states

$$A_{cc}^{(l)} = G_{cc}^{n\,(l)} + G_{cc}^{p\,(l)} \quad \text{where} \quad G_{cc}^{n\,(l)} = G_{cc}^r\, \Sigma_l^{in}\, G_{cc}^a \quad \text{and} \quad G_{cc}^{p\,(l)} = G_{cc}^r\, \Sigma_l^{out}\, G_{cc}^a \tag{2.19a}$$

$$\text{with} \quad \Sigma_l^{in} = f_l\, \Gamma_l \quad \text{and} \quad \Sigma_l^{out} = \left(1 - f_l\right) \Gamma_l. \tag{2.19b}$$

Occupied states in a lead act as a source of electrons in the central region while unoccupied states are a drain of electrons (or equally a source of holes). The leads can have different temperatures and chemical potentials; this induces a temperature gradient and a voltage drop across the central region, which is consequently in a state of non-equilibrium. The total density of electrons (or holes) in the central region is the sum of contributions from all leads.

The above results are sufficient to describe coherent transport through the central region. In addition, it is possible to include scattering inside the central region. This is an advantage of the NEGF formalism. In general, this scattering can be described by an additional self-energy Σ_φ, which is added to the effect of the leads [31]. More precisely, we have $\Sigma^r = \Sigma_\varphi^r + \sum_l \Sigma_l^r$ for the retarded self-energy entering in the retarded GF (eq. (2.17)) and the electron and hole GFs are

$$G_{cc}^n = G_{cc}^r \left(\Sigma_\varphi^{in} + \sum_l \Sigma_l^{in}\right) G_{cc}^a \qquad G_{cc}^p = G_{cc}^r \left(\Sigma_\varphi^{out} + \sum_l \Sigma_l^{out}\right) G_{cc}^a. \tag{2.20}$$

The specific form of the scattering self-energy depends on the particular type and description of scattering; the derivation often requires the use of many-particle NEGFs and diagrammatic perturbation theory [55, 34]. In this work, we investigate the case of disorder scattering, which can be handled in an independent-particle picture. It is treated with the coherent potential approximation (CPA), which describes substitutionally disordered materials by a self-consistent effective medium and is introduced in section 3.

A particularly interesting and important transport property is the current through the device. It can be shown [31, 96] that the current from lead l into the central region is given by (in SI units)

$$I_{l,tot} = \int \mathrm{d}E\; I_l(E) \quad \text{with}$$

$$I_l = \frac{e}{h}\, \mathrm{Tr}\left[\Sigma_l^{in}\, G_{cc}^p - \Sigma_l^{out}\, G_{cc}^n\right]. \tag{2.21}$$

Using eqs. (2.20) and (2.19b) this can be decomposed into coherent and incoherent contributions $I_l = I_l^{coh} + I_l^{inc}$

$$I_l^{coh} = \frac{e}{h} \sum_{l'} \left(f_l - f_{l'}\right)\, \mathrm{Tr}\left[\Gamma_l\, G_{cc}^r\, \Gamma_{l'}\, G_{cc}^a\right] = \frac{e}{h} \sum_{l'} \left(f_l - f_{l'}\right) \bar{T}_{l \leftarrow l'}^{coh}, \tag{2.22}$$

$$I_l^{inc} = \frac{e}{h}\, \mathrm{Tr}\left[\Sigma_l^{in}\, G_{cc}^r\, \Sigma_\varphi^{out}\, G_{cc}^a - \Sigma_l^{out}\, G_{cc}^r\, \Sigma_\varphi^{in}\, G_{cc}^a\right]. \tag{2.23}$$

The coherent part has the form of a Landauer formula [31], where the trace gives the transmission $\bar{T}$ (summed over all modes) between leads l and l'. The incoherent part depends on the form of scattering. We discuss it for the case of disorder scattering described by the CPA. In order to proceed, we anticipate some results from section 3. In the case of the CPA, the retarded GF including scattering is the effective medium GF $\bar{G}^r$ (eq. (3.3)). For expressions involving a product of two retarded or advanced GFs one obtains an additional term called vertex correction (VC, section 3.3, eq. (3.14)); e.g. for the density contributed by lead l this yields

$$A_{cc}^{(l)} = \bar{G}_{cc}^r \, \Gamma_l \, \bar{G}_{cc}^a + \bar{G}_{cc}^r \, \Omega_l \, \bar{G}_{cc}^a. \tag{2.24}$$

Here, the VC Ω_l describe electrons or holes originating from lead l that have been scattered by the disorder. We show that the VC depend linearly on the source (in this case Γ_l). Thus, for each source Σ_l^{in} (Σ_l^{out}) we obtain a VC term Ω_l^{in} (Ω_l^{out}) that contributes independently to the scattering self-energy Σ_φ^{in} (Σ_φ^{out}). Because of the linearity we have

$$\Omega_l^{in} = f_l \, \Omega_l \quad \text{and} \quad \Omega_l^{out} = \big(1 - f_l\big) \, \Omega_l, \tag{2.25}$$

and we obtain an expression for the incoherent contribution to the current from lead l that is similar to the coherent one

$$I_l^{inc} = \frac{e}{h} \sum_{l'} \big(f_l - f_{l'}\big) \, \mathrm{Tr}\big[\Gamma_l \, \bar{G}_{cc}^r \, \Omega_{l'} \, \bar{G}_{cc}^a\big] = \frac{e}{h} \sum_{l'} \big(f_l - f_{l'}\big) \, \bar{T}_{l \leftarrow l'}^{inc}. \tag{2.26}$$

In the absence of magnetic fields, the transmission between two leads must be reciprocal [31] ($\bar{T}_{l' \leftarrow l} = \bar{T}_{l \leftarrow l'}$). Still, eq. (2.26) is asymmetric with respect to the leads. It can be shown [134] that including the VC ensures energy and particle-number conservation. This means $\bar{T}_{l' \leftarrow l}^{inc}(E) = \bar{T}_{l \leftarrow l'}^{inc}(E)$ for each energy E. However, this is not true for each $\vec{k}_\parallel$-point; disorder results in an elastic scattering between different $\vec{k}_\parallel$-points. In this sense, eq. (2.26), when calculated for individual $\vec{k}_\parallel$-points, describes the transmission in terms of $\vec{k}_\parallel$-states in lead l while any information on the $\vec{k}_\parallel$-state in lead l' is lost due to scattering. Phrased differently, the true transmission through a disordered region depends on incoming and outgoing $\vec{k}_\parallel$-vectors; however, we obtain an effective transmission which has been integrated over one of the two. The coherent part of the transmission is still reciprocal for each $\vec{k}_\parallel$-point.

The above equations for quantum transport were stated in a (single-particle) operator notation. The implementation in the KKR method requires some additional considerations [A4]. This is briefly discussed in appendix A.2.

2.5 Space groups

The characteristic feature of crystalline material is its high degree of spatial symmetry, which has a decisive impact on most of its properties. The spatial symmetry is described by a *space group* $\mathcal{G}_S = \big\{ \{\alpha|\vec{t}\} \big\}$ [20, 38, 51], where each element consists of a rotation α and a translation $\vec{t}$. The subgroup of pure translations $\mathcal{G}_T = \big\{ \{1|\vec{T}\} \big\}$ is a Bravais lattice and describes the periodicity of the crystal. The crystal can be visualized as a set of atoms, the basis, being repeated according to $\mathcal{G}_T$. Consequently, the position of each atom can be written as $\vec{R}_i = \vec{T}_i + \vec{S}_i$.

According to Wigner's theorem [20], in quantum mechanics a symmetry of the system is described by a unitary (or anti-unitary) operator which commutes with the Hamiltonian. We can use symmetries to classify eigenstates according to their transformation properties under the symmetries and decouple the eigenvalue equation. In the case of the Bravais lattice $\mathcal{G}_T$ this leads to *Bloch's theorem* [102]

$$\{1|\vec{T}\} \, \phi_{\vec{k}}^n(\vec{r}) = \phi_{\vec{k}}^n(\vec{r} - \vec{T}) = e^{-i \, \vec{k} \, \vec{T}} \phi_{\vec{k}}^n(\vec{r}) \tag{2.27a}$$

$$\Leftrightarrow \quad \phi_{\vec{k}}^n(\vec{r}) = e^{i \, \vec{k} \, \vec{r}} \, u_{\vec{k}}^n(\vec{r}) \quad \text{with} \quad u_{\vec{k}}^n(\vec{r} + \vec{T}) = u_{\vec{k}}^n(\vec{r}). \tag{2.27b}$$

Bloch's theorem states that eigenstates of the system are Bloch waves, which are also eigenstates of the Bravais lattice. They are characterized by a Bloch vector $\vec{k}$, which is restricted to the first Brillouin zone. For each $\vec{k}$-point there are still infinitely many eigenstates. Mostly, these are distinguished by different energy eigenvalues. However, for certain $\vec{k}$-vectors we can have degeneracies, which can be understood by taking into account the full space group $\mathcal{G}_S$. One can show [20] that if $\phi^n_{\vec{k}}$ is a Bloch wave then $\{\alpha|\vec{t}\}\,\phi^n_{\vec{k}}$ is also a Bloch wave with Bloch vector $\alpha\,\vec{k}$. We need to distinguish two cases: whether the two wave vectors are equivalent $\alpha\,\vec{k} \equiv \vec{k}$ (i.e. they differ only by a reciprocal lattice vector $\alpha\,\vec{k} = \vec{k} + \vec{K}$) or not $\alpha\,\vec{k} \not\equiv \vec{k}$.
If they are not equivalent, this means that we can obtain the eigenstates at $\alpha\,\vec{k}$ from those at $\vec{k}$. This is used to reduce the computational effort, since the full Brillouin zone can be recovered from its irreducible part.
Otherwise, if the two Bloch vectors are equivalent $\alpha\,\vec{k} \equiv \vec{k}$, then $\{\alpha|\vec{t}\}$ is a symmetry of the point $\vec{k}$; we call the group formed by these symmetries $\mathcal{G}_{\vec{k}}$. We can use $\mathcal{G}_{\vec{k}}$ to classify the states at $\vec{k}$ further [20]. Assume we know a basis formed by all degenerate states at $\vec{k}$, then applying a symmetry from $\mathcal{G}_{\vec{k}}$ to one of them must yield a linear combination of these states. Thus, the elements of $\mathcal{G}_{\vec{k}}$ can be represented as matrices in the basis of degenerate states. We could aim to find a new basis which makes these matrices as simple as possible. This amounts to finding *irreducible representations* (IRR) of $\mathcal{G}_{\vec{k}}$ [20, 38]. IRRs are matrices of small dimension which specify the transformation properties of corresponding states. They can be used to classify eigenstates for $\vec{k}$-points with non-trivial symmetry. Since IRRs are determined only up to a unitary transformation, they are identified by their trace, called character. The character for the identity element is equal to the dimension, which also determines the degeneracy.

In general, IRRs depend on the space group and the $\vec{k}$-point (line, plane) of symmetry; they are tabulated in the literature [20]. For a symmorphic space group IRRs can be obtained via $D^i(\{\alpha|\vec{T}\}) = e^{-i\,\vec{k}\,\vec{T}}\tilde{D}^i(\alpha)$ [20], where $\tilde{D}^i$ is an IRR of the point group obtained from $\mathcal{G}_{\vec{k}}$ by dropping the translations. Only few point groups can occur and their IRRs are also tabulated [20, 38]. In general, we may not know a basis of eigenstates; however, for any basis we can find linear combinations which transform according to the IRRs; these can only contribute to the corresponding eigenstates. Because of the Bloch theorem eq. (2.27) we only need to consider basis functions inside the primitive cell. If no atoms in the basis are equivalent (i.e. related by a symmetry), basis functions at different atomic site are independent. In the case of the KKR method, this means that we need symmetry-adapted linear combinations of spherical harmonics, called lattice harmonics [3] (or surface harmonics [20]). Since the basis functions are orthonormal, this amounts to a unitary rotation in the angular momentum indices. If two (or more) sites in the basis are equivalent, the basis functions comprise all equivalent sites (see e.g. [2] for hcp).

As an example, we investigate the symmetry group of a (flat) square, i.e. the point group C_{4v}. It contains eight symmetry elements: a four-fold rotation axis and four mirror planes. The group has five IRRs listed in table 3 including their characters; only Δ_5 is degenerate. Table 3 also states some low-degree basis functions in terms of Cartesian coordinates. One can easily verify that the non-degenerate IRRs transform according to the character table, while for Δ_5 one first needs to determine the transformation matrices from the basis function. The point group C_{4v} is of great importance in later sections. We also need the lattice harmonics for this group, which are given in appendix A.3.

The representation theory of finite groups (which includes point and space groups) provides a great amount of information on the IRRs. For example, it is possible to predict the splitting of bands when going from higher to lower symmetry $\vec{k}$-points or to obtain selection rules for interactions with external perturbations. In this work, we mainly use IRRs to separate contributions from different eigenstates at high-symmetry $\vec{k}$-points.

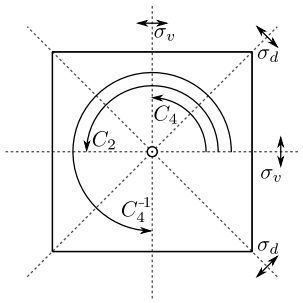

C_{4v}	1	C_2	$2\,C_4$	$2\,\sigma_v$	$2\,\sigma_d$	
Δ_1	1	1	1	1	1	1, (z)
Δ_1'	1	1	1	-1	-1	–
Δ_2	1	1	-1	1	-1	x^2-y^2
Δ_2'	1	1	-1	-1	1	$x\,y$
Δ_5	2	-2	0	0	0	$\{x, y\}$

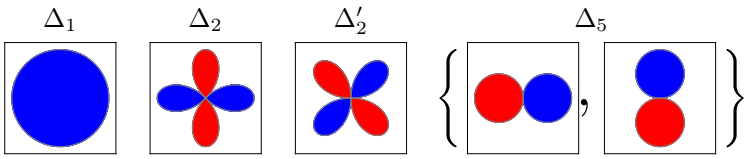

Table 3: Symmetry group of a square C_{4v} (or $4mm$).
(Top, Left) Illustration of the eight symmetries: three rotations, four mirror planes and the identity.
(Top, Right) Character table for the five irreducible representations including basis functions [38]; $\{x, y\}$ is a point on the unit circle. In three dimensions z transforms as Δ_1.
(Bottom) Polar plot of the given basis functions (blue is positive, red negative).

3 Theory – Coherent potential approximation

3.1 Introduction

The description of crystalline solids is greatly facilitated by the high degree of spatial symmetry, i.e. the space group (section 2.5). In particular, one can apply Bloch's theorem (eq. (2.27)) to describe the eigenstates via band-structure theory. This also splits a spatially infinite Hamiltonian (single electron or elementary excitation) into separate Hamiltonians for each $\vec{k}$-point, which can be solved in the primitive cell. Conversely, the description of disordered solids is difficult because of the absence of spatial symmetry. The precise atomic arrangement in a disordered solid (e.g. an alloy or amorphous material) is unknown (and uncontrollable). Thus, quantitative theoretical predictions are only feasible for results which are insensitive to these details. The same holds for experimental results as well as intended functionalities in applications. This usually means that the disordered region needs to be sufficiently large such that the quantity of interest represents some kind of average. This observation immediately suggests a possible approach for a description, i.e. to simulate a sufficiently large part (supercell), which is repeated periodically and possibly averaged over several arrangements. In principle, this approach can be used with basically every band-structure method and for any kind of spatial disorder. In practice, computational costs restrict the supercell size and thereby also the describable disorder (e.g. possible alloy/doping concentrations) and the attainable accuracy [A3].

In this work, we focus on the special case of substitutional disorder [150, 102], i.e. the solid has a crystal structure but sites are occupied randomly (the material may have additional ordered sublattices). This includes substitutional alloys (substitutional solid solutions) but can also be used e.g. to describe thermal disorder [24, 40]. For this case, specific methods have been developed which utilize the underlying crystal structure. They place an *effective medium* on all alloy sites which restores the crystal symmetry. In the *virtual crystal approximation* (VCA) [102] the effective medium represents a simple average of the components. It may be defined to have e.g. an averaged potential or atomic number (see e.g. appendix A.4). In some cases, when the components are similar, the VCA yields a reasonable description; however, it neglects effects of disorder, which are important for transport. A more accurate description can be obtained using GFs (section 2.2). We may assume that properties of interest can be calculated from configuration-averaged GFs, i.e. where the ensemble average has been taken over all possible occupations of alloy sites. One may also consider restricted averages, where the occupation is fixed for one or several sites. The (fully) averaged GF $\langle G \rangle$ has the space group symmetry of the underlying crystal structure. Thus, we can define an effective medium by [102, 135]

$$\big\langle G(z) \big\rangle = \big(z - H_{eff}(z)\big)^{-1}, \tag{3.1}$$

where $H_{eff}(z)$ has the full spatial symmetry but may contain complicated energy-dependent, non-Hermitian, and non-local contributions. Thus, the disordered Hamiltonian is mapped to an effective, symmetric Hamiltonian, which contains the effects of disorder as a self-energy. Of course, the latter cannot be calculated exactly. A popular class of self-consistent, approximate methods is the *coherent potential approximation* (CPA) [150, A3]. A considerable simplification is obtained by using the *single-site approximation* (SSA) [135], which we state as follows: The properties of the effective medium or an atom at one site may not depend on the specific occupation on any other (alloy) site; this means that this site only 'sees' the effective medium on all alloy sites. The SSA implies that the investigation of site-diagonal (i.e. $\vec{r}_1$ and $\vec{r}_2$ in the same atomic domain/ASA sphere) properties can be reduced to considering a single atom embedded in the effective medium. Conversely, the effective medium can be defined self-consistently by demanding that averaging over such an impurity should retrieve the effective medium. This concept is readily translated to the language of multiple-scattering methods (next section). A disadvantage of the SSA is that effects of a specific local environment (e.g. short-range order, component-specific charge transfers, etc.) are neglected. Further, it cannot be applied to methods where the coupling between two sites depends on their occupation (e.g. tight binding). To overcome these shortcomings, several generalizations of the single-site CPA are considered in the literature (see discussion and references in [A3]).

3.2 Single-site KKR-CPA

In this section we show how the single-site CPA can be implemented in the KKR multiple-scattering method [A4, A3, 150]. The derivation in this section follows refs. [135, 24]. We use the *R-H* formulation of the KKR method[6] [150], which leads to a multiple-scattering equation for the structural GF g (see appendix A.2). In the KKR-CPA the effective medium is described by t-matrices $\bar{t}^n$, which are placed on the alloy sites. They are chosen so as to restore the symmetry of the underlying crystal structure. Of course, the usual atomic t-matrices are placed on non-alloy sites, thus the full t-matrix is

$$\bar{t} = \Big\{ \delta_{nm} \begin{cases} \bar{t}^n & \text{if } n \text{ is an alloy site} \\ t^n & \text{if } n \text{ is a non-alloy site} \end{cases} \Big\}. \tag{3.2}$$

The effective medium $\bar{t}$ is site-diagonal and thus independent of $\vec{k}$ after Fourier transform. This is a consequence of the SSA [102]. The t-matrix describes the scattering properties of the effective medium (relation between incoming and outgoing partial waves); internal properties like scattering solutions inside the ASA sphere or a 'potential' are not accessible within the KKR-CPA method (see also section 3.4). Since $\bar{t}$ has the crystal symmetry, the effective medium structural GF

$$\bar{g} = \big(g_0^{-1} - \bar{t}\big)^{-1} \tag{3.3}$$

can be calculated with the usual methods for periodic systems, i.e. the (Bloch-)Fourier transform. For layer systems with semi-infinite leads this is applied in-plane while the perpendicular direction is treated by the decimation technique [150]; in this case (and also in the corresponding supercell) a separate effective medium $\bar{t}^n$ is considered for each layer.

In order to derive the self-consistent condition we investigate an arbitrary but fixed configuration of the alloy; this is described by a t-matrix where the atomic t-matrix of one of the components is placed on each alloy site. Note that because of the SSA we only need to consider one potential and t-matrix for each component of the alloy (which otherwise would depend on the environment). It will prove beneficial to use the effective medium as a reference system. Thus, the GF for this system is calculated from

$$g = \big(\bar{g}^{-1} - \Delta t\big)^{-1} \quad \text{with} \quad \Delta t = t - \bar{t}. \tag{3.4}$$

Using the tools of multiple scattering [150, 42] we rewrite g in terms of the T-matrix as

$$g = \bar{g} + \bar{g}\, T\, \bar{g} \quad \text{where} \tag{3.5a}$$

$$T = \Delta t + \Delta t\, \bar{g}\, T \tag{3.5b}$$

$$= \Big\{ x^n \big(\delta_{nm} + \sum_{i \neq n} \bar{g}^{ni}\, T^{im}\big) \Big\}. \tag{3.5c}$$

In the last step T was expressed in terms of the excess scattering matrix x. Assuming that in the fixed configuration the alloy site i is occupied by atom type α (i.e. $t^{ii} = t^i_\alpha$) the latter is given by

$$x^i = x^i_\alpha = \big((\Delta t^i_\alpha)^{-1} - \bar{g}^{ii}\big)^{-1} \quad \text{with} \quad \Delta t^i_\alpha = t^i_\alpha - \bar{t}^i. \tag{3.6}$$

For non-alloy sites x^i is zero. Next, we calculate the alloy average $\langle g \rangle$ over all configurations. Since $\bar{g}$ does not depend on the configuration we need to calculate $\langle T \rangle$. Using the expansion of T in terms of x we find

$$\langle T^{nm} \rangle = \Big\langle x^n \big(\delta_{nm} + \sum_{i \neq n} \bar{g}^{ni}\, T^{im}\big) \Big\rangle \approx \langle x^n \rangle \Big(\delta_{nm} + \sum_{i \neq n} \bar{g}^{ni}\, \langle T^{im} \rangle\Big). \tag{3.7}$$

In the second step alloy averages for different elements of T were decoupled neglecting correlations between different sites. This *single-site decoupling* [135] is an important consequence of the SSA

[6] In [A3] we used the *Z-J* version, where the multiple-scattering equation is given in terms of the scattering path operator τ; one can show that both versions lead to identical descriptions for the CPA.

(and often used synonymously). Since the goal is to describe the alloy average by the effective medium, we require

$$\langle g \rangle = \bar{g} \quad \text{which means} \quad \langle T \rangle = 0. \tag{3.8}$$

Using the single-site decoupling eq. (3.7) this is fulfilled if $\langle x^i \rangle = 0$ for all sites. Hence, we obtain the single-site CPA condition (c^i_α is the concentration of alloy component α at site i)

$$\bar{x}^i = \langle x^i \rangle = \sum_\alpha c^i_\alpha \, x^i_\alpha = 0 \quad \text{for all alloy sites } i, \tag{3.9}$$

which demands that replacing the effective medium at a single alloy site with one of the components on average should not produce additional scattering. This condition can be rewritten in terms of the component-resolved GFs g^i_α or the impurity matrices D^i_α as

$$\sum_\alpha c^i_\alpha \, g^i_\alpha = \bar{g}^{ii} \quad \text{or} \quad \sum_\alpha c^i_\alpha \, D^i_\alpha = \sum_\alpha c^i_\alpha \, \tilde{D}^i_\alpha = 1 \tag{3.10a}$$

$$\text{where} \quad g^i_\alpha = D^i_\alpha \, \bar{g}^{ii} = \bar{g}^{ii} \, \tilde{D}^i_\alpha = \left((\bar{g}^{ii})^{-1} - \Delta t^i_\alpha \right)^{-1} \tag{3.10b}$$

$$\text{with} \quad D^i_\alpha = \left(1 - \bar{g}^{ii} \, \Delta t^i_\alpha \right)^{-1} = 1 + \bar{g}^{ii} \, x^i_\alpha \tag{3.10c}$$

$$\text{and} \quad \tilde{D}^i_\alpha = \left(1 - \Delta t^i_\alpha \, \bar{g}^{ii} \right)^{-1} = 1 + x^i_\alpha \, \bar{g}^{ii}.$$

This allows an alternative interpretation, namely that the effective medium GF is the average of the component GFs. The impurity matrix D^i_α (or $\tilde{D}^i_\alpha$) introduced here basically projects the site-diagonal effective medium GF $\bar{g}^{ii}$ onto the component GF g^i_α; this is discussed in detail in section 3.4. Of course, the CPA conditions are equivalent for alloy sites which are related by the underlying crystal structure. For non-equivalent alloy sites in the primitive cell the conditions are coupled via $\bar{g}$ and need to be fulfilled simultaneously. When the effective medium has been obtained and the CPA condition is satisfied, we can calculate physical properties of the alloy, e.g. the density; this often requires component-resolved GFs (section 3.4). For a discussion of the DFT treatment in combination with the CPA see [A3].

Eqs. (3.9) or (3.10) contain the effective medium $\bar{t}$ in a non-linear way (in particular via $\bar{g}$) and cannot be solved directly. We use an iterative method explained in the following. The iteration is started from the average t-matrix approximation

$$\bar{t}^{\,i\,(0)} = \sum_\alpha c^i_\alpha \, t^i_\alpha. \tag{3.11}$$

In each iteration the effective medium GF $\bar{g}^{(j)}$ is calculated from $\bar{t}^{(j)}$ via eq. (3.3). Then, we calculate $\bar{x}^{i\,(j)} = \sum_\alpha c^i_\alpha \, x^{i\,(j)}_\alpha$, where the $x^{i\,(j)}_\alpha$ are obtained using eq. (3.6). If the CPA condition eq. (3.9) is not fulfilled in the iteration, i.e. $\bar{x}^{i\,(j)} \neq 0$ for some site i, we obtain $\bar{t}$ for the next iteration from the following idea [101, 49]. The excess scattering created by the new effective medium relative to the old one should be equal to $\bar{x}^{i\,(j)}$, i.e. the residual excess scattering is integrated in the new effective medium

$$\bar{x}^{i\,(j)} = \left(\left(\bar{t}^{\,i\,(j+1)} - \bar{t}^{\,i\,(j)} \right)^{-1} - \bar{g}^{ii\,(j)} \right)^{-1};$$

from this we obtain the new effective medium t-matrix

$$\bar{t}^{\,i\,(j+1)} = \bar{t}^{\,i\,(j)} + \left((\bar{x}^{i\,(j)})^{-1} + \bar{g}^{ii\,(j)} \right)^{-1}. \tag{3.12}$$

It has been shown [101] that this iterative scheme always converges. In rare cases, however, numerical errors can lead to instabilities, which can be averted by symmetrization of $\bar{t}$, i.e. by ensuring that $\bar{t}$ possesses all space-group symmetries.

3.3 Vertex corrections

In this section we investigate the alloy average of a two-particle expression (i.e. an expression involving a product of two single-electron GFs) of the form $\langle G(z_1)\, A\, G(z_2)\rangle$ for some operator A [A4]. Expressions of this form arise e.g. in linear-response theory (Kubo formula) [102] or the NEGF formalism, in particular the Keldysh equation (2.14c). The derivation follows ref. [134], see also [26, 74, 73]. In the derivation we assume that operator A is independent of the alloy configuration. In the intended applications this is in fact the case: If we use an ordered material for the lead (and the coupling region) the operator Γ_l describing the coupling to the lead (eq. (2.18b)) is configuration independent. Conversely, this means we can only consider disorder inside the middle region. In cases when the operator acts inside the alloy (often in linear-response theory), it usually depends on the occupation; a derivation for this case is given in [24].

The two GFs may have different (complex) energy arguments; an energy dependence of operator A does not play a role in this derivation. Because of the application to NEGFs we label $g^<_A(z_1, z_2) = g(z_1)\, A\, g(z_2)$, where operator A is now in the KKR basis. The energy arguments are suppressed in intermediate steps; they can be recovered by noting that operators left of A (or later Ω_A) in a product carry z_1, while those right of A carry z_2. The goal is to calculate the alloy average $\langle g^<_A\rangle$. We start by inserting the GF in the form of eq. (3.5)

$$\begin{aligned}\bar{g}^<_A = \langle g^<_A\rangle = \langle g\, A\, g\rangle &= \big\langle (\bar{g} + \bar{g}\, T\, \bar{g})\, A\, (\bar{g} + \bar{g}\, T\, \bar{g})\big\rangle \\ &= \bar{g}\big(\langle A\rangle + \langle T\, \bar{g}\, A\rangle + \langle A\, \bar{g}\, T\rangle + \langle T\, \bar{g}\, A\, \bar{g}\, T\rangle\big)\bar{g}, \end{aligned} \tag{3.13}$$

where we used that $\bar{g}$ is independent of the configuration. This expression simplifies notably if we assume that A does not depend on the alloy configuration. We further use that the effective medium fulfills the CPA condition (i.e. eq. (3.8): $\langle T\rangle = 0$). Thus, we obtain

$$\bar{g}^<_A = \langle g\, A\, g\rangle = \bar{g}\, A\, \bar{g} + \bar{g}\, \Omega_A\, \bar{g} \quad \text{with} \quad \Omega_A = \langle T\, \bar{g}\, A\, \bar{g}\, T\rangle, \tag{3.14}$$

where the *vertex corrections* Ω_A were defined [134]. To simplify the vertex corrections we express T in terms of x-matrices (eq. (3.5c))

$$\begin{aligned}\Omega^{nm}_A &= \sum_{n',m'} \Big\langle T^{nn'} \big[\bar{g}\, A\, \bar{g}\big]_{n'm'} T^{m'm}\Big\rangle \\ &= \sum_{n',m'} \left\langle x^n \Big(\delta_{nn'} + \sum_{i\neq n} \bar{g}^{ni}\, T^{in'}\Big) \big[\bar{g}\, A\, \bar{g}\big]_{n'm'} \Big(\delta_{m'm} + \sum_{j\neq m} T^{m'j}\, \bar{g}^{jm}\Big) x^m \right\rangle \\ &\approx \sum_{n',m'} \left\langle x^n \left\langle \Big(\delta_{nn'} + \sum_{i\neq n} \bar{g}^{ni}\, T^{in'}\Big) \big[\bar{g}\, A\, \bar{g}\big]_{n'm'} \Big(\delta_{m'm} + \sum_{j\neq m} T^{m'j}\, \bar{g}^{jm}\Big) \right\rangle x^m \right\rangle, \end{aligned} \tag{3.15}$$

where in the last step we used the single-site decoupling [134]. For $n \neq m$ the two x-matrices in the outer average are independent and thus the average vanishes because of the CPA condition. Consequently, we find that the vertex corrections are site-diagonal $\Omega^{nm}_A = \delta_{nm}\, \Omega^n_A$. The inner average can be simplified considering only the $n = m$ term and again using the CPA condition

$$\begin{aligned}&\sum_{n',m'} \left\langle \Big(\delta_{nn'} + \sum_{i\neq n} \bar{g}^{ni}\, T^{in'}\Big) \big[\bar{g}\, A\, \bar{g}\big]_{n'm'} \Big(\delta_{m'n} + \sum_{j\neq n} T^{m'j}\, \bar{g}^{jn}\Big) \right\rangle \\ &\quad = \big[\bar{g}\, A\, \bar{g}\big]_{nn} + \sum_{n',i\neq n} \bar{g}^{ni} \big\langle T^{in'}\big\rangle \big[\bar{g}\, A\, \bar{g}\big]_{n'n} + \sum_{m',j\neq n} \big[\bar{g}\, A\, \bar{g}\big]_{nm'} \big\langle T^{m'j}\big\rangle\, \bar{g}^{jn} \\ &\qquad + \sum_{\substack{n',i\neq n \\ m',j\neq n}} \bar{g}^{ni} \underbrace{\Big\langle T^{in'} \big[\bar{g}\, A\, \bar{g}\big]_{n'm'} T^{m'j}\Big\rangle}_{\Omega^{ij}_A} \bar{g}^{jn} \\ &\quad = \big[\bar{g}\, A\, \bar{g}\big]_{nn} + \sum_{\substack{i\neq n \\ j\neq n}} \bar{g}^{ni}\, \delta_{ij}\, \Omega^i_A\, \bar{g}^{jn} = \big[\bar{g}\, A\, \bar{g}\big]_{nn} + \sum_{i\neq n} \bar{g}^{ni}\, \Omega^i_A\, \bar{g}^{in}, \end{aligned}$$

where in the last two steps we recognized the definition of Ω_A and used that it is diagonal. With this, we obtain a closed set of equations for the vertex corrections (reintroducing energy arguments)

$$\Omega_A^n = \left\langle x^n(z_1)\Big(\big[\bar{g}(z_1)\, A\, \bar{g}(z_2)\big]_{nn} + \sum_{i\neq n} \bar{g}^{ni}(z_1)\, \Omega_A^i\, \bar{g}^{in}(z_2)\Big)\, x^n(z_2)\right\rangle \tag{3.16a}$$

$$= \sum_\alpha c_\alpha^n\, x_\alpha^n(z_1)\Big(\big[\bar{g}(z_1)\, A\, \bar{g}(z_2)\big]_{nn} + \sum_{i\neq n} \bar{g}^{ni}(z_1)\, \Omega_A^i\, \bar{g}^{in}(z_2)\Big)\, x_\alpha^n(z_2) \tag{3.16b}$$

$$= \sum_\alpha c_\alpha^n\, x_\alpha^n(z_1)\Big(\bar{g}_A^{<,nn}(z_1,z_2) - \bar{g}^{nn}(z_1)\, \Omega_A^n\, \bar{g}^{nn}(z_2)\Big)\, x_\alpha^n(z_2) \tag{3.16c}$$

$$\text{with}\quad \bar{g}_A^<(z_1,z_2) = \bar{g}(z_1)\, A\, \bar{g}(z_2) + \bar{g}(z_1)\, \Omega_A\, \bar{g}(z_2), \tag{3.16d}$$

where in the first step the alloy average was carried out and in the last step the sum over i was completed. It is important to note that the equation above gives a linear relation between the vertex corrections and the operator A. In our case this allows to separate the contributions from different leads and to calculate them independently of the occupation. For a discussion on how the equation is implemented in practice see ref. [A4].

3.4 Restricted averages – Single-particle Green's function

In order to calculate (site-diagonal) physical quantities like the density, we need the GF for an atom of one component placed on a single alloy site while the alloy average is taken over all other sites, i.e. the component-resolved GF. This is calculated by taking the corresponding restricted alloy average [150, 45]. This is necessary, since the effective medium does not provide scattering solutions (i.e. wave functions) and since we are often interested in properties of the individual components. For non-site-diagonal quantities like the Bloch spectral density we also need restricted averages, where two sites are fixed.

To derive the averaged GF for the restricted case $\langle g\rangle_{i=\alpha}$, where site i is fixed to type α, we repeat the steps in section 3.2 leading to eq. (3.7), including the single-site decoupling, and obtain

$$\langle g\rangle_{i=\alpha} = \bar{g} + \bar{g}\,\langle T\rangle_{i=\alpha}\,\bar{g} \quad \text{with} \quad \langle T^{nm}\rangle_{i=\alpha} \approx \langle x^n\rangle_{i=\alpha}\Big(\delta_{nm} + \sum_{j\neq n} \bar{g}^{nj}\,\langle T^{jm}\rangle_{i=\alpha}\Big). \tag{3.17}$$

In principle, we could introduce a new effective medium for the restricted case. However, this would not be very useful, since the fixed site i breaks the desired periodicity. Further, this would not be consistent with the SSA, since the effective medium on sites near to i would be influenced by the coupling to the fixed site via $\bar{g}$. To be consistent with the SSA the effective medium on one site must not depend on the specific occupation of any other (alloy) site, including site i. Therefore, we require that the effective medium for the restricted case on any alloy site except i is identical to the (converged) effective medium for the full average. Effectively, this means that we need to calculate the GF for the case that the effective medium t-matrix for a single site i in the crystal has been replaced by the t-matrix of atom type α. This can be obtained via the Dyson equation starting from the full effective medium

$$\langle g\rangle_{i=\alpha} = \big(\bar{g}^{-1} - \Delta t^{(1)}\big)^{-1} \quad \text{with} \quad \Delta t^{(1)} = \big\{\, \delta_{nmi}\,(t_\alpha^i - \bar{t}^i)\,\big\} = \big\{\, \delta_{nmi}\,\Delta t_\alpha^i\,\big\}, \tag{3.18}$$

where $\bar{t}$ ($\bar{g}$) is the converged effective medium (GF) with respect to the full average. Since $\Delta t^{(1)}$ is non-zero only for site i, so are $x^{(1)}$ and $T^{(1)}$

$$T^{(1)} = \langle T\rangle_{i=\alpha} = x^{(1)} = \big\{\, \delta_{nmi}\, x_\alpha^i\,\big\}, \tag{3.19}$$

with x_α^i given in eq. (3.6). Using this we calculate the restrictedly averaged GF

$$\langle g\rangle_{i=\alpha} = \bar{g} + \bar{g}\,T^{(1)}\,\bar{g} = \big\{\, \bar{g}^{nm} + \bar{g}^{ni}\, x_\alpha^i\, \bar{g}^{im}\,\big\}; \tag{3.20}$$

for $n = i$ or $m = i$ this simplifies to

$$\langle g^{im} \rangle_{i=\alpha} = D^i_\alpha \, \bar{g}^{im} \quad \text{and} \quad \langle g^{ni} \rangle_{i=\alpha} = \bar{g}^{ni} \, \tilde{D}^i_\alpha, \tag{3.21}$$

where D^i_α and $\tilde{D}^i_\alpha$ are given in eq. (3.10c), and for $n = m = i$ we obtain $\langle g^{ii} \rangle_{i=\alpha} = g^i_\alpha$ given in eq. (3.10b) [45]. Usually, only g^i_α is required. With this, we find the KKR-CPA expressions for the site-diagonal component-resolved and averaged real-space GF

$$G^i_\alpha(z; \vec{r}_i, \vec{r}_i') = \langle G^i(z; \vec{r}_i, \vec{r}_i') \rangle_{i=\alpha} = R^i_\alpha(z; \vec{r}_i) \, g^i_\alpha(z) \, R^i_\alpha(z; \vec{r}_i')^\times + G^i_{sc,\alpha}(z; \vec{r}_i, \vec{r}_i') \tag{3.22a}$$

$$\bar{G}^i(z; \vec{r}_i, \vec{r}_i') = \langle G^i(z; \vec{r}_i, \vec{r}_i') \rangle = \sum_\alpha c^i_\alpha \, G^i_\alpha(z; \vec{r}_i, \vec{r}_i') \tag{3.22b}$$

As already shown in section 3.2 the site-diagonal component-resolved structural GFs are consistent with the effective medium GF (see eq. (3.10)). More generally, $\sum_\alpha c^i_\alpha \, \langle g \rangle_{i=\alpha} = \bar{g}$ also follows directly from eq. (3.20) using eq. (3.9).

The approach for the two-site restricted average is similar. We fix site i to type α and site j to type β. From the discussion above this means we have

$$\langle g \rangle_{\substack{i=\alpha \\ j=\beta}} = \left(\bar{g}^{-1} - \Delta t^{(2)} \right)^{-1} \quad \text{with} \quad \Delta t^{(2)} = \left\{ \, \delta_{nmi} \, \Delta t^i_\alpha + \delta_{nmj} \, \Delta t^j_\beta \, \right\}. \tag{3.23}$$

Since the corresponding $x^{(2)} = \left\{ \, \delta_{nmi} \, x^i_\alpha + \delta_{nmj} \, x^j_\beta \, \right\}$ has only two non-zero elements, we find four non-vanishing elements for $T^{(2)}$ coupled by a set of four equations (using eq. (3.5c))

$$T^{ii} = x^i_\alpha + x^i_\alpha \, \bar{g}^{ij} \, T^{ji} \qquad T^{ij} = x^i_\alpha \, \bar{g}^{ij} \, T^{jj} \qquad T^{ji} = x^j_\beta \, \bar{g}^{ji} \, T^{ii} \qquad T^{jj} = x^j_\beta + x^j_\beta \, \bar{g}^{ji} \, T^{ij},$$

which has the solution

$$\begin{aligned} T^{ii} &= \left(\left(x^i_\alpha \right)^{-1} - \bar{g}^{ij} \, x^j_\beta \, \bar{g}^{ji} \right)^{-1} & T^{ij} &= \left(\left(x^i_\alpha \, \bar{g}^{ij} \, x^j_\beta \right)^{-1} - \bar{g}^{ji} \right)^{-1} \\ T^{ji} &= \left(\left(x^j_\beta \, \bar{g}^{ji} \, x^i_\alpha \right)^{-1} - \bar{g}^{ij} \right)^{-1} & T^{jj} &= \left(\left(x^j_\beta \right)^{-1} - \bar{g}^{ji} \, x^i_\alpha \, \bar{g}^{ij} \right)^{-1}. \end{aligned} \tag{3.24}$$

With this the two-site restrictedly averaged GF is given by

$$\langle g^{nm} \rangle_{\substack{i=\alpha \\ j=\beta}} = \bar{g}^{nm} + \bar{g}^{ni} \, T^{ii} \, \bar{g}^{im} + \bar{g}^{ni} \, T^{ij} \, \bar{g}^{jm} + \bar{g}^{nj} \, T^{ji} \, \bar{g}^{im} + \bar{g}^{nj} \, T^{jj} \, \bar{g}^{jm}, \tag{3.25}$$

which for $n = i$ or $m = j$ simplifies to

$$\langle g^{im} \rangle_{\substack{i=\alpha \\ j=\beta}} = D^i_\alpha \, S \left(\bar{g}^{im} + \bar{g}^{ij} \, x^j_\beta \, \bar{g}^{jm} \right) \tag{3.26a}$$

$$\langle g^{nj} \rangle_{\substack{i=\alpha \\ j=\beta}} = \left(\bar{g}^{nj} + \bar{g}^{ni} \, x^i_\alpha \, \bar{g}^{ij} \right) \tilde{S} \, \tilde{D}^j_\beta. \tag{3.26b}$$

Here,

$$S = \left(1 - \bar{g}^{ij} \, x^j_\beta \, \bar{g}^{ji} \, x^i_\alpha \right)^{-1} \quad \text{and} \quad \tilde{S} = \left(1 - x^j_\beta \, \bar{g}^{ji} \, x^i_\alpha \, \bar{g}^{ij} \right)^{-1} = (\bar{g}^{ij})^{-1} \, S \, \bar{g}^{ij} \tag{3.26c}$$

is the common denominator of the non-zero elements of $T^{(2)}$ (eq. (3.24)). It describes repeated scattering between the two fixed sites and, to be consistent with the SSA, this must be neglected [45] (i.e. we set $S = \tilde{S} = 1$). Thus, we obtain the non-site-diagonal elements

$$g^{ij}_{\alpha\beta} = \langle g^{ij} \rangle_{\substack{i=\alpha \\ j=\beta}} = D^i_\alpha \, \bar{g}^{ij} \, \tilde{D}^j_\beta \tag{3.27}$$

for the component-resolved structural GF, and

$$G^{ij}_{\alpha\beta}(z; \vec{r}_i, \vec{r}_j') = \langle G^{ij}(z; \vec{r}_i, \vec{r}_j') \rangle_{\substack{i=\alpha \\ j=\beta}} = R^i_\alpha(z; \vec{r}_i) \, g^{ij}_{\alpha\beta}(z) \, R^j_\beta(z; \vec{r}_j')^\times \tag{3.28a}$$

$$\bar{G}^{ij}(z; \vec{r}_i, \vec{r}_j') = \langle G^{ij}(z; \vec{r}_i, \vec{r}_j') \rangle = \sum_{\alpha,\beta} c^i_\alpha \, c^j_\beta \, G^{ij}_{\alpha\beta}(z; \vec{r}_i, \vec{r}_j') \tag{3.28b}$$

for the component-resolved and averaged real-space GF [45]. An important identity which the two-site restricted average must fulfill is

$$\sum_\beta c_\beta^j \, g_{\alpha\beta}^{ij} = \langle g^{ij} \rangle_{i=\alpha} \quad \text{and} \quad \sum_\alpha c_\alpha^i \, g_{\alpha\beta}^{ij} = \langle g^{ij} \rangle_{j=\beta}, \tag{3.29}$$

i.e. the consistency with the single-site restricted average eq. (3.21). This follows directly from the CPA condition (eq. (3.10)), but only if we set $S = 1$. Note that, since the two fixed sites must be distinct, the expressions are not valid for $i = j$.

3.5 Restricted averages – Two-particle Green's function

In this section we calculate the (single-site) restricted average for a two-particle expression. This is required to obtain component-resolved NEGFs. We proceed similar to section 3.3 keeping track of additional terms arising from the restricted average. The approach has similarities to the one in ref. [24]. We use results obtained in section 3.4; in particular, we describe the restricted average by replacing the effective medium t-matrix on one site i with the atomic t-matrix for type α. We also utilize the result for the T-matrix relative to the effective medium eq. (3.19). After replacing the full averages with restricted ones, we evaluate the general expression eq. (3.13) (suppressing energy arguments and the operator $(\cdot)_A$ index)

$$\begin{aligned} \langle g^< \rangle_{i=\alpha} &= \langle g \, A \, g \rangle_{i=\alpha} \\ &= \bar{g} \left(A + \langle T \rangle_{i=\alpha} \, \bar{g} \, A + A \, \bar{g} \, \langle T \rangle_{i=\alpha} + \langle T \, \bar{g} \, A \, \bar{g} \, T \rangle_{i=\alpha} \right) \bar{g} \\ &= \bar{g} \left(A + x^{(1)} \, \bar{g} \, A + A \, \bar{g} \, x^{(1)} + \Omega_{i=\alpha} \right) \bar{g} \\ &\quad \text{with} \quad \Omega_{i=\alpha} = \langle T \, \bar{g} \, A \, \bar{g} \, T \rangle_{i=\alpha}. \end{aligned} \tag{3.30}$$

For site i this simplifies to (using eq. (3.10c))

$$\begin{aligned} g_\alpha^{<,i} = \langle g^{<,ii} \rangle_{i=\alpha} &= [\bar{g} \, A \, \bar{g}]_{ii} + \bar{g}^{ii} \, x_\alpha^i \, [\bar{g} \, A \, \bar{g}]_{ii} + [\bar{g} \, A \, \bar{g}]_{ii} \, x_\alpha^i \, \bar{g}^{ii} + [\bar{g} \, \Omega_{i=\alpha} \, \bar{g}]_{ii} \\ &= D_\alpha^i \, [\bar{g} \, A \, \bar{g}]_{ii} \, \tilde{D}_\alpha^i - \bar{g}^{ii} \, x_\alpha^i \, [\bar{g} \, A \, \bar{g}]_{ii} \, x_\alpha^i \, \bar{g}^{ii} + [\bar{g} \, \Omega_{i=\alpha} \, \bar{g}]_{ii}. \end{aligned} \tag{3.31}$$

Next, we need to evaluate $\Omega_{i=\alpha}^{nm} = \left[\langle T \, \bar{g} \, A \, \bar{g} \, T \rangle_{i=\alpha} \right]_{nm}$; it is convenient to consider the possible cases for the site indices n, m separately.

- $\Omega_{i=\alpha}^{nm}$ for $n \neq i$ and $m \neq i$
  In this case we could perform an expansion similar to the one in section 3.3. This would lead to additional terms resulting from the special case for site i. However, taking these into account would not be consistent with the SSA. Therefore, following the arguments in section 3.4, we require that vertex corrections for site indices not including i are identical to the vertex corrections obtained for the full average, i.e.

$$\Omega_{i=\alpha}^{nm} = \Omega^{nm} = \delta_{nm} \, \Omega^n \quad \text{for} \quad n \neq i \text{ and } m \neq i. \tag{3.32a}$$

- $\Omega_{i=\alpha}^{im}$ for $m \neq i$ (i.e. $n = i$)
  We expand the left T-matrix and obtain

$$\begin{aligned} \Omega_{i=\alpha}^{im} &= \sum_{n'} x_\alpha^i \left\langle \left(\delta_{in'} + \sum_{j \neq i} \bar{g}^{ij} \, T^{jn'} \right) [\bar{g} \, A \, \bar{g} \, T]_{n'm} \right\rangle_{i=\alpha} \\ &= x_\alpha^i \left(\left[\bar{g} \, A \, \bar{g} \, \langle T \rangle_{i=\alpha} \right]_{im} + \sum_{j \neq i} \bar{g}^{ij} \left[\langle T \, \bar{g} \, A \, \bar{g} \, T \rangle_{i=\alpha} \right]_{jm} \right). \end{aligned}$$

  The first term vanishes since $\langle T \rangle_{i=\alpha} \propto \{\delta_{nmi}\}$ and $m \neq i$. In the second term we recognize the vertex corrections and note that both indices are unequal to i. Thus, using eq. (3.32a) we find

$$\begin{aligned} \Omega_{i=\alpha}^{im} &= \sum_{j \neq i} x_\alpha^i \, \bar{g}^{ij} \, \Omega_{i=\alpha}^{jm} = \sum_{j \neq i} x_\alpha^i \, \bar{g}^{ij} \, \delta_{jm} \, \Omega^m \\ &= x_\alpha^i \, \bar{g}^{im} \, \Omega^m \quad \text{for} \quad m \neq i. \end{aligned} \tag{3.32b}$$

- $\Omega^{ni}_{i=\alpha}$ for $n \neq i$ (i.e. $m = i$)
  We expand the right T-matrix and proceed analogously to the previous case to obtain

$$\Omega^{ni}_{i=\alpha} = \Omega^n \, \bar{g}^{ni} \, x^i_\alpha \quad \text{for} \quad n \neq i. \tag{3.32c}$$

- $\Omega^{ii}_{i=\alpha}$ (i.e. $n = m = i$)
  In this case we need to expand both T-matrices

$$\begin{aligned}
\Omega^{ii}_{i=\alpha} &= \sum_{n'\,m'} x^i_\alpha \left\langle \left(\delta_{in'} + \sum_{j\neq i} \bar{g}^{ij}\, T^{jn'}\right) [\bar{g}\, A\, \bar{g}]_{n'm'} \left(\delta_{m'i} + \sum_{j'\neq i} T^{m'j'}\, \bar{g}^{j'i}\right)\right\rangle_{i=\alpha} x^i_\alpha \\
&= x^i_\alpha \Big([\bar{g}\, A\, \bar{g}]_{ii} + \sum_{j\neq i} \bar{g}^{ij} \left[\langle T\rangle_{i=\alpha}\, \bar{g}\, A\, \bar{g}\right]_{ji} + \sum_{j'\neq i} \left[\bar{g}\, A\, \bar{g}\, \langle T\rangle_{i=\alpha}\right]_{ij'} \bar{g}^{j'i} \\
&\quad + \sum_{\substack{j\neq i \\ j'\neq i}} \bar{g}^{ij} \left[\langle T\, \bar{g}\, A\, \bar{g}\, T\rangle_{i=\alpha}\right]_{jj'} \bar{g}^{j'i} \Big) \, x^i_\alpha.
\end{aligned}$$

  Again, the second and third term vanish and the last one is the vertex corrections for the full average. Thus, we obtain

$$\begin{aligned}
\Omega^{ii}_{i=\alpha} &= x^i_\alpha \Big([\bar{g}\, A\, \bar{g}]_{ii} + \sum_{\substack{j\neq i \\ j'\neq i}} \bar{g}^{ij}\, \Omega^{jj'}_{i=\alpha}\, \bar{g}^{j'i} \Big) \, x^i_\alpha \\
&= x^i_\alpha \Big([\bar{g}\, A\, \bar{g}]_{ii} + \sum_{j\neq i} \bar{g}^{ij}\, \Omega^j\, \bar{g}^{ji} \Big) \, x^i_\alpha.
\end{aligned} \tag{3.32d}$$

For the restrictedly averaged two-particle GF $g^{<,i}_\alpha$ we need to evaluate $[\bar{g}\, \Omega_{i=\alpha}\, \bar{g}]_{ii}$, where we distinguish the above cases

$$\begin{aligned}
[\bar{g}\, \Omega_{i=\alpha}\, \bar{g}]_{ii} &= \sum_{\substack{n\neq i \\ m\neq i}} \bar{g}^{in}\, \Omega^{nm}_{i=\alpha}\, \bar{g}^{mi} + \sum_{n\neq i} \bar{g}^{in}\, \Omega^{ni}_{i=\alpha}\, \bar{g}^{ii} + \sum_{m\neq i} \bar{g}^{ii}\, \Omega^{im}_{i=\alpha}\, \bar{g}^{mi} + \bar{g}^{ii}\, \Omega^{ii}_{i=\alpha}\, \bar{g}^{ii} \\
&= \sum_{n\neq i} \bar{g}^{in}\, \Omega^n\, \bar{g}^{ni} + \sum_{n\neq i} \bar{g}^{in}\, \Omega^n\, \bar{g}^{ni}\, x^i_\alpha\, \bar{g}^{ii} + \sum_{m\neq i} \bar{g}^{ii}\, x^i_\alpha\, \bar{g}^{im}\, \Omega^m\, \bar{g}^{mi} \\
&\quad + \bar{g}^{ii}\, x^i_\alpha \Big([\bar{g}\, A\, \bar{g}]_{ii} + \sum_{n\neq i} \bar{g}^{in}\, \Omega^n\, \bar{g}^{ni} \Big) \, x^i_\alpha\, \bar{g}^{ii} \\
&= \sum_{n\neq i} \big(1 + \bar{g}^{ii}\, x^i_\alpha\big)\, \bar{g}^{in}\, \Omega^n\, \bar{g}^{ni} \left(1 + x^i_\alpha\, \bar{g}^{ii}\right) + \bar{g}^{ii}\, x^i_\alpha\, [\bar{g}\, A\, \bar{g}]_{ii}\, x^i_\alpha\, \bar{g}^{ii} \\
&= \sum_{n\neq i} D^i_\alpha\, \bar{g}^{in}\, \Omega^n\, \bar{g}^{ni}\, \tilde{D}^i_\alpha + \bar{g}^{ii}\, x^i_\alpha\, [\bar{g}\, A\, \bar{g}]_{ii}\, x^i_\alpha\, \bar{g}^{ii} \\
&= D^i_\alpha\, [\bar{g}\, \Omega\, \bar{g}]_{ii}\, \tilde{D}^i_\alpha - D^i_\alpha\, \bar{g}^{ii}\, \Omega^i\, \bar{g}^{ii}\, \tilde{D}^i_\alpha + \bar{g}^{ii}\, x^i_\alpha\, [\bar{g}\, A\, \bar{g}]_{ii}\, x^i_\alpha\, \bar{g}^{ii}.
\end{aligned}$$

Entering this in eq. (3.31) we finally obtain for the restricted average of the two-particle expression

$$\begin{aligned}
g^{<,i}_\alpha(z_1, z_2) &= \Big\langle \big[g(z_1)\, A\, g(z_2)\big]_{ii} \Big\rangle_{i=\alpha} \\
&= D^i_\alpha(z_1) \Big(\big[\bar{g}(z_1)\, A\, \bar{g}(z_2)\big]_{ii} + \big[\bar{g}(z_1)\, \Omega\, \bar{g}(z_2)\big]_{ii} - \bar{g}^{ii}(z_1)\, \Omega^i\, \bar{g}^{ii}(z_2) \Big) \, \tilde{D}^i_\alpha(z_2) \qquad (3.33) \\
&= D^i_\alpha(z_1) \left(\bar{g}^{<,ii}(z_1, z_2) - \bar{g}^{ii}(z_1)\, \Omega^i\, \bar{g}^{ii}(z_2)\right) \tilde{D}^i_\alpha(z_2) \qquad (3.34) \\
&\quad \text{with} \quad \bar{g}^<(z_1, z_2) = \big\langle g(z_1)\, A\, g(z_2)\big\rangle = \bar{g}(z_1)\, A\, \bar{g}(z_2) + \bar{g}(z_1)\, \Omega\, \bar{g}(z_2)
\end{aligned}$$

For convenience we note that $\tilde{D}^i_\alpha(z^*) = D^i_\alpha(z)^\dagger$. An important identity which the restricted average must fulfill is

$$\bar{g}^{<,ii} = \big\langle [g\, A\, g]_{ii} \big\rangle = \sum_\alpha c^i_\alpha \left\langle [g\, A\, g]_{ii} \right\rangle_{i=\alpha} = \sum_\alpha c^i_\alpha\, g^{<,i}_\alpha. \tag{3.35}$$

To show this we note that for some expression $(\cdot)$ independent of α we have

$$\begin{aligned}\sum_\alpha c^i_\alpha\, D^i_\alpha\,(\cdot)\,\tilde{D}^i_\alpha &= \sum_\alpha c^i_\alpha \left(1+\bar{g}^{ii}\,x^i_\alpha\right)(\cdot)\left(1+x^i_\alpha\,\bar{g}^{ii}\right)\\ &= \Big(\sum_\alpha c^i_\alpha\Big)(\cdot) + \bar{g}^{ii}\Big(\sum_\alpha c^i_\alpha\, x^i_\alpha\Big)(\cdot) + (\cdot)\Big(\sum_\alpha c^i_\alpha\, x^i_\alpha\Big)\bar{g}^{ii} + \bar{g}^{ii}\Big(\sum_\alpha c^i_\alpha\, x^i_\alpha\,(\cdot)\,x^i_\alpha\Big)\bar{g}^{ii}\\ &= (\cdot) + \bar{g}^{ii}\Big(\sum_\alpha c^i_\alpha\, x^i_\alpha\,(\cdot)\,x^i_\alpha\Big)\bar{g}^{ii}, \end{aligned} \tag{3.36}$$

where the second and third term vanished because of the CPA condition. In the present case we have $(\cdot) = \bar{g}^{<,ii} - \bar{g}^{ii}\,\Omega^i\,\bar{g}^{ii}$ and in the last term we recognize the vertex corrections eq. (3.16c). This cancels with the second term in eq. (3.34). Thus, we verify that eq. (3.35) is fulfilled for the restrictedly averaged GFs obtained in this section.

For the special case of a binary alloy, the restricted averages can also be obtained in a different way using projection operators [73, A4]. The derivation and the equivalence of the results to the general expressions in this section are discussed in appendix B.1. Recently, an alternative approach to NEGF+CPA has been proposed [70, 155], where the CPA is applied directly to contour GFs. This is discussed (in a modified notation) in appendix B.2. It yields vertex corrections and one-side restrictedly averaged GFs $g^{<,i}_\alpha$ as given above. Since this alternate approach allows for a simpler derivation, we use it to derive the two-site restricted average of the two-particle expression $g^{<,ij}_{\alpha\beta}$ (see eq. (B.21)).

3.6 Bloch spectral density

The Bloch spectral density [45] (BSF for Bloch spectral function) is the density of states resolved with respect to the Bloch vector $\vec{k}$. To derive an expression for the BSF we first note that for a periodic system (in equilibrium or ground state) the real-space gDOS is also periodic

$$A(E;\vec{r}+\vec{T},\vec{r}'+\vec{T}) = A(E;\vec{r},\vec{r}') = A(E;\vec{r}_0,\vec{r}'_0+\vec{T}'), \tag{3.37}$$

where $\vec{r}_0$ and $\vec{r}'_0$ are restricted to the primitive cell V_0, which uniquely determines $\vec{T}'$. Thus, its Bloch-Fourier transform (or $\vec{k}$-th projection [150]) is diagonal in $\vec{k}$ (and also periodic with respect to reciprocal lattice vectors)

$$A(E;\vec{k},\vec{r}_0,\vec{r}'_0) = \sum_{\vec{T}} e^{i\,\vec{k}\,\vec{T}}\,A(E;\vec{r}_0,\vec{r}'_0+\vec{T}). \tag{3.38}$$

Analogous equations hold for real-space GFs of a periodic system. With this, the BSF can be defined as

$$A^B(E;\vec{k}) = \frac{1}{2\pi}\int_{V_0} \mathrm{d}\vec{r}_0\; A(E;\vec{k},\vec{r}_0,\vec{r}_0) \tag{3.39a}$$

$$= -\frac{1}{\pi}\,\mathrm{Im}\int_{V_0} \mathrm{d}\vec{r}_0\;\sum_{\vec{T}} e^{i\,\vec{k}\,\vec{T}}\,G(E;\vec{r}_0,\vec{r}_0+\vec{T}). \tag{3.39b}$$

By writing the gDOS (or the GF) in terms of Bloch waves, one can show that for a perfect crystal [45]

$$A^B(E;\vec{k}) = \sum_n \delta(E-\epsilon_n(\vec{k})), \tag{3.40}$$

thus in this case the BSF is basically equivalent to the band structure $\epsilon_n(\vec{k})$. When defined in terms of the GF, the BSF can be extended to complex energies. In this case the δ-functions turn into Lorentzians, whose width is determined by the imaginary part of the energy.

Applying eq. (3.39b) to the KKR GF (eq. (A.2a)) of a periodic system results in (see appendix A.2 for notations)

$$A^B(z;\vec{k}) = -\frac{1}{\pi}\,\mathrm{Im}\sum_{\vec{S}}\int_{V_{\vec{S}}}\mathrm{d}\vec{r}\,\left(R^{\vec{S}}(z;\vec{r})\,g^{\vec{S}\vec{S}}(z;\vec{k})\,R^{\vec{S}}(z;\vec{r})^{\times} + G^{\vec{S}}_{sc}(z;\vec{r},\vec{r})\right) \tag{3.41a}$$

$$= -\frac{1}{\pi}\,\mathrm{Im}\sum_{\vec{S}}\mathop{\mathrm{Tr}}_{L}\int_0^{r^{\vec{S}}_{ASA}}\mathrm{d}r\;r^2\left(\tilde{R}^{\vec{S}}(z;r)\,g^{\vec{S}\vec{S}}(z;\vec{k})\,\tilde{R}^{\vec{S}}(z;r) + \tilde{G}^{\vec{S}}_{sc}(z;r,r)\right), \tag{3.41b}$$

where we used that the scattering solutions are independent of $\vec{T}$ and the single-scatterer GF contributes only for $\vec{T}=0$. In the second step the angular integration was performed assuming ASA potentials, which results in a trace over the angular momentum index. This expression allows a decomposition of the BSF into separate contributions from different atoms (via the site index $\vec{S}$), angular momenta L, and also spins σ (suppressed in this section). If IRRs for the group of $\vec{k}$ are known, a useful decomposition can be obtained in terms of the corresponding basis functions, i.e. the lattice harmonics. Since the IRR is a quantum number of the eigenstates at $\vec{k}$, this facilitates separating contributions from different states. From the discussion in section 2.5 this means that we need to transform from spherical harmonics to lattice harmonics and take the trace over all basis functions of an IRR.

In alloys the gDOS (or GF) for a fixed configuration usually has no spatial symmetries and in particular is not periodic. However, taking the full configuration average restores the underlying space group symmetry (for the substitutional alloys considered in this work). In particular, this is true for the CPA averages. Thus, we can extend the BSF to this case by using the CPA averaged GF. When calculating the Bloch-Fourier transform of the latter, one needs to consider the different form of site-diagonal (eq. (3.22b)) and non-site-diagonal terms (eq. (3.28b)). This results in [45]

$$\begin{aligned} A^B_{\vec{S}}(z;\vec{k}) = -\frac{1}{\pi}\,\mathrm{Im}\int_{V_{\vec{S}}}\mathrm{d}\vec{r}\,\Big(&\sum_{\alpha,\beta} c^{\vec{S}}_\alpha\, c^{\vec{S}}_\beta\, R^{\vec{S}}_\alpha(z;\vec{r})\, D^{\vec{S}}_\alpha(z)\,\bar{g}^{\vec{S}\vec{S}}(z;\vec{k})\,\tilde{D}^{\vec{S}}_\beta(z)\,R^{\vec{S}}_\beta(z;\vec{r})^{\times} \\ &- \sum_{\alpha,\beta} c^{\vec{S}}_\alpha\, c^{\vec{S}}_\beta\, R^{\vec{S}}_\alpha(z;\vec{r})\, D^{\vec{S}}_\alpha(z)\,\bar{g}^{\vec{S}\vec{S}}(z)\,\tilde{D}^{\vec{S}}_\beta(z)\,R^{\vec{S}}_\beta(z;\vec{r})^{\times} \\ &+ \sum_{\alpha} c^{\vec{S}}_\alpha\left(R^{\vec{S}}_\alpha(z;\vec{r})\, D^{\vec{S}}_\alpha(z)\,\bar{g}^{\vec{S}\vec{S}}(z)\,R^{\vec{S}}_\alpha(z;\vec{r})^{\times} + G^{\vec{S}}_{sc,\alpha}(z;\vec{r},\vec{r})\right)\Big), \end{aligned} \tag{3.42}$$

where the second and third term are independent of $\vec{k}$ and may be considered as a correction which becomes necessary because of the SSA [45]. Because Bloch waves are not eigenstates of the alloy, the BSF does not consist of δ-functions. Since the Bloch waves are scattered by disorder, they obtain a finite lifetime, which results in a broadening of the bands. Since the CPA effective medium restores the full symmetry of the space group we can also obtain a decomposition in terms of IRRs as discussed above.

It is possible to obtain the BSF of an alloy by an alternative approach using supercells [109]. In the band structure of a large supercell the bands are 'folded' into the much smaller Brillouin zone, which makes an interpretation difficult. However, by mapping the eigenstates onto Bloch states of the parent lattice, a BSF in the original Brillouin zone can be defined; this procedure is called unfolding [109]. In the terms of this section, we can obtain an unfolded BSF by imposing a Bloch-Fourier transform of the parent lattice on the gDOS of the supercell. This is no longer diagonal in $\vec{k}$, but we are only interested in the diagonal part. Assuming that the supercell comprises N_S primitive cells at $\vec{T}_1 \cdots \vec{T}_{N_S}$ we define the unfolded BSF as the average over the N_S sites

$$A^B_{\vec{S}}(z;\vec{k}) = \frac{1}{N_S}\int_{V_{\vec{S}}}\mathrm{d}\vec{r}\;\sum_{i,j=1}^{N_S} e^{i\,\vec{k}\,(\vec{T}_j-\vec{T}_i)}A(z;\tilde{\vec{k}},\vec{S}+\vec{T}_i+\vec{r},\vec{S}+\vec{T}_j+\vec{r}), \tag{3.43}$$

where $\tilde{\vec{k}}$ is the Bloch vector onto which $\vec{k}$ is folded.

A BSF can equally be defined for the non-equilibrium density. We only need to replace A with its non-equilibrium counterpart. This method, in particular in combination with a decomposition into IRRs, allows a detailed analysis of transport processes.

4 Results – Tunnel magnetoresistance

4.1 Electronic structure of FeCo alloys

In this section we discuss the electronic structure of iron (Fe), cobalt (Co), and their binary alloys (we use FeCo as an abbreviation for $Fe_{1-x}Co_x$ with $0 < x < 1$). This topic has already been addressed in [A3]. Here, we use the advanced methods introduced in previous sections to obtain a deep and comprehensive understanding of the electronic states, their symmetry, and the effects of disorder scattering. This provides a sound basis to apprehend the complex transport processes in tunnel junctions containing alloy layers.

In this work we assume that all metals have the equilibrium lattice structure of iron, i.e. a body-centered cubic (bcc) structure with a lattice constant of $a_{\mathrm{Fe}} = 0.287$ nm [142]. This means we neglect a change in the lattice constant or even the lattice structure caused by adding cobalt [A3] (which has a hexagonal close-packed (hcp) equilibrium structure). The intention is to separate purely electronic effects from additional effects caused by the lattice structure. We further assume that the FeCo alloys form completely disordered substitutional alloys, which is a prerequisite for applying the CPA.

The band structure of iron and cobalt is shown in figure 4.1; we focus on the Δ high-symmetry $\vec{k}$-line, which is of great importance in later sections. The Δ-line can be either of the Cartesian axes in $\vec{k}$-space and has C_{4v} symmetry. This point group is discussed in section 2.5 and the corresponding lattice harmonics (appendix A.3) are used to separate the IRRs. As explained in section 2.5 this does not give a complete set of quantum numbers (e.g. two Δ_1 bands appear in figure 4.1 for each spin). However, states of the same symmetry are well separated in energy. Thus, for practical aspects the symmetry allows for a separation of the eigenstates.

Since $_{26}$Fe and $_{27}$Co differ only by one electron (and core charge) the difference in their band structures can, to a large extend, be understood by band filling, which leads to a higher Fermi-energy in Co. Additionally, one can observe a decrease in the exchange splitting (or Stoner splitting) in Co, i.e. the energy difference between majority and minority spin. In combination, both effects lead to a different position of the Fermi-energy relative to the Δ_1 half-metallic region, which is the energy range between the lowest majority $\Delta_1^{\uparrow}$ and minority $\Delta_1^{\downarrow}$ conduction band states.

Following the idea of a VCA (section 3.1), the bands of an FeCo alloy should be describable as an interpolation between both elements. From the BSF of $Fe_{0.5}Co_{0.5}$ shown in figure 4.1 we can see that this is in fact the case for some of the bands. However, some bands show a notable broadening, as expected from the discussion in sections 3 and 3.6. This cannot be understood within a VCA and requires taking into account effects of disorder. The broadening varies strongly with energy, between different bands, $\vec{k}$-points, and both spins. It is most pronounced for the minority spin close above the Fermi-energy. For the $\Delta_1^{\downarrow}$ and $\Delta_2^{\downarrow}$ bands it is so large that an interpretation in terms of a modified band structure (i.e. a quasiparticle interpretation) becomes ambiguous. Since both bands originate from the same doubly degenerate state at Γ ($\Gamma_{12} \rightarrow \Delta_1 + \Delta_2$), they have the same BSF at that $\vec{k}$-point. A close inspection, shown in figure 4.2, reveals that it has a two-peak structure. Along the Δ-line for $\Delta_1^{\downarrow}$ ($\Delta_2^{\downarrow}$) the lower (upper) peak is reduced to a shoulder and decays; however, for the $\Delta_1^{\downarrow}$ states it retains a notable density at the Fermi-energy throughout half of the Brillouin-zone (figure 4.2). A plausible explanation for the two-peak structure is that the states split into iron- and cobalt-like states. To verify this and to obtain a quantitative description of the full concentration dependence we analyze the BSF at the Γ-point as a function of the concentration, shown in figure 4.3. The bands have a rather complicated non-linear concentration dependence. The main reason is the structure of the DOS, which for iron shows a minimum above the Fermi-energy followed by a pronounced peak [A3]; this leads to a non-linear concentration dependence of E_F via band filling. The details of concentration dependence and broadening vary for the four bands. An inspection of the $\Gamma_{12}^{\downarrow}$ band confirms the explanation above: it consists of an iron and a cobalt peak, which maintain their position in energy, only the weight is shifted from the Fe to the Co peak with increasing Co concentration. This explains the strong broadening of these states and the two-peak structure

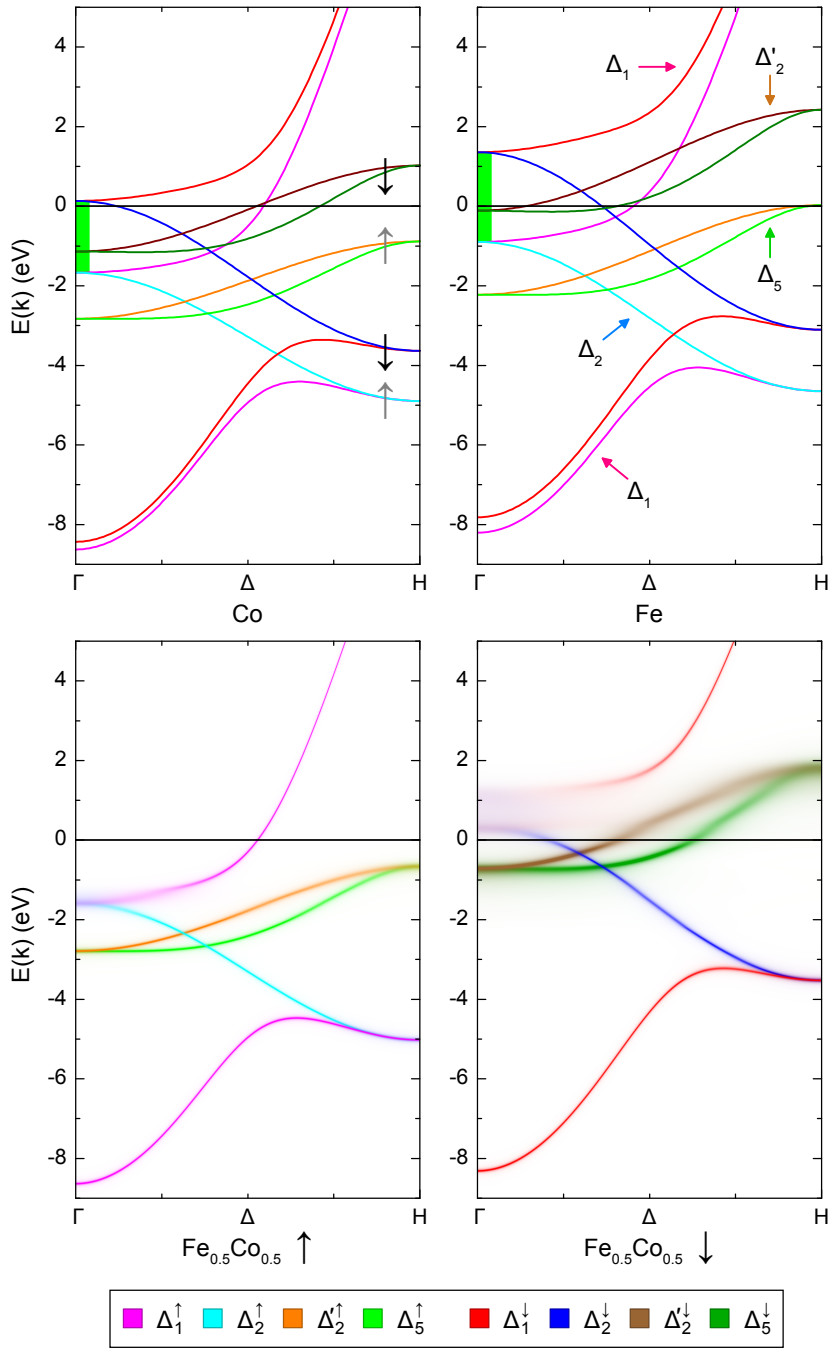

Figure 4.1: (Top) Band structure of (bcc) cobalt and iron along the Δ-line (i.e. $\Gamma - H$) for both spins; the Δ_1 half-metallic energy range is marked;
(Bottom) Bloch spectral density of $Fe_{0.5}Co_{0.5}$ obtained with the CPA, the spin channels are shown in separate plots;
the high-symmetry $\vec{k}$-points are: $\Gamma = \frac{2\pi}{a}\{0,0,0\}$ and $H = \frac{2\pi}{a}\{0,0,1\}$.

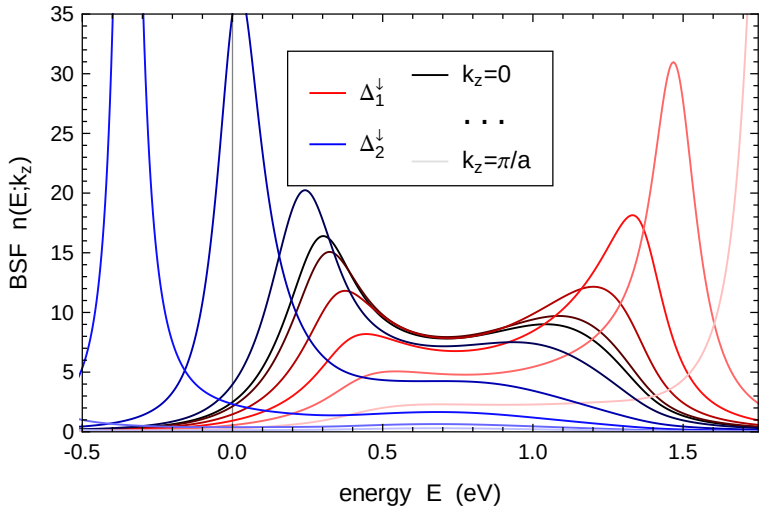

Figure 4.2: Cross sections of the Bloch spectral density shown in figure 4.1 for different k_z values along half of the Δ-line showing only the $\Delta_1^{\downarrow}$ and $\Delta_2^{\downarrow}$ bands.

observed in figure 4.2. A similar effect is observed in the corresponding part of the DOS [A3].

Because of the importance of the peculiar broadening in later sections, we would like to verify that it is not an artifact of the CPA method. This is accomplished by using the alternative approach to BSFs of alloys explained in section 3.6, i.e. by unfolding of supercell band structures. As it turns out, this requires very large supercells even for qualitative results. To reduce the computational costs we use self-consistent CPA potentials to construct the supercell potentials. The result for the full Δ-line is shown in figure 4.4. The strength and distribution of the broadening are in good agreement to the CPA result (figure 4.1). Despite the large supercells the unfolded BSF shows a strong coarseness, which can be attributed to the supercell size. We also investigate the peculiar broadening at the Γ-point in detail, which is shown in figure 4.5. While the two-peak structure is not well reproduced, the overall broadening and in particular the density at the Fermi-energy are in good agreement with the CPA result. The unfolding method offers an alternative interpretation of the CPA results, namely as the projection of the eigenstates of the disordered alloy onto Bloch states of the parent lattice.

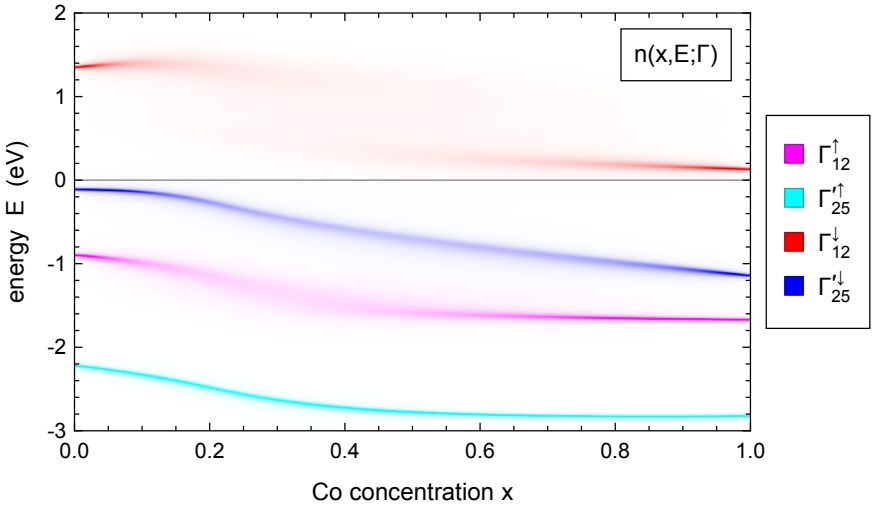

Figure 4.3: Bloch spectral function of $Fe_{1-x}Co_x$ at the Γ-point as a function of Co concentration and energy for both spin; aligned at the respective Fermi-energies.

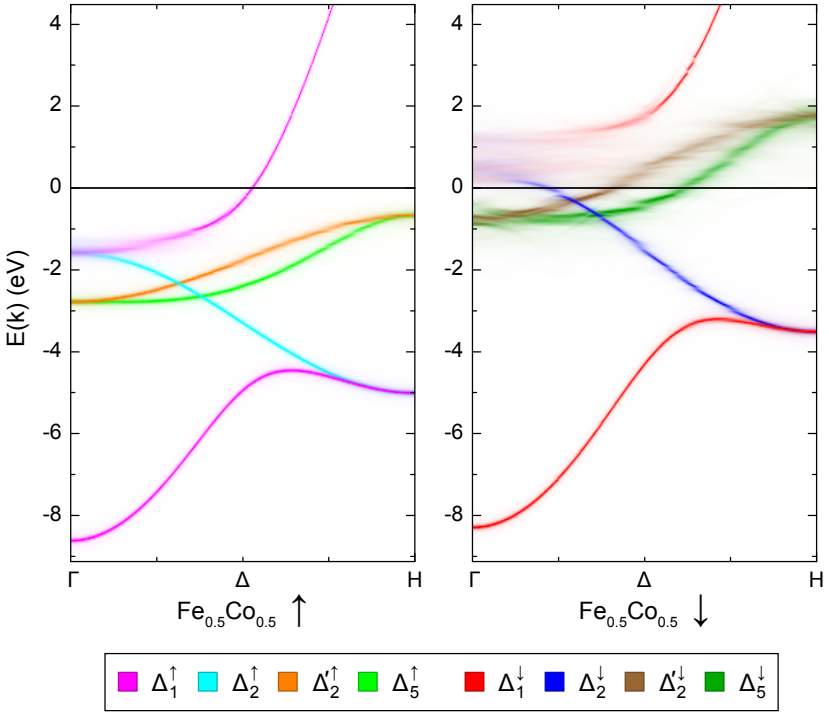

Figure 4.4: Bloch spectral density of $Fe_{0.5}Co_{0.5}$ for both spin channels along the Δ-line obtained by unfolding, averaged over 5 supercells containing 128 atoms

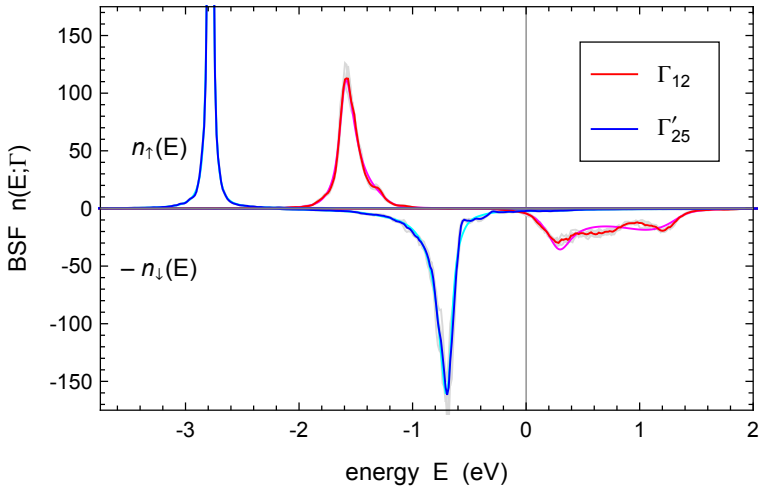

Figure 4.5: Bloch spectral density of $Fe_{0.5}Co_{0.5}$ at Γ obtained by unfolding, averaged over 5 supercells containing 1024 atoms (darker), compared to the CPA result (brighter); the gray lines show the spread within the supercell results.

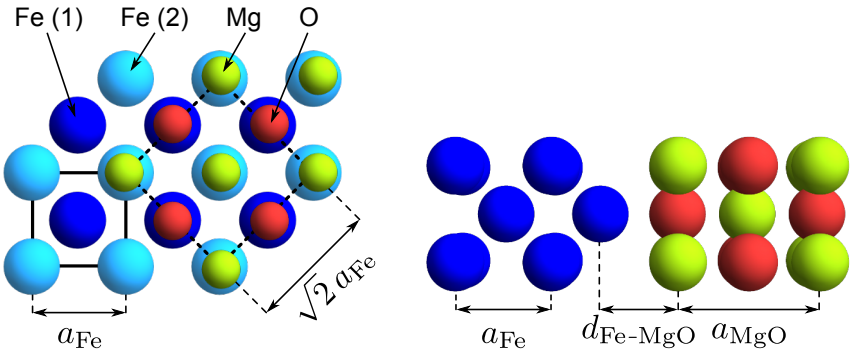

a_{Fe}	$\sqrt{2}\,a_{\mathrm{Fe}}$	$d_{\mathrm{Fe\text{-}MgO}}$	a_{MgO}
0.287 nm	0.405 nm	0.235 nm	0.424 nm

Figure 4.6: Interface structure of magnesium oxide grown epitaxially on iron
(Left) Top view showing the first layer of MgO on top of the first two layers of iron; the squares indicate the cubic cells of both materials; the top face of the iron cell is also the bottom face of the tetragonal MgO cell.
(Right) Side view of the interface structure.
(Table, Bottom) Lattice parameters and distances [142, 29].

4.2 Tunnel magnetoresistance in Fe/MgO/Fe tunnel junctions

In this section we introduce the tunnel magnetoresistance (TMR) in (coherent) magnetic tunnel junctions (MTJ). These junctions consist of two ferromagnetic layers separated by an insulating layer, which is thin enough to allow for a measurable tunneling current. We focus on junctions where the tunneling is coherent, which means that the state (i.e. the energy, spin, $\vec{k}$-vector, and IRR) of the tunneling electrons is preserved. This requires a crystalline barrier and epitaxial interfaces. Coherent MTJs are in contrast to diffusive ones (e.g. with an amorphous AlO_x barrier), where the tunneling is incoherent. The latter ones can be described by the Jullire model in terms of the spin polarization of the DOS at the Fermi-energy (see section 1.1). This simple model is not valid for the coherent MTJs discussed in this work [62].

As a typical example of a coherent MTJ we discuss the case of a magnesium oxide (MgO) barrier separating two semi-infinite iron (Fe) leads. This structure was the first proposed coherent MTJ and has been extensively investigated [131]. It is suitable to introduce the quantum-mechanical effects that lead to the large TMR observed in many coherent MTJs. It has been shown that MgO can be grown epitaxially on Fe (see discussion and refs. in [25, 94]). The resulting interface structure is shown in figure 4.6. In the growth direction (z-direction), which is also the direction of the current in transport calculations, both materials are aligned along their [001] axis. In-plane (i.e. perpendicular to the growth direction) the MgO cubic cell is rotated by 45° and matched to the Fe surface in such a way that the oxygen atoms lie on top of the iron atoms. Because of the lattice mismatch between both materials, the MgO is deformed from its equilibrium rock-salt structure (two interpenetrating face-centered cubic (fcc) lattices with octahedral coordination) to a body-centered tetragonal (bct) structure. The space group of the junction is $P4/nmm$ (D^7_{4h}) (for an even number of atomic MgO layers); however, if the z-direction is fixed by transport boundary conditions, it reduces to $P4mm$ (C^1_{4v}) [126, 127].

The different lattice constants and distances are given in figure 4.6. We assume a simplified structure ('ideal' structure) [29, A5], where the iron maintains its equilibrium structure throughout, while the MgO is compressively strained in-plane by 5% to match the lattice constant of iron. Along the growth direction we assume (about) the equilibrium lattice constant of MgO, although, because of the in-plane compression, an expansion is also feasible. The distance between the last Fe and the first MgO layer is constructed by bringing the MgO surface, including one layer of empty-spheres, to touching distance. The resulting distance is slightly larger than other values considered in the literature [25]. Relaxation of atoms near the interface from the

G_p	$G_{\uparrow\uparrow}$	$G_{\downarrow\downarrow}$	G_{ap}	$G_{\uparrow\downarrow} = G_{\downarrow\uparrow}$	TMR	nTMR
22.3	21.3	1.00	0.495	0.248	4410	95.7

Table 4: Conductance (per junction area) of the Fe/MgO/Fe tunnel junction for the different channels given in units of $10^9\ \Omega^{-1}\mathrm{m}^{-2}$ and tunnel magnetoresistance ratio given in %. Note that the area of the primitive in-plane cell is $A = a_{\mathrm{Fe}}^2 = 0.0821\ \mathrm{nm}^2$.

described positions are not considered. The lattice structure is intentionally kept simple to separate electronic and structural effects. Throughout this work we use a barrier thickness of six atomic layers of MgO (1.27 nm).

To obtain DFT self-consistent potentials for the MTJ, the semi-infinite leads are replaced by finite slabs of 30 Fe layers on each side and the resulting structure is treated as a supercell. The self-consistent potentials (including their Fermi-energy) are used for the transport calculations, where the outermost Fe layers are repeated to produce the leads. The magnetizations in both Fe leads are parallel (P) to each other and (by default) aligned with the z-axis. To calculate the TMR we also need the potentials for anti-parallel (AP) aligned magnetizations; these are obtained by simply replacing spin-up and -down potentials from the middle of the barrier on, without a subsequent self-consistent calculation. This is justified by the strong separation of both leads via the insulating barrier. Strictly speaking, having the magnetization pointing perpendicular to the layers is a special (and particularly interesting) case which only occurs for very thin Fe slabs [A9]. However, since we neglect relativistic effects, in particular spin-orbit interaction, the absolute direction of the magnetization has no physical effect, only the relative alignment of the magnetizations in both leads has.

Using the NEGF method introduced in section 2.2 we calculate the conductance of this junction for P and AP alignment of the magnetizations. In this section we consider the limit of zero bias and zero temperature, where the conductance is obtained in linear response from eq. (2.21) as

$$G = \frac{I_{tot}}{V} = \frac{e^2}{h}\, T(E_F). \tag{4.1}$$

Since in these non-relativistic and collinear calculations both spins are decoupled, we obtain two separate contributions for each alignment, which we denote by $G_{\sigma\sigma'}$ for the conductance between spin σ in the left lead and spin σ' in the right lead. The spins are labeled by $\uparrow$ for the local majority and $\downarrow$ for the minority spin. The total conductance for each alignment is

$$G_p = G_{\uparrow\uparrow} + G_{\downarrow\downarrow} \qquad \text{and} \qquad G_{ap} = G_{\uparrow\downarrow} + G_{\downarrow\uparrow}. \tag{4.2}$$

The results are given in table 4. One immediately notes that the conductance for P is much larger than for AP alignment. This difference can be used to infer the alignment from a conductance measurement. The size of the difference is measured by the (optimistic) TMR ratio

$$\mathrm{TMR} = \frac{G_p - G_{ap}}{G_{ap}} = \frac{R_{ap} - R_p}{R_p} = \frac{I_p - I_{ap}}{I_{ap}}, \tag{4.3}$$

where $R = 1/G$ is the resistance. Alternatively, the normalized TMR ratio (nTMR)

$$\mathrm{nTMR} = \frac{G_p - G_{ap}}{G_p + G_{ap}} = \frac{R_{ap} - R_p}{R_p + R_{ap}} = \frac{I_p - I_{ap}}{I_p + I_{ap}} \tag{4.4}$$

can be used; it is restricted to the interval $(-1, 1)$, whereas the optimistic TMR diverges for $G_{ap} \to 0$. Both ratios are zero for $G_p = G_{ap}$ and in $(-1, 0)$ for $G_p < G_{ap}$. The ratios calculated for the MTJ are given in table 4. Although the very large predicted TMR ratio of over 4000% is not achieved in experiments, the measured values are large, up to about 500% (1000%) at room (low) temperature [146, 84], which is why these MTJs are widely used in applications [131, 147].

4.2.1 Origin of the giant TMR ratio

The main goal of this section is to explain the physical reason for the large TMR value. We show that it is the result of an interplay between the band structure of iron and the (complex) band structure of MgO. This concept has originally been developed by Butler [25] and Umerski [94]; this section is based on their work.

The key is to understand the tunneling process at the $\bar{\Gamma}$-point, i.e. the center of the two-dimensional Brillouin zone. Since the junction is periodic in-plane and we are not considering any disorder scattering (for now), the in-plane $\vec{k}$-vector ($\vec{k}_\parallel$) is conserved. If $\vec{k}_\parallel$ has a non-trivial symmetry group $\mathcal{G}_{\vec{k}_\parallel}$, the IRR of the states (or symmetry, see section 2.5) is also a conserved quantum number. Keeping in mind that the transport direction is fixed, the group of $\bar{\Gamma}$ for the present structure is C_{4v}, which has been introduced in section 2.5. Thus, we can use the lattice harmonics given in appendix A.3 to separate the contributions of different IRRs. As indicated in sections 4.1, this amounts to a separation of the eigenstates in Fe and also in MgO (shown below). In figure 4.7 we show the layer- and IRR-resolved tunneling density of states (TDOS) at $\bar{\Gamma}$ and E_F [25], i.e. the density of only those states connected to the left lead (eq. (2.18)). Since each IRR corresponds to one eigenstate only, each curve has the form expected from a simple tunnel barrier. This means, in the left lead we have a single incoming and the corresponding reflected wave leading to an oscillating density. The wavelength can be compared to the corresponding k_z-value from figure 4.1, although this is difficult in some cases, since we only have one sampling point per atom (or layer). Of course, only states which are present at the Fermi-energy in the spin channel can provide incoming states[7]. In the barrier we find an exponential decay for all IRRs as expected inside the band gap of an insulator. The decay rate depends strongly on the IRR, but not on the spin channel. In the right lead we have either the constant density of a single outgoing wave or another exponential decay, if the incoming IRR is not present at E_F in the outgoing spin channel (compare figure 4.1). In the latter case, iron, although metallic, acts as an insulator for unavailable states.

The outgoing TDOS is closely related to the transmission probability at $\bar{\Gamma}$, which is also given in figure 4.7. In all channels Δ_2' and Δ_2 states (when present) have no significant contribution, since their decay rates in MgO are large and thus their transmission probabilities small in comparison to the others IRRs. Δ_5 states are present in all channels and contribute in a similar way, although the contribution depends on the states in both Fe leads, which are quite different for majority and minority spin. Δ_1 states have by far the smallest decay rate and thus the largest transmission probability. However, they can only contribute in the $\uparrow\uparrow$ channel for P alignment. The reason is that Δ_1 states are not present at E_F in the minority spin of iron, i.e. Fe is half-metallic with respect to Δ_1 states. Therefore, they cannot contribute in any of the other channels: in the $\downarrow\downarrow$ and $\downarrow\uparrow$ channels there are no incoming Δ_1 states and in the $\uparrow\downarrow$ channel the outgoing Δ_1 states decay in the right lead. Consequently, the transmission in the $\uparrow\uparrow$ channel is much larger than in any other channel leading to an (of course purely hypothetical) TMR of $4 \cdot 10^9$ % for the $\bar{\Gamma}$-point.

The different decay rates in MgO are the crucial ingredient, since they lead to a symmetry selection in the barrier. Clearly, this requires coherent tunneling, because otherwise the symmetry (IRR) would not be conserved. Without this effect, we would need a true half-metal to obtain a large TMR. The different decay rates can be understood by investigating the complex band structure of MgO. The complex band structure is a generalization of the usual band structure obtained by reducing the physical boundary conditions to allow exponentially decaying states $\propto e^{-\kappa_z z}$ in one direction (here the z-direction). The decay rate κ_z is regarded as an imaginary part of the Bloch wave vector k_z in this direction. These evanescent states cannot exist in a bulk crystal, but they are important in the vicinity of interfaces for the description of interfaces states or incoming states from another material as in the present case. In particular, neglecting modifications near the interfaces (the complex band structure is calculated in a bulk crystal), the tunneling process can essentially be understood as follows: the incoming states couple to

[7] Actually, by numerical error (because of the necessary artificial broadening) there is a small spurious contribution of the unavailable IRRs, which is suppressed in the figure.

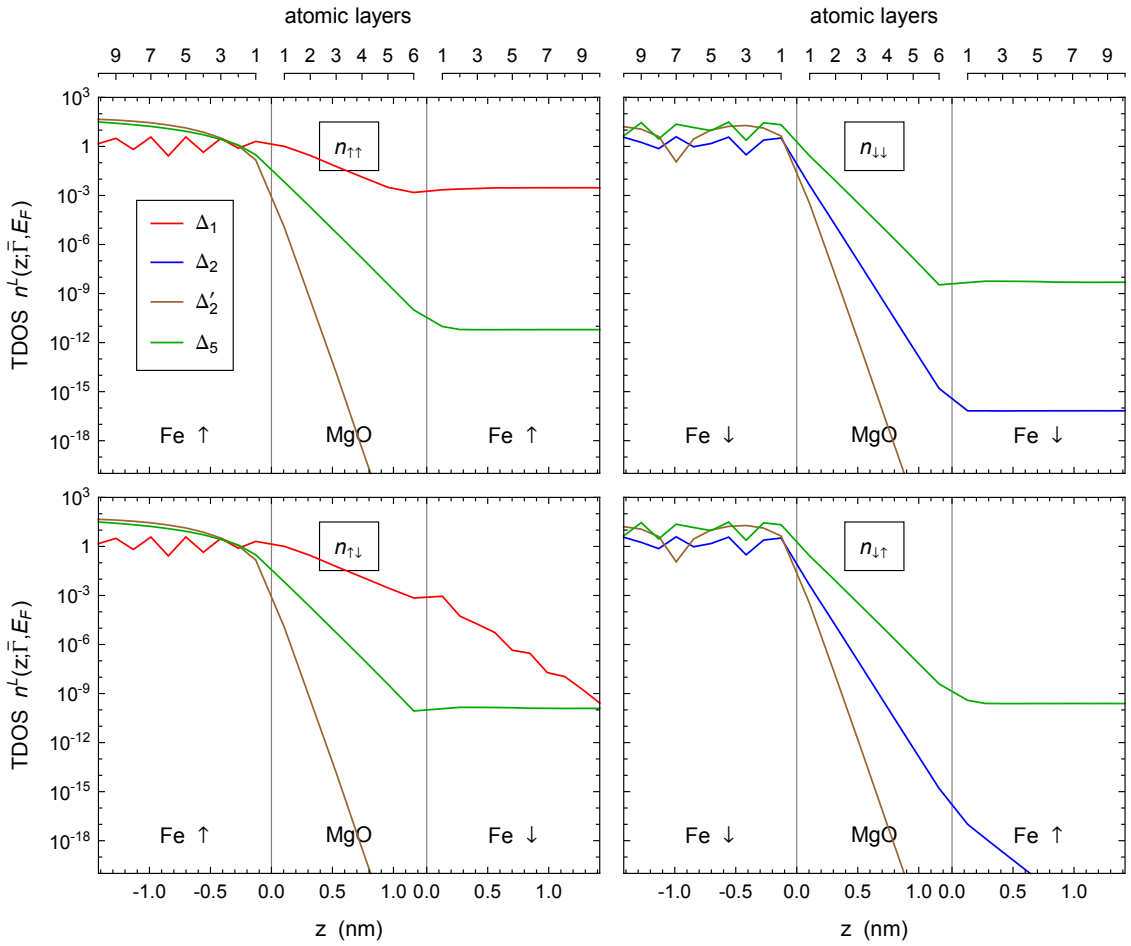

		Δ_1	Δ_2	Δ_2'	Δ_5	sum	
P	$\downarrow\downarrow$	0	$6.64 \cdot 10^{-17}$	0	$1.29 \cdot 10^{-9}$	$1.29 \cdot 10^{-9}$	$2.85 \cdot 10^{-3}$
	$\uparrow\uparrow$	$2.85 \cdot 10^{-3}$	0	0	$8.21 \cdot 10^{-13}$	$2.85 \cdot 10^{-3}$	
AP	$\downarrow\uparrow$	0	0	0	$3.26 \cdot 10^{-11}$	$3.26 \cdot 10^{-11}$	$6.52 \cdot 10^{-11}$
	$\uparrow\downarrow$	0	0	0	$3.26 \cdot 10^{-11}$	$3.26 \cdot 10^{-11}$	

Figure 4.7: (Top) Layer-resolved tunneling density of the states connected to the left lead (TDOS) in the MTJ at the $\bar{\Gamma}$-point and Fermi-energy for the four spin channels $n^L_{\sigma\sigma'}(z;\bar{\Gamma},E_F)$; contributions of the IRRs are shown separately. The TDOS is summed over the atoms in each layer; empty spheres are disregarded.
(Table, Bottom) Transmission $T(\bar{\Gamma},E_F)$ for the different spin channels and IRRs; small values are clipped at 10^{-20}. Note that the $\vec{k}_\parallel$-resolved transmission probability is unitless.

a) body-centered tetragonal

b) face-centered cubic

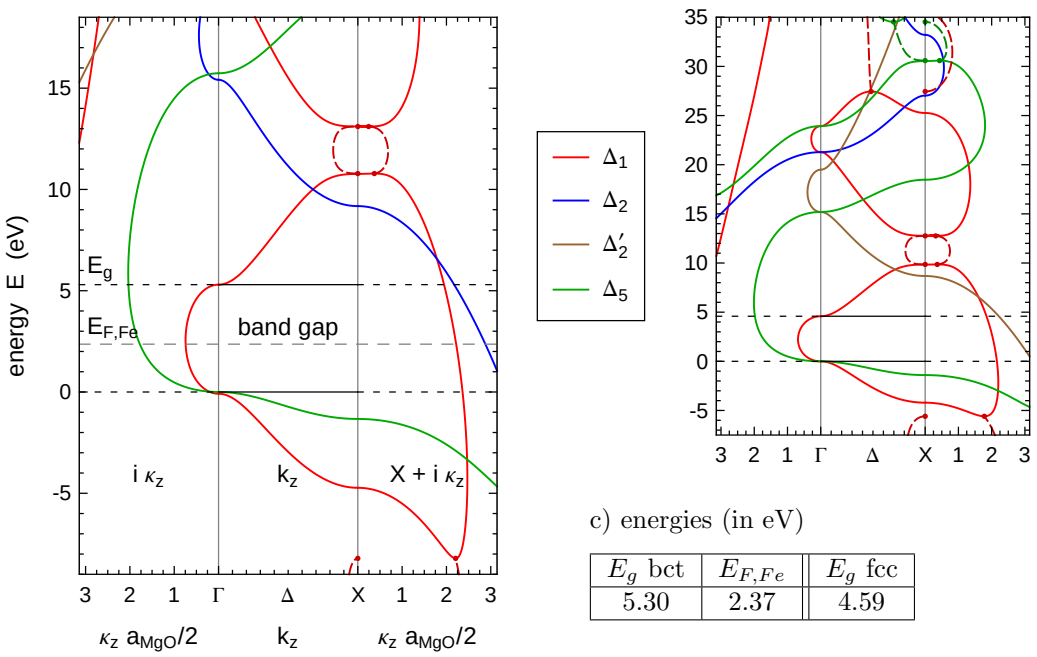

c) energies (in eV)

E_g bct	$E_{F,Fe}$	E_g fcc
5.30	2.37	4.59

Figure 4.8: Complex band structure of MgO in the constrained bct and the equilibrium fcc structur[9] for $k_x = k_y = 0$. The $\vec{k}$-point of symmetry is $X = \frac{2\pi}{a_{\mathrm{MgO}}}\{0, 0, 1\}$. $E_{F,Fe}$ indicates the position of the Fermi-energy in the Fe/MgO/Fe MTJ.

decaying states from the complex band structure, which then couple to the outgoing states.

We calculate the complex band structure of MgO for the constrained bct structure and also in its equilibrium fcc structure for comparison. In both structures $\vec{k}$-vectors the along k_z-axis have C_{4v} symmetry; the IRRs remain valid for the complex band structure. The results for both structures are shown in figure 4.8. Note that the roles of Δ_2 and Δ_2' are interchanged between fcc and bct, since both structures are rotated by 45° relative to each other [25]. Figure 4.8 also shows the position of the Fermi-energy in the Fe/MgO/Fe MTJ relative to the band gap[10]. We find that in our calculation the Fermi-energy is close to the center of the band gap. The decay rates of the various states at E_F can be directly read of and agree well with the ones obtained from the TDOS (figure 4.7) of the inner four MgO layers. Thus, despite a strong impact of the confinement on the states in the MgO barrier (visible in DOS and BSF), the tunneling is well described by the bulk complex band structure. In principle, all complex bands with $k_x = k_y = 0$ contribute to the tunneling at $\bar{\Gamma}$ regardless of their real part of k_z. Thus, there may be several bands at E_F belonging to the same IRR (e.g. for Δ_1). However, the tunneling is always dominated by the band with the smallest decay rate κ_z.

In a similar way, the decay of the evanescent states in iron can be explained using the corresponding complex band structure. Since the specific decay rates are of no importance, this discussion is omitted here. Noteworthy, the peculiar decay of Δ_1 states can be attributed to a mixing of two states, one of them with real part $k_z \neq 0$ [144].

We now extend the discussion to the full two-dimensional Brillouin zone. The $\vec{k}_\parallel$-resolved transmission $T_{\sigma,\sigma'}(\vec{k}_\parallel; E_F)$ is shown in figure 4.9. Integrating it over $\vec{k}_\parallel$ and multiplying by $\frac{e^2}{h}$ yields the conductance shown in table 4. Since the junction is symmetric (i.e. it has a mirror

[9] Usually, different labels are used for the symmetry points and lines in bct structure [20]; for simplicity we use the fcc labels for both cases.

[10] The position of $E_{F,Fe}$ is determined by comparing the band structure of bulk bct MgO to the one obtained by using a MgO potential taken from the center of the barrier.

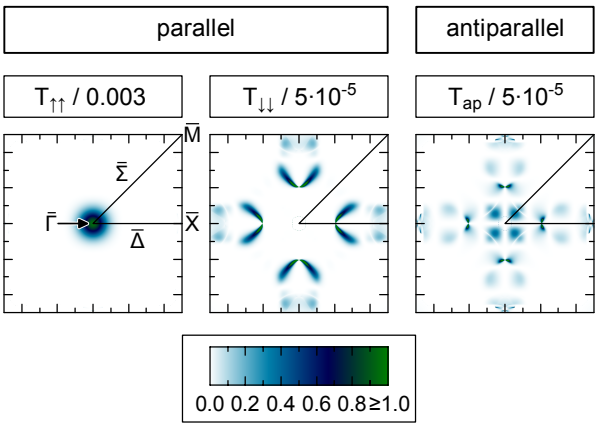

Figure 4.9: Transmission $T_{\sigma,\sigma'}(\vec{k}_\parallel; E_F)$ in the two-dimensional Brillouin zone at the Fermi-energy for the different spin channels; note that $T_{\downarrow\uparrow} = T_{\uparrow\downarrow} = T_{ap}/2$; some sharp peaks are clipped; the $\vec{k}_\parallel$-points of symmetry are $\bar{\Gamma} = \frac{2\pi}{a}\{0,0\}$, $\bar{X} = \frac{2\pi}{a}\{1/2,0\}$, and $\bar{M} = \frac{2\pi}{a}\{1/2,1/2\}$; the lines of symmetry are $\bar{\Delta} = \bar{\Gamma}-\bar{X}$, and $\bar{\Sigma} = \bar{\Gamma}-\bar{M}$

plane in the center), the transmissions for the $\downarrow\uparrow$ and $\uparrow\downarrow$ channel are equal. Of course, a general $\vec{k}_\parallel$-point has no symmetries and the method applied at the $\bar{\Gamma}$-point cannot be used. In general, any band in Fe can couple with any complex band in MgO. The combination of the couplings and decay rates determines the transmission probability. This cannot be described accurately by a simple model. However, in the vicinity of the $\bar{\Gamma}$-point we can argue that e.g. Δ_1-like bands in Fe, i.e. bands which have Δ_1 symmetry at $\bar{\Gamma}$, will couple predominantly to Δ_1-like complex bands in MgO etc. Calculations show [25, 63] that the Δ_1-like complex band with the smallest decay rate at $\bar{\Gamma}$ retains a small decay rate in a large spot around $\bar{\Gamma}$, which also is by far the smallest decay rate of all complex bands at E_F in the entire two-dimensional Brillouin zone. This Δ_1-like band causes the spot around $\bar{\Gamma}$ in the $T_{\uparrow\uparrow}$ channel, which integrates to the large conductance $G_{\uparrow\uparrow}$. In the T_{ap} channel there are some contributions in this region originating from tunneling between bands of different character at $\bar{\Gamma}$ through the Δ_1-like complex bands in MgO. For large barrier thicknesses these contributions limit the TMR [63]. For the thickness considered here, there are also contributions in other regions of the Brillouin zone, where the symmetry selection has no effect. Clearly, there can only be contributions to T_{ap} at $\vec{k}_\parallel$-points where states exist for both spin directions (see also figure 4.10).

4.2.2 Interface resonance states

In order to understand the structure of $T_{\downarrow\downarrow}$ (figure 4.9) we need to take into account effects of the interfaces, which have been disregarded so far. The dominant peaks in $T_{\downarrow\downarrow}$ and also the corresponding peaks in T_{ap} cannot be explained from the bulk bands. They are a result of an interface resonance state (IRS). An IRS occurs when an interface state, i.e. a two-dimensional state localized at an interface, overlaps with a bulk band and couples to it. This can lead to a strongly increased amplitude of the wave function and density at the interface in such a $\vec{k}_\parallel$-region, which also enhances the coupling to the MgO. The IRS responsible for the peaks in $T_{\downarrow\downarrow}$ can be observed in the BSF (section 3.6) at E_F for the interfacial Fe layer shown in figure 4.10. This figure also shows the corresponding bulk BSF for comparison, which further indicates the states available for transport at each $\vec{k}_\parallel$-point. For example, no transport through the MTJ is possible in empty $\vec{k}_\parallel$-regions, where no bulk states are available. Comparing bulk and interfacial BSF shows the strong enhancement caused by the IRS about 2/5 along the $\bar{\Delta}$-line. It also shows a depletion of other states at the interface. This is reasonable, since the MgO acts as an almost impenetrable barrier and thus incoming states have a node at the interface. A closer consideration reveals more IRSs close to the edge of the Brillouin zone for majority spin and in

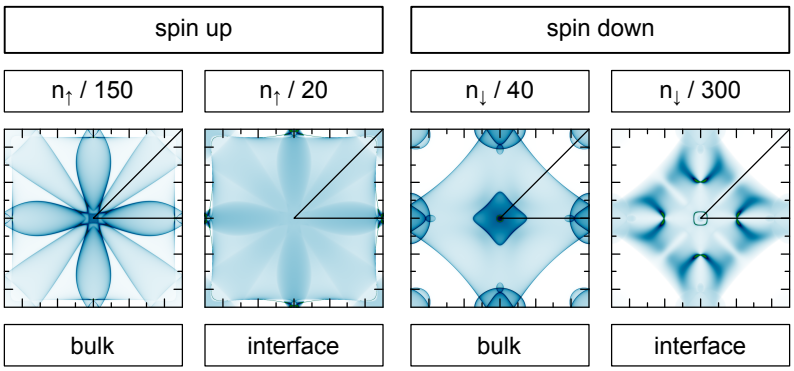

Figure 4.10: Bloch spectral density of iron for the bulk crystal and the Fe/MgO interfacial layer in the two-dimensional Brillouin zone at the Fermi-energy; the bulk density is calculated in the cubic bcc cell and projected (i.e. integrated) along k_z.

the center for minority spin, which can also be observed in the transmission.

To investigate the IRS in more detail we calculate the minority BSF in the interface layer along the $\bar{\Delta}$-line (similar to the investigation in [108] for Fe/Vacuum) and the $\bar{\Sigma}$-line in an energy range around E_F. These $\vec{k}_\parallel$-lines have a mirror symmetry and we can distinguish even and odd states. In figure 4.11 the interfacial BSF is compared to the respective bulk BSF. It turns out that the IRS which causes the peak in figure 4.10 has even symmetry along $\bar{\Delta}$ and a very flat dispersion. It is located around the Fermi-energy in a gap of the even bulk states, which, strictly speaking, makes it an interface state along the symmetry line, since it cannot couple to bulk states. This gap is covered by states with odd symmetry and off the $\bar{\Delta}$-line the IRS can couple to these bulk states leading to the broadening observed in figure 4.10. The interfacial BSF of states with odd symmetry along $\bar{\Delta}$ follows the respective bulk BSF and shows no clear sign of IRSs. Along the $\bar{\Sigma}$-line the IRS has odd symmetry and lies in a gap of the odd bulk states. It crosses the Fermi-energy close to the $\bar{\Gamma}$-point but then stays at least 11 meV above it. Along $\bar{\Sigma}$ we can also observe an interface state close to it above E_F. It lies inside a full gap of the bulk states and has even symmetry. A third IRS is observed 1.32 eV above E_F close to $\bar{\Gamma}$, which has even symmetry along both lines. A closer look reveals several other IRSs, however these are less important for later discussions. For the IRS at higher energies we can analyze the symmetry at $\bar{\Gamma}$, which reveals a Δ_1 character (see figure 4.20). It lies directly below the minority $\Delta_1^\downarrow$ band bottom. The IRS close to E_F disappears right before the $\bar{\Gamma}$-point at the energy where the Δ_2 and Δ_5 bands cross; the characters along both $\vec{k}_\parallel$-lines equally match the splitting rules for Δ_2 and Δ_5; because of the relatively small decay rate [25] we label this IRS Δ_5-like.

It is important to understand the different effects of the IRS at E_F on $T_{\downarrow\downarrow}$ and T_{ap}. In both cases the IRS leads to a significant contribution (figure 4.9). For $T_{\downarrow\downarrow}$ the IRSs on both sides of the barrier are perfectly aligned and the effect is 'squared'. Nevertheless, $T_{\downarrow\downarrow}$ is still small compared to $T_{\uparrow\uparrow}$ and has only a minor impact on the TMR. The perfect alignment is easily disturbed in experimental junctions, which would further reduce the effect [13]. In both channels for AP alignment the IRS occurs only on one side leading to a smaller absolute contribution. However, since both AP channels are equally small, the IRS actually leads to a reduction of the TMR by increasing T_{ap}. Additionally, the impact on T_{ap} is less sensitive to small disturbances at the interfaces. Since the large contributions of the IRS are away from $\bar{\Gamma}$ they cannot couple to the Δ_1-like complex band with the smallest decay rate in MgO. Thus, the (relative) contribution of the IRS reduces strongly with increasing barrier thickness, while it may have a crucial impact for thin barriers [25, 13].

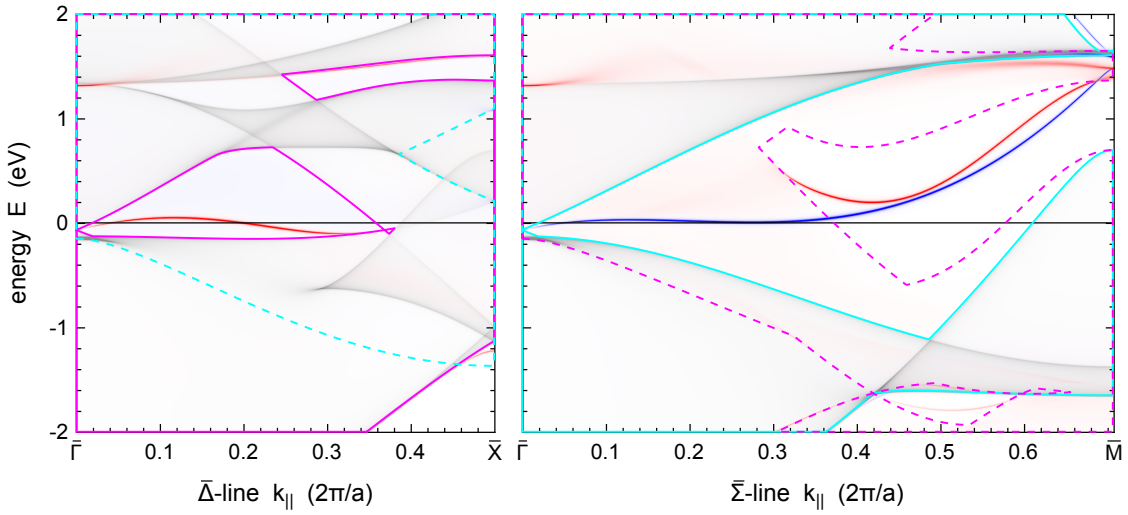

Figure 4.11: Bloch spectral function for the minority spin in the interface Fe layer at an Fe/MgO interface along the $\bar{\Delta}$-line ($\bar{\Gamma}-\bar{X}$) and the $\bar{\Sigma}$-line ($\bar{\Gamma}-\bar{M}$) in the two-dimensional Brillouin zone showing even (red) and odd (blue) states separately; the additional lines indicate the distribution of the respective even (magenta) and odd (cyan) bulk states; the gray background shows the even bulk states along $\bar{\Delta}$ and the odd bulk states along $\bar{\Sigma}$ for comparison.

4.2.3 Experimental results

The large theoretically predicted TMR ratios for coherent MTJs inspired a major effort to achieve these in experiments. Nevertheless, typical TMR values obtained in experimental junctions are one order of magnitude smaller than the predictions [146]. Many different possible reasons have been proposed and investigated in the literature and some are briefly reviewed below. To date, no conclusive explanation for this discrepancy has been found and likely a combination of these and other effects is present. The occurrence/importance of different effects may also depend on details of the structure of the MTJ and on the preparation method and conditions.

When comparing different TMR values some general issues are important. The relative magnitude of different contributions to the conductance depends sensitively on the barrier thickness. Thus, not only the TMR ratio but also its qualitative dependence on some parameter or effect can change considerably with the thickness. The TMR decreases moderately with increasing temperature due to an increase in the AP conductance [105]. Since *ab initio* calculations rarely include finite-temperature effects a comparison is only feasible for low-temperature measurements.

Most of the proposed mechanisms causing a reduction of the TMR are based on structural imperfections in experimental junctions. One possible defect is the formation of an iron(II) oxide (FeO) layer at the interfaces. This effect has been intensively investigated theoretically [153, 61] and experimentally [99, 98]. The formation of FeO can be controlled and prevented by controlling the growth conditions [149, 145]. Recent systematic experiments indicate a rather weak influence of an FeO layer on the TMR [17, 4].

The lattice mismatch between iron and MgO leads to lattice distortions and dislocations at the interfaces and in the barrier [149, 18]. It has been demonstrated experimentally that a high density of dislocations reduces the TMR [18]. These extended defects are difficult to describe computationally and theoretical results have not yet been published. However, it has been shown that oxygen vacancies in the barrier lead to scattering and reduce the TMR [100, 116].

The IRSs are particularly difficult to investigate, since they are very sensitive to the interface structure as well as details in the calculation. Effects of an IRS can be experimentally observed via tunnel spectroscopy, i.e. by investigating derivatives of the tunnel current. The onset of new contributions to the current is visible as peaks in the second derivative d^2I/dV^2. Using this method, peaks at 0.16–0.2 V and 1.0–1.1 V for AP alignment have been attributed to minority

IRSs [151, 90], which may be identified with the Δ_5-like and Δ_1-like IRS. These experiments also show that IRSs are quenched by interface roughness. The calculated AP conductance, which is discussed in section 4.5, shows a rather broad peak at 0.1 V resulting from the Δ_5-like IRS, this creates a maximum in d^2I/dV^2 at about 0.04–0.05 V. It is unclear, whether only the dispersion of the IRS is different in the experiments or if it is shifted to higher energies altogether. Recent calculations using the quasiparticle self-consistent GW approximation predict the IRS at higher energies [44]. The peak resulting from the Δ_1-like IRS falls outside the bias voltage range considered in section 4.5, but a large sharp peak is observed in the energy-dependent AP transmission at 1.32 V in section 4.2.4 in reasonable agreement with the experiments. When interpreting tunnel spectroscopy results, one should keep in mind that they also include other effects, in particular inelastic scattering by magnons and phonons [39, 90], and the assignment may not always be unambiguous.

4.2.4 Energy-dependent transmission

In this section we briefly discuss the energy-dependent transmission for an Fe/MgO/Fe tunnel junction in a large energy range for the different spin channels [113]. Because of the Pauli exclusion principle, the transport properties at zero bias voltage are determined solely by the transmission at the Fermi-energy at zero temperature or in a small energy range around E_F for finite temperatures. Nonetheless, this discussion is instructive, since it shows the influence of various effects on the transmission and it is beneficial for understanding their impact on the transport properties discussed in later sections. The results are summarized in figure 4.12, which shows the energy-dependent transmission as well as the $\vec{k}_\parallel$-resolved transmissions for selected energies and channels. Although this calculation is performed with an increased artificial broadening (see appendix A.5) of $2.71 \cdot 10^{-4}$ eV to reduce the computational costs, some noise is visible in $T_{\downarrow\downarrow}$ resulting from a not fully converged $\vec{k}_\parallel$-mesh. Additionally, only 10 Fe layers on each side of the barrier have been included in the middle region. The main effect of the broadening is to reduce the large peaks in $T_{\downarrow\downarrow}$ related to IRSs. It is likely that a similar effect is present in experiments due to disorder and finite temperature. Therefore, the broadening is used by some authors to simulate 'generic disorder' [113, 133]. On the downside, this broadening leads to a non-conserving approximation, i.e. scattered particles are removed rather than being scattered into a different state. In particular, scattering should reduce the symmetry filtering and thereby the TMR as observed in experiments, however, this is not the case for the artificial broadening [113]. Still, since this section is intended to illustrate the qualitative effects, this approximation is reasonable.

The most prominent features observed in the transmission functions in figure 4.12 are a result of IRSs. When interpreting these peaks, one should keep in mind that they are the result of a complicated interplay of the coupling of the IRS to the Fe bulk bands, the coupling to the evanescent MgO bands and their decay rates, and also of the amplitude of the IRS. The largest peaks are a result of the Δ_1-like IRS. For $T_{\uparrow\uparrow}$ this occurs around -0.95 eV and marks the onset of the $\Delta_1^\uparrow$ band. The latter provides the large dominating contribution to $T_{\uparrow\uparrow}$ in the rest of the shown energy range. This shows relatively little structure with a minimum at 0.11 eV and a moderate increase towards higher energies, which is a result of the energy dependence of the complex Δ_1-like band in MgO. Note that the large contributions from the valence and conduction bands in MgO are far outside the shown energy range. In $T_{\downarrow\downarrow}$ the peak from the $\Delta_1^\downarrow$-like IRS at 1.34 eV is even larger than the one in $T_{\uparrow\uparrow}$; it marks the end of the Δ_1 half-metallic region in Fe. The dispersion and the coupling to bulk states are quite different for the IRS for both spins resulting in the distinct peak shapes. This difference is also visible in the $\vec{k}_\parallel$-resolved transmission shown for the maxima of both peaks. As expected, this also shows that the contributions are located in the center of the Brillouin zone, where the complex Δ_1-like MgO band has a small decay rate. The $\Delta_1^\downarrow$-like IRS also causes a large peak in T_{ap}, since Δ_1-like states become available for both spins

Figure 4.12 includes a detail view of T_{ap} around E_F showing effects of the minority $\Delta_5^\downarrow$-like IRS. This shows that its contribution is not maximal at the Fermi-energy but has two peaks at

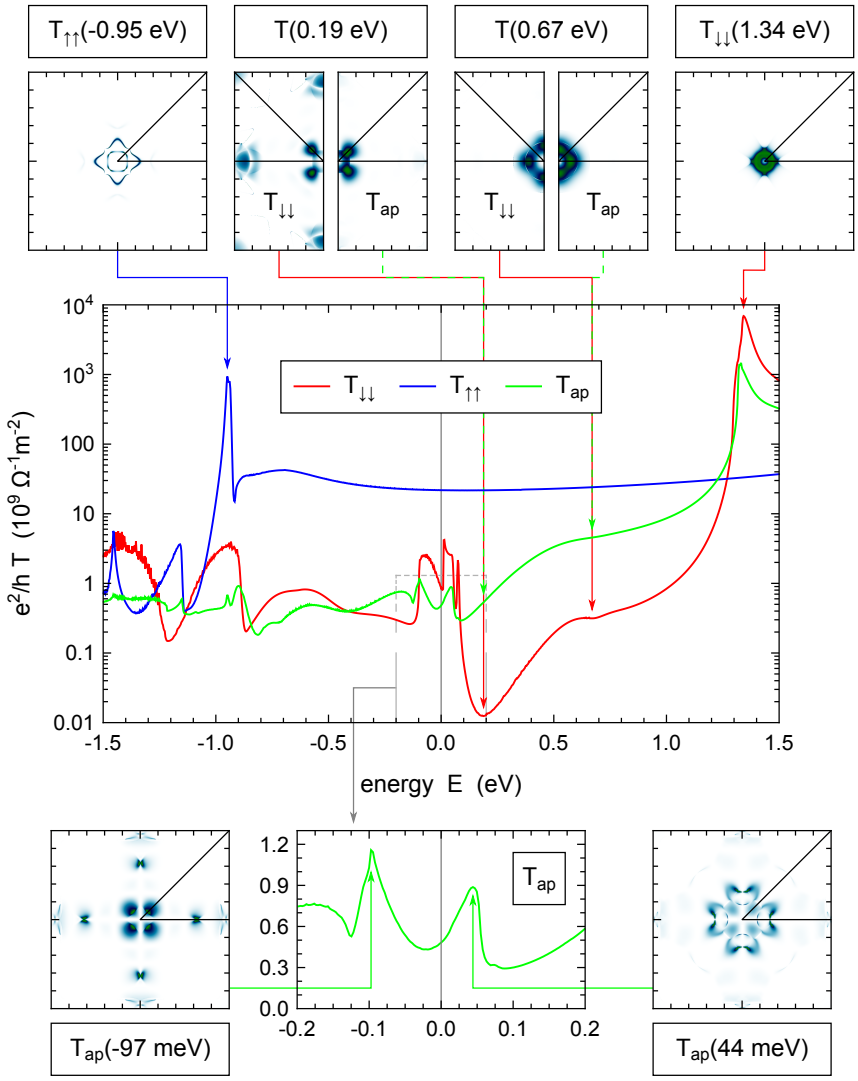

Figure 4.12: Energy-dependent transmission function for the MTJ showing the two spin channels for P alignment and $T_{ap} = T_{\downarrow\uparrow} + T_{\uparrow\downarrow}$ for AP alignment of the magnetizations (center); for some features in the $T(E)$ the $\vec{k}_{\parallel}$-resolved transmission is shown (top,bottom); additionally, a detail plot of T_{ap} is shown (bottom).

-97 meV and 44 meV, where the minimum between both peaks is close to E_F. The $\vec{k}_\parallel$-resolved plots show that for both peaks the contributions are located along the $\bar{\Delta}$-line. Remarkably, the effect of the same IRS on $T_{\downarrow\downarrow}$ is quite different, since in this case the IRSs in both leads are aligned. In particular, $T_{\downarrow\downarrow}$ shows a steep increase directly above E_F, which is related to a saddle point of the IRS along the $\bar{\Sigma}$-line. This has no visible effect on T_{ap}, since the decay rates in MgO are large in this $\vec{k}_\parallel$-region. The contributions of the $\Delta_5^\downarrow$-like IRS end abruptly at about 0.1 eV; for higher energies the IRS lies completely in a gap of the bulk states (compare figure 4.10) and cannot contribute to transport. Above the IRS $T_{\downarrow\downarrow}$ shows a pronounced minimum around 0.2 eV; actually $T_{\downarrow\downarrow}$ appears to have a broad minimum around the Fermi-energy, which is only disrupted by the IRS. This roughly coincides with a minimum in the minority bulk DOS [A3], however the minimum in $T_{\downarrow\downarrow}$ is primarily related to a decreased coupling of the available states to the Δ_1-like complex MgO band around $\bar{\Gamma}$. At higher energies additional states with increased coupling to this complex band become available and lead to an increase in $T_{\downarrow\downarrow}$ around 0.5 eV. A similar but much less pronounced dependence is observed for T_{ap}. A direct comparison of the $\vec{k}_\parallel$-resolved transmissions shows that the same states control the dominating contribution in both cases. Using symmetry arguments we can classify these states further. Since the Δ_1-like states have even symmetry along both symmetry lines ($\bar{\Delta}$ and $\bar{\Sigma}$), we can compare the $\vec{k}_\parallel$-resolved transmission with the available states along both lines shown in figure 4.10. This shows that the minimum in $T_{\downarrow\downarrow}$ and T_{ap} is related to the 'hole' around E_F in the even states along the $\bar{\Delta}$-line.

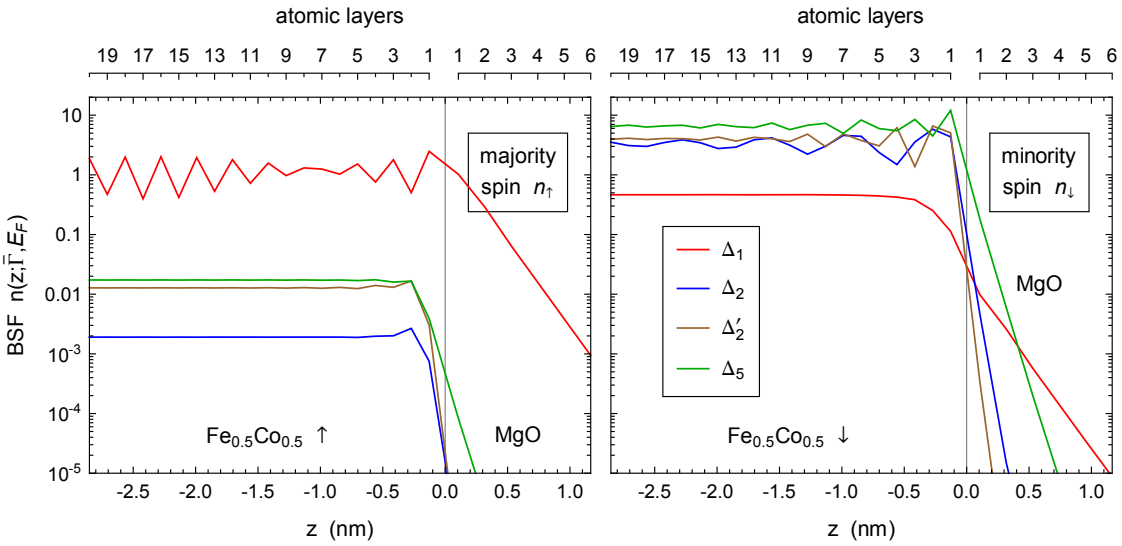

Figure 4.13: Layer-resolved Bloch spectral density at E_f and $\bar{\Gamma}$ for an $Fe_{0.5}Co_{0.5}$/MgO interface; both spins and the IRRs are shown separately.

4.3 Alloy leads — The effect of disorder

In this section we extend the discussion of MTJs from section 4.2 by replacing the iron leads with disordered FeCo leads. Many of the substantial changes in this case are not a result of the band filling (which could be described by a VCA) but result from the disorder scattering, which is included in the CPA description. This means the transport electrons can be (elastically) scattered between different states at the same energy, in particular different $\vec{k}_{\parallel}$-points and IRRs.

We start by investigating the (equilibrium) density at E_F for a single interface between FeCo and MgO (both semi-infinite) in the same structure as the interfaces in the MTJs. To obtain an effective medium for the semi-infinite FeCo lead, we copy the one from the outermost CPA site in the middle region in each CPA self-consistent iteration. One can equally use an effective medium exported from a corresponding bulk calculation, which leads to the same result. Using the experience from section 4.2.1, we first analyze the BSF at the $\bar{\Gamma}$-point for an $Fe_{0.5}Co_{0.5}$/MgO interface shown in figure 4.13. Since there are no states coming from a right lead, this can be compared to the left half of the TDOS for iron leads (figure 4.7). We observe that the oscillation in the densities resulting from the interference of incoming and reflected wave decays away from the interface. This is a result of the dephasing caused by the disorder scattering. For states which are strongly affected by scattering (e.g. minority $\Delta_1^{\downarrow}$ states) it basically quenches the oscillation. The scattering and dephasing is weakest for the majority $\Delta_1^{\uparrow}$ states as shown in section 4.1.

By comparing figure 4.13 to the TDOS for iron leads an important difference becomes immediately apparent: for both spins all IRRs have a finite density in FeCo, including those which would not be available at the Fermi-energy in a VCA description. This is caused by the broadening of the bands observed in an alloy (see figure 4.1), which can lead to a finite density far away (in energy) from the actual band. An equivalent perspective is that the evanescent states are continually filled by in-scattering from other bands. For the majority spin this only leads to a small density in the three IRRs which otherwise would not be available at E_F. However, in the minority spin the finite $\Delta_1^{\downarrow}$ density obtained this way has profound consequences. First, the $\Delta_1^{\downarrow}$ density is relatively large, because the $\Delta_1^{\downarrow}$ band shows an extremely large broadening extending across E_F. More importantly, since the complex Δ_1 band in MgO has the smallest decay rate (section 4.2.1), the minority density extending into the MgO is dominated by the scattering-induced $\Delta_1^{\downarrow}$ contribution after three layers of MgO. This means that, because the FeCo alloy is not fully Δ_1 half-metallic, we have a dominating contribution of Δ_1 states not only in the majority but also in the minority spin. Since the combination of symmetry filtering and

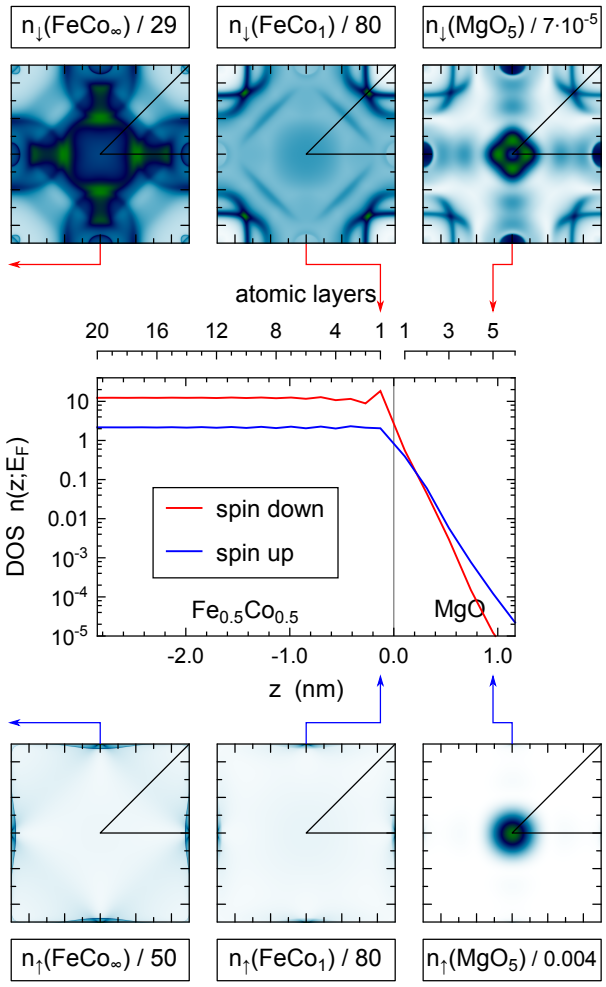

Figure 4.14: Layer-resolved DOS at the Fermi-energy for the $Fe_{0.5}Co_{0.5}$/MgO interface (middle) and $\vec{k}_{\parallel}$-resolved density (Bloch spectral density) for bulk, the FeCo layer at the interface, and in the fifth MgO layer for minority (top) and majority (bottom) spin.

Δ_1 half-metallicity is the key effect for obtaining the large TMR for iron leads, we anticipate that these minority $\Delta_1^{\downarrow}$ contributions reduce the TMR for FeCo leads. The density in figure 4.13 is calculated for a Co concentration of 50%; however, the broadening of the minority $\Delta_1^{\downarrow}$ band occurs already for relatively small Co concentrations and persists almost to pure cobalt (figure 4.3). Thus, the effect observed above is important in a large range of concentrations.

Next, we consider the density at E_F in the full two-dimensional Brillouin zone. Figure 4.14 shows the layer-resolved DOS for the $Fe_{0.5}Co_{0.5}$/MgO interface and the $\vec{k}_{\parallel}$-resolved density (BSF) in selected layers. The bulk majority BSF in FeCo is much simpler than the one for iron (figure 4.10), since the flat d-bands are below the Fermi energy. The minority BSF shows a strong broadening as expected from the BSF shown in figure 4.1. For both spins, the entire Brillouin zone is covered with at least a little density. At the interface, the majority BSF is only slightly depleted. As for iron, the minority BSF at the interface is very different from the bulk one. The bulk states are depleted and instead it shows two IRSs, which overlap on the $\bar{\Sigma}$ line (compare figure 4.11). For iron these IRSs lie in a gap of the bulk states, but for FeCo they overlap with the scattering-induced density. The IRSs show a strong broadening, in particular compared to the very sharp peak for pure iron (figure 4.10), as a result of the disorder and the coupling to bulk states. The effect of the IRSs is still visible in the outbound BSF for the minority spin

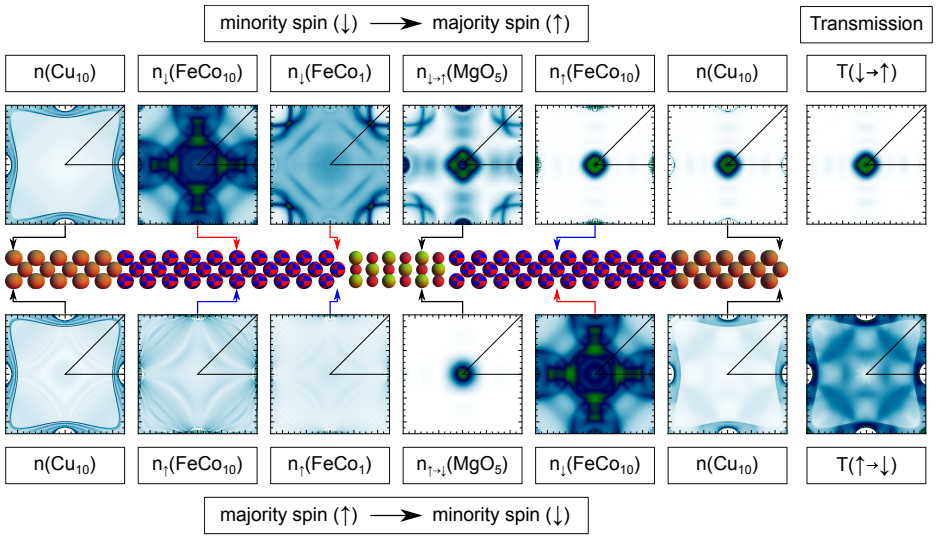

Figure 4.15: $\vec{k}_{\parallel}$-resolved tunneling density of states at E_F in a $Cu/Fe_{0.5}Co_{0.5}/MgO/Fe_{0.5}Co_{0.5}/Cu$ junction with anti-parallel alignment of the magnetizations shown for selected layers. The spin labels are relative to the local magnetization. The last column shows the transmission in the respective channel.

inside the MgO. However, the dominating contribution is located in the center of the Brillouin zone close to the $\bar{\Gamma}$-point. A part of this contribution is a result of electrons which are scattered into Δ_1-like states as explained above. Additionally, it contains contributions of states which become available at E_F via band filling (compare figures 4.12 and A.1). Both tunnel via the Δ_1-like complex band with the low decay rate in MgO. In the majority BSF inside the MgO we find a peak around $\bar{\Gamma}$, which closely resembles the peak in the majority transmission for iron (figure 4.9) and has the same origin, i.e. Δ_1-like states decaying via the complex Δ_1-like band of MgO.

The next step is to investigate a full MTJ with FeCo leads. Unfortunately, it is not possible at present to calculate transport properties when using CPA alloys for the semi-infinite leads. While obtaining an (equilibrium) effective medium for the leads is straightforward (see above), the non-equilibrium lead self-energies and vertex corrections for this case have not been derived. Thus, one has to resort to introducing a third material, which is ordered and can be used for the leads. There are several obvious choices including pure iron or cobalt or a VCA alloy with the same composition. Here, we use a different option: the leads are modeled using copper (Cu) in the bcc structure of iron. The reason for this choice is that we need a finite width of the ferromagnetic regions for spin-transfer torque calculations, which are discussed later in this work. This rules out the more obvious choices. To avoid unnecessary influence of the leads a free-electron-like metal suggests itself. The details of the metal are of no importance and the bcc structure is chosen for convenience [58]. The Cu/FeCo interfaces lead to additional effects, which are discussed bellow. A typical junction investigated in this work consists of a six-monolayer MgO barrier with 20-monolayer FeCo slabs (with the same composition) and semi-infinite (bcc) Cu leads on either side. 10 monolayers of each Cu lead are included in the middle region for the self-consistent calculation (see figure 4.15).

We start right away by discussing the TDOS in a $Cu/Fe_{0.5}Co_{0.5}/MgO/Fe_{0.5}Co_{0.5}/Cu$ MTJ for AP alignment. Note that this requires the NEGF-CPA-BSF developed in this work. The $\vec{k}_{\parallel}$-resolved TDOS at E_F in various layers is shown in figure 4.15. Just as in its equilibrium fcc structure, copper in bcc structure has a single-sheeted Fermi-surface. This results in the simple TDOS shown in figure 4.15. The hole around $\bar{X}$ originates from a corresponding hole in the Fermi-surface around the N-point on the face of the bcc Brillouin zone. The lateral faces of the Fermi-surface are folded back into the simple cubic transport cell leading to the double

coverage along the edges of the two-dimensional Brillouin zone. The TDOS shows some weak oscillations originating from the boundary condition at the Cu/FeCo interface. Since the copper is non-magnetic, both spins are very similar; the small differences result from the adjacent FeCo.

In the FeCo slab the additional interface leads to quantum-well states, since it is now enclosed by a different material on both sides. In the majority spin these lead to smooth oscillations in most regions of the Brillouin zone, since the quantum-well states are broadened by coupling to the states in copper. However, in the $\vec{k}_\parallel$-region where the copper TDOS shows a hole, the quantum-well states are sharp, since they cannot couple to (bulk) states on either side of the FeCo slab. In the minority spin the quantum-well states are strongly broadened by the disorder scattering. Apart from some small variations and the region around $\bar{X}$ for the majority spin, the TDOS at the FeCo/MgO interface is very similar to the BSF observed for semi-infinite FeCo in figure 4.14. Thus, the same effects as discussed above for that case apply. In particular, inside the MgO we obtain a TDOS coming from the left lead, which is very similar to the equilibrium BSF in MgO in figure 4.14. Here, these states couple into the right lead.

In both spin channels the dominant contributions tunnel via the Δ_1-like complex band in the vicinity of $\bar{\Gamma}$. The electrons tunneling from majority to minority spin are quickly redistributed across the states at E_F by the strong disorder scattering in the right FeCo slab. This way, the Δ_1-like states can contribute to transport rather than just decay as observed in pure iron. The minority TDOS in the right FeCo slab resembles the bulk BSF. Accordingly, we obtain a rather smooth outbound TDOS in the right Cu lead, which no longer shows the origin of the tunneling states. In the majority spin the disorder scattering is weak and the peak around $\bar{\Gamma}$ is clearly visible in the outbound TDOS. The sharp quantum-well states at $\bar{X}$ in the FeCo majority spin cannot couple to states in the Cu leads and thus contribute to the transport only indirectly via the weak in- and out-scattering. The TDOS related to the minority IRSs, which is still visible in the fifth MgO layer, is further reduced in the last MgO layer and no longer visible in the first FeCo layer (not shown), thus its contribution to transport is small.

Keeping in mind the difference in normalization (compare eqs. (2.19) and (2.22)), the outbound TDOS in the last copper layer agrees well with the transmission through the junction, which is also shown in figure 4.15. Thus, the ($\vec{k}_\parallel$-resolved) TDOS provides a powerful tool to investigate the effects that determine the transmission, even in the presence of disorder scattering. Note that, in the sense of section 2.4, the transmission is given in terms of the $\vec{k}_\parallel$-states of the right lead. This illustrates that in this case the $\vec{k}_\parallel$-resolved transmission shows the contribution at that $\vec{k}_\parallel$-point where the electron arrives in the right lead.

To summarize, we observe that the disorder scattering leads to additional contributions of Δ_1-like states tunneling from the FeCo minority spin, in particular for AP alignment. Similarly, incoming Δ_1-like states are redistributed in the FeCo minority spin and can also contribute to transport. We have discussed the two channels for AP alignment, the two channels for P alignment can be explained analogously from the same effects (see also figure 4.21).

From the discussion above, it seems that the copper leads have only little impact on the actual tunneling, since the states arriving at the barrier are similar as for semi-infinite FeCo leads. Thus, the qualitative results, which are determined by the ferromagnetic material and the barrier, are insensitive to the leads. However, the quantum-well states lead to a more or less pronounced oscillatory dependence of many quantitative results on various parameters, in particular the thickness of the ferromagnetic slabs. These oscillations are strongest and most weakly damped by disorder scattering in the majority spin. The assumed perfect Cu/FeCo interfaces are difficult to achieve in experiments and interface roughness would interfere with the quantum-well states. Also, the thickness dependence would restrict the significance of many results to a fixed slab thickness. Therefore, we reduce the effect of the quantum-well states by introducing a rough interface between the FeCo slab and the Cu lead, which is modeled by averaging over several slap thicknesses. We repeat each calculation varying the slab size on each side independently between 19 and 21 layers, which results in nine combinations. The results are averaged with a weight of 25%, 50%, 25% for 19, 20, 21 layers. This reduces the oscillations quite effectively, since the dominating oscillations (for iron) have a period of about two layers [56]. We treat the junctions with different thicknesses as conducting independently in parallel,

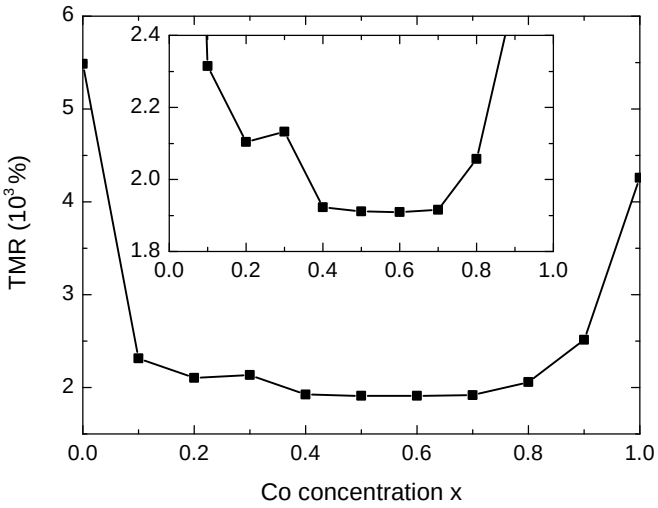

Figure 4.16: Tunnel magnetoresistance in junctions with $Fe_{1-x}Co_x$ ferromagnetic layers as a function of the Co concentration for zero bias voltage; the inset shows a detailed view at intermediate concentrations. Modified from [A5].

thus the conductances, currents, etc. are averaged and the derived quantities like the TMR are obtained from the averaged result. The rough interface might also be considered as a transition to an amorphous region.

4.4 Material dependence of the TMR

In the following sections we systematically investigate various transport phenomena in MTJs with disordered FeCo leads. We focus mainly on TMR and STT, but the discussion also includes e.g. spin currents, which are important in many spintronic applications. In the present section we analyze the dependence of the TMR at zero bias voltage on the Co concentration. To this end, we calculate the TMR in the full concentration range from pure iron to pure cobalt. The calculations include the thickness averaging for the finite-width FeCo slabs, which are contacted by copper leads, as described in the previous section. The results are shown in figure 4.16.

Because of the additional copper leads, the TMR of 5490% for pure iron is larger than the one reported for semi-infinite iron lead in section 4.2. The values obtained individually for the different thicknesses show a considerable spread with a standard deviation of 15%, which demonstrates the necessity of the averaging. For pure cobalt the spread is even larger. However, some of this variance can be attributed to the definition of the (optimistic) TMR ratio, which is very sensitive to small changes in R_{ap}.

The TMR shows a steep drop from the pure materials to the first finite concentrations included in the calculations resulting in a value of about 2000%. From this dependence and the discussion in section 4.3 we assume that this is related to effects of disorder scattering. To confirm this idea, we investigate the conductances entering in the TMR (eq. (4.3)). These are shown in figure 4.17. For P alignment the conductance varies only moderately by less than 10% showing a slight decrease with the Co concentration. In contrast, the AP conductance doubles from 0% to 10% and from 100% to 80% cobalt. This increase causes the observed decrease in the TMR. Figure 4.17 also shows the contribution described by the vertex corrections, which can be interpreted as the diffusive part of the conductance (see eq. (2.26)). In the majority spin only a small fraction of the conductance is diffusive, showing the weak effect of disorder scattering on the $\Delta_1^\uparrow$ states. The minority conductance is almost completely diffusive for finite concentrations. This is expected, since in both contributing channels ($\uparrow\downarrow$ and $\downarrow\uparrow$) the electrons need to traverse a minority FeCo region, which exhibits strong scattering even for small concentrations. The $\downarrow\downarrow$ channel for P alignment is also completely diffusive, but gives only a small contribution ($1 - 2\%$) to the P

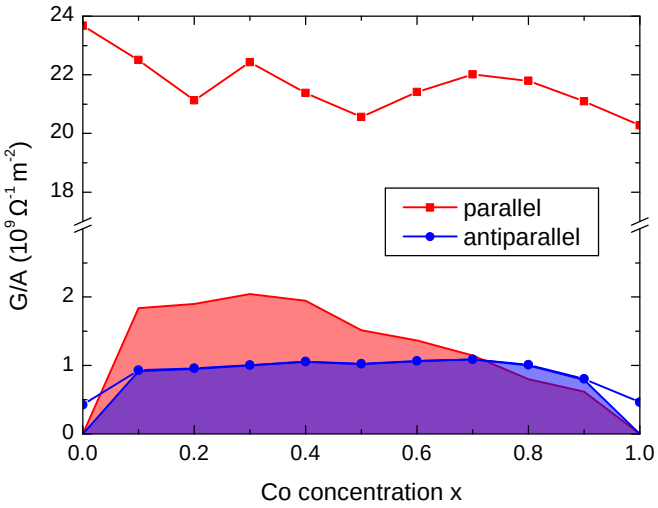

Figure 4.17: Concentration dependence of the conductance for parallel and anti-parallel alignment at zero bias voltage. The shaded areas indicate the diffusive part of the conductance described by the vertex corrections. Note the break in the vertical axis. [A5]

conductance. Only for pure iron it has a relevant contribution of about 10%, which is a result of the Δ_5-like IRS.

In section 4.3 we found that for 50% Co an important contribution to the transport for AP alignment is created by electrons which are scattered from or into minority $\Delta_1^\downarrow$-like states and tunnel in the center of the two-dimensional Brillouin zone. To analyze for which concentrations this contribution is important we calculate the relevant density in FeCo alloys, i.e. the density at the Fermi-energy of such states which are projected onto $\bar{\Gamma}$ in the transport geometry [14]. This is the density at $\vec{k}_\parallel = 0$ integrated over k_z[11]; it is shown in figure 4.18. In the majority spin the $\Delta_2'^\uparrow$ and $\Delta_5^\uparrow$ bands shift below the Fermi-energy at small Co concentrations and their contributions decrease rapidly leaving only $\Delta_1^\uparrow$ states. For the minority spin the contributions from $\Delta_2'^\downarrow$ and $\Delta_5^\downarrow$ states decrease with the concentration while the $\Delta_2^\downarrow$ contribution increases. However, the important part is the $\Delta_1^\downarrow$ contribution; we find that it increases slowly at small concentrations, then shows a broad peak at high concentrations with a maximum at 75% Co, and afterwards decreases quickly towards pure cobalt[12]. From the $\Delta_1^\downarrow$ density we can infer that the effect described in section 4.3 has a significant influence on the AP conductance for concentrations $\gtrsim 40\%$. In the same range we also expect an increase of contributions via band filling (compare section 4.2.4 and appendix A.4). Thus, at small concentrations we anticipate additional contributions to explain the observed AP conductance.

To identify potential additional contributions for small Co concentrations we analyze the TDOS inside the MgO barrier shown in figure 4.19. As shown in section 4.3 this provides a more reliable view on the actual tunneling process than the transmission, which is influenced by disorder scattering in the right lead. The TDOS provides a clear picture of additional contributions: we find an additional peak along the $\bar{\Delta}$ line, which is due to the Δ_5-like IRS that has already been observed for iron in section 4.2.2. Note that in a VCA picture this would actually be shifted below E_F by the band filling for 20% Co (see appendix A.4), but is still visible because of a large disorder broadening. The two IRS observed along the $\bar{\Sigma}$ line for 50% Co (figure 4.14) are faintly visible for $\geq 20\%$ Co. These also cause the outer peaks close to $\bar{X}$ for $\geq 20\%$ Co. Further, there are peaks close to $\bar{X}$, which are related to quantum-well states (see section 4.3).

[11] Note that the projected density is different from the corresponding line in figure 4.3, which includes only states at $k_z = 0$.

[12] Note that the minority $\Delta_1^\downarrow$ contribution does not decrease completely to zero because of some necessary artificial broadening and the proximity to the actual $\Delta_1^\downarrow$ band in Co.

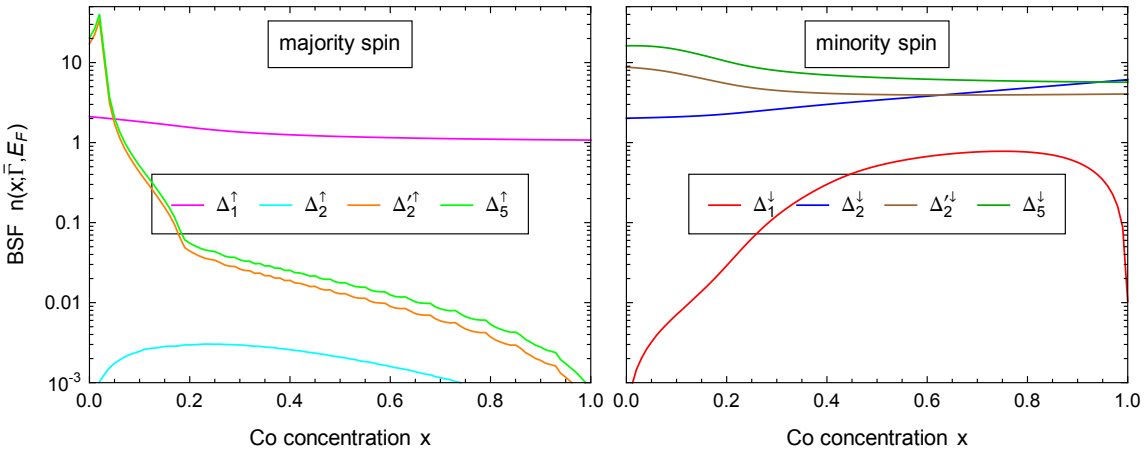

Figure 4.18: Projected density at the center of the two-dimensional Brillouin zone $\bar{\Gamma}$ of $Fe_{1-x}Co_x$ as a function of the cobalt concentration at the respective Fermi-energy; contributions are resolved by the IRRs.

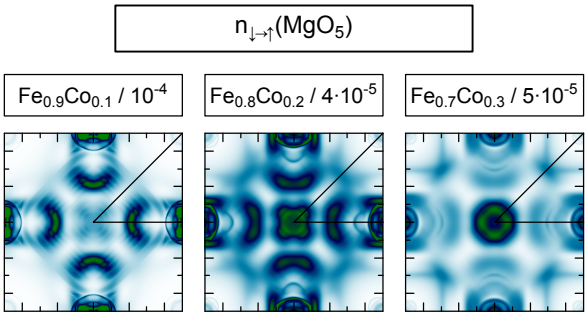

Figure 4.19: Tunneling density of states in the fifth layer of the MgO barrier coming from the minority spin in the left lead of a MTJ with 20 monolayer FeCo slabs in anti-parallel alignment; shown for three different compositions.

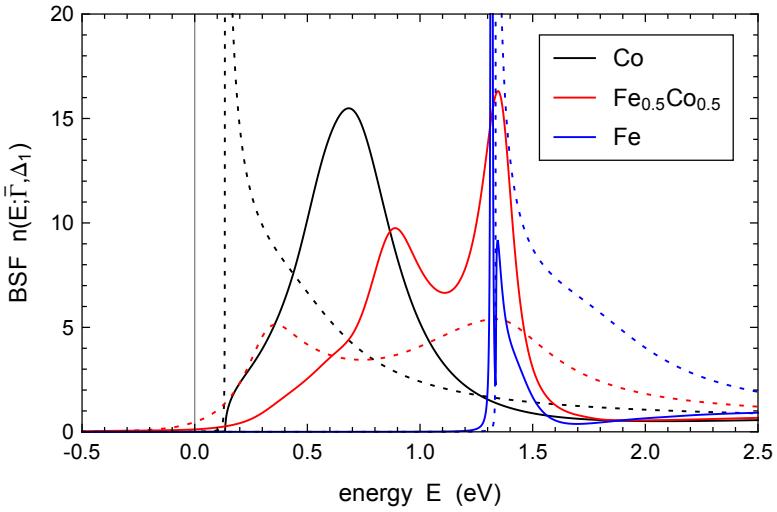

Figure 4.20: Bloch spectral density at $\bar{\Gamma}$ in an energy range above the Fermi-energy at an Fe/MgO, $Fe_{0.5}Co_{0.5}$/MgO, and Co/MgO interface; only the Δ_1 contribution is shown; the dotted line shows the corrsponding bulk density for comparison.

Although these cannot contribute directly to the transport they could make a small contribution via in- and out-scattering. With increasing Co concentration the additional peaks become less important relative to the peak around $\bar{\Gamma}$ and become negligible for $\gtrsim 30\%$. As explained in section 4.3 this peak results from a combination of electrons which are scattered into this $\vec{k}_\parallel$ region and states that become available via band filling (which are of course also influenced by the disorder). It is a curious coincidence that the sum of these contributions leads to a basically concentration-independent AP conductance for $10\% \leq x \leq 50\%$. In particular, the decrease in G_{ap} observed for iron leads at energies above the IRS (figure 4.12) and in the VCA result for $x > 8\%$ (figure A.1) is compensated by effects of disorder scattering.

In section 4.2.2 we observed another IRS at higher energies in the minority spin of iron; it has Δ_1 symmetry at $\bar{\Gamma}$ and leads to a very large contribution in $T_{\downarrow\downarrow}$ and T_{ap} (figure 4.12). One might expect that via band filling this IRS would shift close to or even cross the Fermi-energy with increasing Co concentration, which should have a large effect on the TMR. To explain why this is not the case, figure 4.20 shows the interfacial minority $\Delta_1^\downarrow$ BSF at $\bar{\Gamma}$ for $Fe_{0.5}Co_{0.5}$ and the pure materials. The figure also includes the corresponding bulk BSF. For the pure materials the latter shows the expected $1/\sqrt{E}$ dependence at the band onset, while for the alloy it shows the broadened two-peak structure observed in figure 4.2. For iron the BSF at the interface shows a sharp peak from the IRS directly below the bulk-like states. The concentration dependence of the Δ_1-like IRS is very different from a simple band filling. Similar to the bulk $\Delta_1^\downarrow$ states, the $\Delta_1^\downarrow$ IRS peak of FeCo alloys splits in an iron- and a cobalt-like peak at finite concentrations. While the iron-like peak retains its position, the cobalt-like peak shifts towards the Fermi-energy. Both peaks overlap with the bulk states and are strongly broadened by this coupling and the disorder. For pure cobalt the IRS is still far above E_F (at 0.68 eV) and inside the bulk-like states, which explains why it is not observed in the TMR at zero bias. The described trends have been verified for more Co concentrations and also for the interfacial BSF along symmetry $\vec{k}_\parallel$-lines (not shown). Interestingly, for a plain bcc Co surface the IRS is predicted below E_F [19], which shows that the MgO layer has a strong influence on the IRS.

Finally, we discuss the ($\vec{k}_\parallel$-resolved) transmission for the case of the pure lead materials in more detail. These are shown in figure 4.21 including the previously discussed case of $Fe_{0.5}Co_{0.5}$ for comparison. In the $\uparrow\uparrow$ channel for P alignment we find the pronounced peak at $\bar{\Gamma}$ for all concentrations, which has been observed and explained in section 4.2.1. The other channels for the pure materials show a strong influence of the quantum-well states, which lead to additional structure in the $\vec{k}_\parallel$-resolved transmission. For $T_{\downarrow\downarrow}$ the structure is particularly sharp, since the

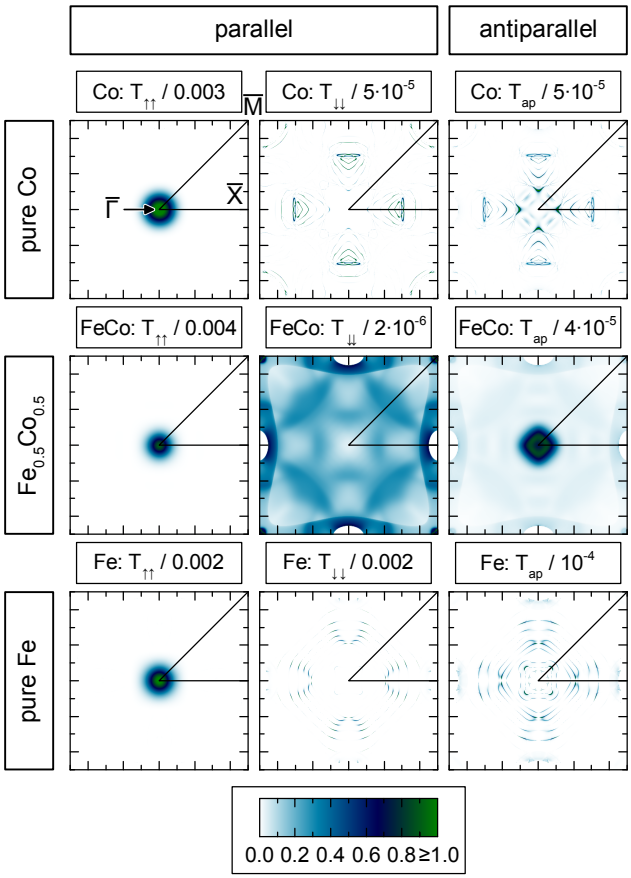

Figure 4.21: Transmission through a MTJ containing 20-monolayer Fe, $Fe_{0.5}Co_{0.5}$, and Co slabs as ferromagnetic layers for parallel ($T_{\downarrow\downarrow}$ and $T_{\uparrow\uparrow}$) and anti-parallel ($T_{ap} = T_{\downarrow\uparrow} + T_{\uparrow\downarrow}$) alignment at the respective Fermi-energy. [A5]

quantum-well states are aligned on both sides of the barrier. For iron we find the structure observed for semi-infinite leads (figure 4.9), including the peaks from the IRS, but superimposed by the structure from the quantum-well states. For cobalt a relatively weak effect of an IRS is visible close to $\bar{M}$. Note that the indicated plus-sign like shape of the contributions for both pure cases (and also some other figures before) is a result of the complex band structure of MgO [63].

4.4.1 Experimental results

The interest in FeCo alloys as ferromagnetic leads has originally been inspired by calculations predicting even larger TMR ratios for ordered equimolar Fe_1Co_1 alloys or pure Co than for pure Fe [152]. In these calculations the ordered alloy was described by a B2 structure[13]. Although growth of this ordered structure is occasionally observed [36], it is unclear whether it plays a role in MTJs. From the previous sections it is clear that neglecting the effects of disorder is not a valid approximation for this system. Thus, the applicability of these results is questionable and, either way, they cannot be extended to arbitrary concentrations.

The concentration dependence of the TMR has been subject to systematic experimental investigations [84, 19]. Despite different growth methods (molecular beam epitaxy [19] and radio frequency magnetron sputtering [84]) both investigations obtain similar qualitative trends: Starting from pure iron the TMR increases with the Co concentration and shows a maximum at 25% Co, which has ca. 150% of the value for pure Fe. For higher Co concentrations the TMR drops to about half the Fe value at 75% Co. This trend is observed at room temperature as well as at low temperature. The largest observed values are 530% [19] and 1010% [84] at low temperature. This experimental concentration dependence is quite different from our result. In particular, the steep increases towards pure lead materials are not observed. This is not surprising given the discrepancy between calculations and experiments for pure Fe leads, which was already discussed in section 4.2.3. The decrease of the TMR for large Co concentrations observed in the experiments may be explained by the mechanisms found in section 4.3.

In the initiating publication [152], the predicted increase in TMR with the Co concentration was explained by the disappearance of majority $\Delta_5^\uparrow$ (and $\Delta_2'^\uparrow$) contributions at $\bar{\Gamma}$ leading to an infinite TMR for this $\vec{k}_\parallel$-point (compare section 4.2.1). This argument is not quite conclusive, since the contributions from these bands at $\bar{\Gamma}$ are negligible either way. However, it seems plausible that shifting the majority d-bands below the Fermi-energy (the Δ_1-band is regarded 's-like') should reduce the overlap of the states contributing to the AP conductance, since these are then purely s-like in the majority and purely d-like in the minority spin. The d-bands are completely below E_f for about 20% Co [A3]. In section 4.2.4 we found a decrease in the AP transmission for energies above the contributions from the Δ_5-like IRS. However, this decrease is related to the iron minority states in that energy range, which also cause a strong decrease in $T_{\downarrow\downarrow}$. In a simple VCA picture (and ignoring the IRS) this decrease and the subsequent increase in T_{ap} result in a concentration dependence of the TMR, which is qualitatively similar to the experimental one [130] (compare appendix A.4). This provides an alternative explanation of the experimentally observed increase. In our CPA calculations the contributions from the IRS, which is strongly broadened by disorder scattering, actually lead to a constant T_{ap} in this concentration range. Because of the rather thin barrier and the absence of interface roughness, the effect of the IRS may be overestimated in our calculations compared to the experiments (see also section 4.2.3), which could explain the discrepancy (apart from the limits of pure lead materials).

It is interesting that the concentration dependence of the TMR follows qualitatively the one of the magnetization [A3], i.e. the Slater-Pauling curve, which shows a maximum of $2.37\,\mu_B$ for 17% Co (refined from [A3]). This maximum occurs, when the majority d-bands are completely filled and the higher minority d-bands are still empty. This explanation is related to the one above (apart from IRS), but for the TMR the coupling of the different states to the Δ_1-like complex band in MgO is more important than their density.

The calculated lattice constant also shows a similar concentration dependence [A3]. The increase at small Co concentrations is overestimated compared to experiments [36] and has little effect on the lattice mismatch. On the other hand, the decreasing lattice constant at large Co concentrations may impair the MgO and interface quality. Furthermore, the latter may be influenced by a change in the interface chemistry. Thus, one may expect an effect of a change in growth quality in addition to the electronic effects discussed above.

The band alignment between the ferromagnets and the MgO barrier depends on the alloy

[13] The Caesium chloride or B2 structure consists of two interpenetrating simple cubic lattices with cubic coordination.

composition. In our calculations this leads to a small, about linear shift of the Fermi-energy toward the valence bands in MgO with increasing Co concentration, which is 0.22 eV for Co and has little influence on the transport. However, in experiments this alignment may be influenced by details of the interface and the barrier.

The concentration dependence of the IRSs has also been studied experimentally [19]. This investigation uses spin- and symmetry-resolved photoemission spectroscopy to investigate the electronic structure of an FeCo surface. They identify a minority IRS which crosses the Fermi-energy from above at about 30% Co and indicates $\Delta_1^\downarrow$ symmetry [19, 4]. This would mean that the cobalt-like peak of the $\Delta_1^\downarrow$-like IRS shifts downwards in energy with the Co concentration much faster than observed in our calculations and crosses the Fermi-energy at small concentrations. Such a substantial discrepancy might be attributed to unanticipated surface conditions (e.g. oxidation). Conversely, if the experimental symmetry assignment is incorrect, the observed IRS might be identified with the $\Delta_5^\downarrow$-like IRS observed in the calculations (but not observed in these experiments). This would reduce the discrepancy, although it would mean that the $\Delta_5^\downarrow$-like IRS is located at a higher energy in the experiments.

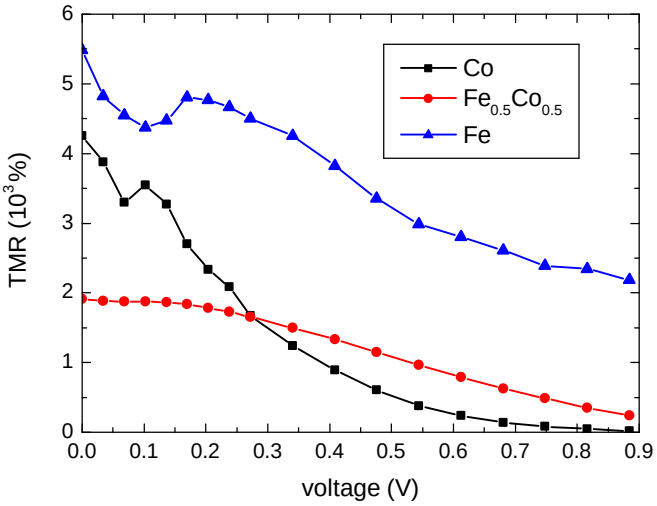

Figure 4.22: Bias-voltage dependence of the TMR in MTJs with Fe, $Fe_{0.5}Co_{0.5}$, and Co ferromagnetic slabs. [A5]

4.5 Bias-voltage dependence of the TMR

In this section we study the TMR at finite bias voltage for different compositions in the ferromagnetic layers. The applied bias voltage V corresponds to a difference in the chemical potentials (or quasi Fermi-levels) of electrons in both leads $\mu_L - \mu_R = -e\,V$, where $e = |e|$ is the (positive) elementary charge. The sign of the bias voltage is defined in such a way that for positive voltages the electrons tunnel from the right to the left lead (which means that the conventional current direction is left to right). In the calculations, the bias voltage is described by a rigid-band shift [61]: the left lead and the metallic layers left of the barrier are shifted by $-e\,V/2$ and those on the right by $+e\,V/2$; in the barrier a linear drop between these values is assumed. The shift is applied by shifting the self-consistent potentials accordingly. This form of the potential corresponds to an ideal capacitor. It has been shown that this assumed potential is very similar to a self-consistent result [113]. The calculations are performed for zero temperature, thus the Fermi-functions of the leads are step functions and the energy integration in eq. (2.21) can be restricted to $[\mu_L, \mu_R]$. The thickness averaging for the ferromagnetic slabs (see section 4.3) is included in these calculations. Since the averaged junctions are symmetric, the TMR is an even function of the bias and only positive voltages are shown.

Figure 4.22 shows the bias-voltage dependence for $Fe_{0.5}Co_{0.5}$ alloys and both pure materials. The TMR at zero bias shows the reduction from pure lead materials to FeCo alloys explained in section 4.4. The junction with Fe leads shows a pronounced S-shape structure at small bias and a moderate decrease at larger bias to 40% of its zero-bias value at 0.88 V [14]. For the FeCo alloy we obtain a very smooth bias dependence. It starts from 1910% at zero bias, stays almost constant at small bias, and then decreases about linearly to 237% at 0.88 V. For Co leads the bias dependence shows a narrow S-shape around 0.1 V followed by a steep decrease to only 18% TMR at 0.88 V. Because of the much faster decay, the TMR for Co even drops below the FeCo value for voltages > 0.28 V. Thus, the bias dependence is very different for the three lead materials and needs to be discussed separately for each case.

To understand the bias-voltage dependence of the TMR we analyze the bias-voltage dependence of the corresponding conductances $G = I_{tot}/V$ shown in figure 4.23. We find that the P conductance is basically independent of the bias voltage and the Co concentration. The TMR is controlled by the AP conductance, which shows a very different bias dependence for the three materials ranging from a moderate increase for Fe to an exponential increase for Co. The two

[14] The bias voltage sampling, as most other energy meshes, is set in Rydberg units leading to odd numbers in SI units.

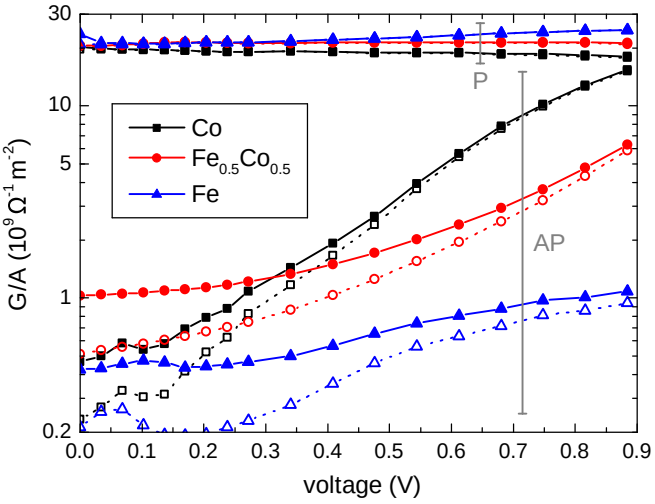

Figure 4.23: Bias-voltage dependence of the conductance in MTJs containing Fe, $Fe_{0.5}Co_{0.5}$, and Co leads for parallel and anti-parallel alignment of the magnetizations; the dashed lines with open symbols show the contribution of the dominating channel, which is $G_{\uparrow\uparrow}$ for P and $G_{\downarrow\uparrow}$ for AP conductance. [A5]

channels contributing for each alignment (eq. (4.2)) can be investigated separately. As already observed at zero bias, the P conductance is dominated by the $G_{\uparrow\uparrow}$ contribution; this remains valid for all concentrations and considered bias voltages. This also means that the tunnel current for P alignment is strongly spin-polarized. Only at zero bias for the pure materials $G_{\downarrow\downarrow}$ has a notable contribution, which disappears at the first sampling point (34 mV). For the AP conductance both channels are equal at zero bias; however, their bias dependence is very different and at large bias the AP conductance is dominated by $G_{\downarrow\uparrow}$, i.e. electrons tunneling from the majority spin in the right lead to the minority spin in the left.

The different bias-voltage dependences can be understood qualitatively using results from the previous sections, in particular section 4.2.4. Since additional structure from quantum-well states impedes a direct interpretation of the energy- and $\vec{k}_\parallel$-resolved conductances, we mostly confine the discussion to this qualitative level. Note however that the energy integration at finite bias voltage leads to an additional averaging and further reduces the effects of quantum-well states for integrated properties. The MgO barrier causes a strong decoupling of both leads. Therefore, we can assume that the states in both leads, including the IRSs, are only unalteredly shifted relative to each other in energy by the bias voltage [113]. Additionally, since the complex bands in MgO show only a weak energy dependence in the relevant energy range inside the band gap (figure 4.8), the modification of the barrier by the bias voltage can be ignored in the first approximation. These simplifications can be justified by the transmission functions calculated at finite bias for iron leads discussed in [113]. As an additional simplification for the AP conductance we can ignore the weak energy dependence of the majority Δ_1 band and assume that the bias dependence is determined solely by shifting the minority states in the other lead. The last approximation is particularly convenient, since it allows to estimate the conductances for the AP channels at finite bias from the energy-dependent AP conductance at zero bias; this estimate is given by the average over the interval $[E_F - V, E_F]$ ($[E_F, E_F + V]$) for electrons tunneling from (into) the minority states.

As an illustration we explain the observed S-shape for iron at low bias voltage in detail. It is a result of the minority $\Delta_5^\downarrow$-like IRS, which influences the three conduction channels in different ways. The drop in the TMR from zero bias to the first bias point is caused by the reduction in $G_{\downarrow\downarrow}$, which in turn results from misaligning the IRSs in both leads. Since the IRS has a flat dispersion, small shifts in energy diminish the overlap in $\vec{k}_\parallel$-space. This is enhanced

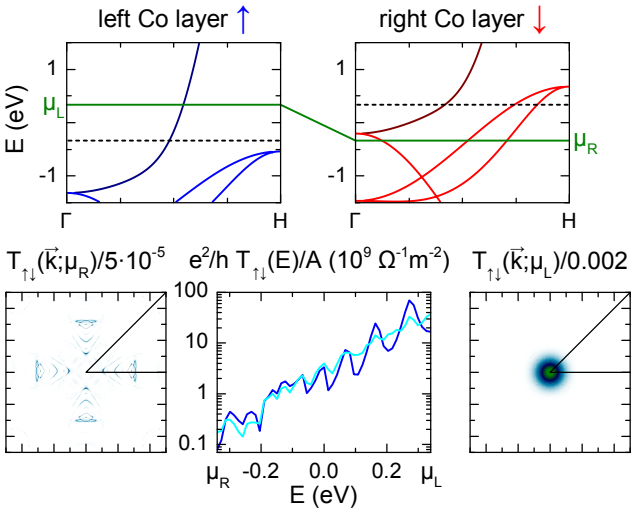

Figure 4.24: Transmission in a MTJ with Co leads for AP alignment at a negative bias voltage $(\mu_L - \mu_R)/(-e) = -0.68$ V in the ↑↓ channel; electrons are tunneling from left to right.
Top: Alignment of the involved bulk bands (at $\bar{\Gamma}$) in both leads, the Δ_1 bands are emphasized, the green line shows the chemical potential on each side, which also matches with the bulk Fermi-energy. Bottom, center: Energy-resolved transmission for 20 monolayer ferromagnetic slabs (blue) and thichness-averaged (cyan). Bottom, left and right: $\vec{k}_\parallel$-resolved transmission at μ_R and μ_L for 20 monolayers (modified from [A5])

and supplemented by quantum-well effects, which lead to an additional localization in $\vec{k}_\parallel$-space (see figure 4.21). Consequently, the large enhancement at zero bias for $G_{\downarrow\downarrow}$ only appears for symmetric junctions entering in the thickness averaging. An analogous effect does not occur for $G_{\uparrow\uparrow}$, since the position of the Δ_1-like peak in the $\vec{k}_\parallel$-resolved transmission is fixed by the barrier, or the AP channels, which contain no alignment of similar states. The subsequent broad minimum in the TMR for Fe extending from 0.034 V to 0.17 V results from a maximum in G_{ap}, which is actually the sum of two peaks. One peak appears in $G_{\downarrow\uparrow}$ at ca. 0.06 V resulting from electrons tunneling into the IRS in the left lead and corresponds to the peak above the Fermi-energy observed in G_{ap} in figure 4.12. The second peak occurs in $G_{\uparrow\downarrow}$ at ca. 0.12 V and results from electrons tunneling from the IRS in the right lead (peak below E_F in figure 4.12). A similar explanation might hold for cobalt, which shows a weak influence of an IRS observed close to $\bar{M}$.

After the IRS related peak, G_{ap} for iron shows a moderate linear increase, which leads to the observed reduction in the TMR. This results from an increase in $G_{\downarrow\uparrow}$ with increasing bias voltage (while $G_{\uparrow\downarrow}$ decreases) in agreement with the estimate from the energy-dependent conductance in figure 4.12. Thus, for iron we can qualitatively understand all important features of the bias dependence from the explanations in previous sections. Note that we do not see any influence of the minority $\Delta_1^\downarrow$ IRS or bulk band, which cause a large increase in figure 4.12, since they lie outside the considered bias range.

Next, we discuss the bias-voltage dependence for cobalt leads. From the previous sections it is evident that the steep increase in the ↓↑ channel is related to the proximity of the minority $\Delta_1^\downarrow$ band to the Fermi-energy. For cobalt it is only 0.134 eV above E_F, whereas for iron it is far away (1.36 eV). The effect is illustrated in figure 4.24, which shows the situation at a large bias voltage. For convenience, we consider the ↑↓ channel for a negative bias voltage, i.e. the electrons are tunneling from left to right. By symmetry, this is equivalent to ↓↑ at positive bias. Via the rigid-band shift, the bands in both leads are shifted relative to each other, such that the difference between the chemical potentials in both leads yields $-eV$, but locally the chemical potential is in the position of the equilibrium Fermi-energy. Only occupied states in the left lead

(i.e. below μ_L) and above the chemical potential in the right lead contribute to the transport; below μ_R contributions in both directions cancel. For a sufficiently large (negative) bias voltage, minority $\Delta_1^\downarrow$ states in the right lead shift into the resulting energy window $[\mu_R, \mu_L]$ from above. This means that majority $\Delta_1^\uparrow$ states from the left lead can tunnel into these states and no longer decay in the right lead; these make a large contribution to the current. In other words, the bias voltage effectively reduces the Δ_1-half-metallic gap, which was responsible for the large TMR in the first place, and causes contributions from a Δ_1-metallic region. Thus, the strong reduction of the TMR in this case is evident. This also explains the observed threshold voltage of ca. 0.14 V for the exponential increase in $G_{\downarrow\uparrow}$. To substantiate this explanation we investigate the energy-resolved transmission. We expect a significant increase starting 0.134 eV above μ_R; this can be observed in figure 4.24. The increase is about exponential after the threshold. For the junction with a fixed slab size of 20 monolayers Co we observe pronounced oscillations, which are superimposed on the increase. These are strongly suppressed in the thickness-averaged curve, which shows that they result from a quantum-well effect. Finally, figure 4.24 shows the $\vec{k}_\parallel$-resolved transmission at both endpoints of the energy window, which can be compared to figure 4.21. At the lowest energy μ_R we observe a transmission which is very similar to T_{ap} at zero bias. At the highest energy μ_L the transmission looks like a typical $\uparrow\uparrow$ transmission and shows the pronounced peak around $\bar{\Gamma}$ (without a hole in the center), which indicates (bulk) Δ_1-like contributions.

Note that the observed increase in $G_{\downarrow\uparrow}$ (figure 4.23) is still much smaller and smoother than what might be expected from figure 4.12, which shows an extremely large peak in $T_{ap}(E)$ for iron at the onset of the $\Delta_1^\downarrow$ states. The reason for this discrepancy is the different position of the $\Delta_1^\downarrow$-like IRS, which lies directly below the $\Delta_1^\downarrow$ bulk band for iron but is shifted into the bulk bands for cobalt as explained in section 4.4. This also shows the strong influence of the density at the interface (with or without IRS) on the transport, since the bulk density is similar for both materials (figure 4.20).

From the above explanation it is clear that a similar large contribution cannot occur in $G_{\downarrow\downarrow}$, since, while the minority $\Delta_1^\downarrow$ band in one lead is shifted down into the energy window, the one in the other lead is shifted upwards and always stays above the energy window. Consequently, $G_{\downarrow\downarrow}$ shows only a very small increase with the bias voltage and makes no significant contribution to G_p (figure 4.23). An analogous explanation holds for $G_{\uparrow\downarrow}$ (for positive bias), where the $\Delta_1^\downarrow$ band in the right lead always stays above the energy window. $G_{\uparrow\downarrow}$ is basically independent of the bias voltage.

The above explanations for Co can be easily extended to the $Fe_{0.5}Co_{0.5}$ alloy. In this case, because of the large disorder broadening, the minority $\Delta_1^\downarrow$ band extends even below the Fermi-energy. It contributes to G_{ap} in addition to states which become available via band filling. The sum is responsible for the small TMR (compared to the pure materials) at zero bias. This was explained in section 4.4. This contribution outweighs (for 50% Co) the small contributions from IRSs, which are moreover broadened by disorder. This explains the smooth bias dependence of the TMR at small bias voltage. For $G_{\downarrow\uparrow}$ we observe a steep but smooth increase with the bias voltage as the Co-like $\Delta_1^\downarrow$ peak in the left lead shifts into the energy window (compare figure 4.20). $G_{\uparrow\downarrow}$ slightly decreases, since the energy windows includes an increasing share of the decaying $\Delta_1^\downarrow$ tail and the less efficiently tunneling states. Nevertheless, $G_{\uparrow\downarrow}$ makes a significant contribution to G_{ap} up to high voltages. As for the pure materials G_{ap} is responsible for the decreasing TMR, whereas G_p is basically constant and strongly dominated by $G_{\uparrow\uparrow}$. $G_{\downarrow\downarrow}$ contributes less than 1% to G_p and shows a complicated bias dependence resulting from the $\Delta_1^\downarrow$ band as well as several IRS.

To conclude this section on the TMR at finite bias voltage and finite concentrations we discuss the full concentration dependence at a high bias voltage of 0.544 V. This is shown in figure 4.25; additionally figure 4.26 shows the concentration dependence of the corresponding conductances. The concentration dependence at the high bias voltage is very different from the one at zero bias and shows a smooth decrease with the Co concentration, which results from an about linear increase in $G_{\downarrow\uparrow}$. This is expected from the previous discussions and indicates an

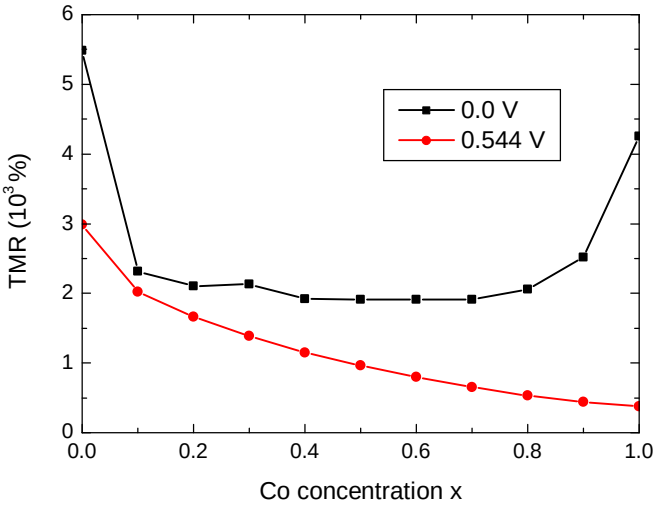

Figure 4.25: TMR in a MTJ with $Fe_{1-x}Co_x$ leads at a finite bias voltage of 0.544 V as a function of the Co concentration; the dependence at zero bias (figure 4.16) is included for comparison. [A5]

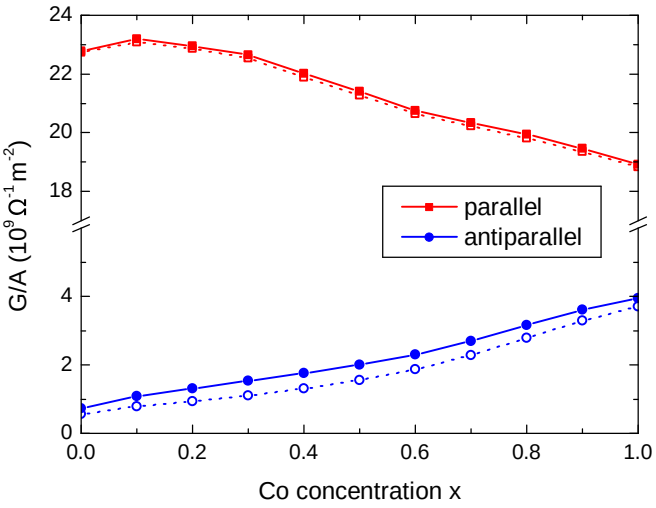

Figure 4.26: Concentration dependence of the conductance in a MTJ with $Fe_{1-x}Co_x$ leads at a finite bias voltage of 0.544 V for P and AP alignment; the dashed line (open symbols) shows the contribution of the dominating channel, which is ↑↑ for P and ↓↑ for AP alignment. Note the break in the vertical axis. [A5]

increasing contribution of electrons which tunnel via Δ_1-like states in MgO. The Co-like minority $\Delta_1^\downarrow$ peak lies inside the energy window created by the bias voltage and gains weight as the Co concentration increases (compare figure 4.3). Further, we have contributions from the states that cause the increase in $T_{ap}(E)$ for pure iron at higher energies (figure 4.12). For pure iron the latter are the main reason for the decrease in TMR with the bias voltage, while at increased Co concentrations the former dominate (figure 4.24). It is notable that G_{ap} is smooth through to the limiting cases of pure materials, unlike at zero bias, where we found a steep increase from the pure materials to small concentrations. Such a dependence is still observed at the high bias voltage in $G_{\uparrow\downarrow}(x)$, which shows the form of an inverted parabola. This behavior can be explained by generic disorder scattering, which leads to additional conduction channels. Such a contribution depends on the amount of disorder and should behave roughly like $\propto x\,(1-x)$. A similar dependence is observed in $G_{\downarrow\downarrow}$ but with additional contributions from IRSs for small concentrations and the $\Delta_1^\downarrow$ states at high concentrations. $G_{\downarrow\downarrow}$ is small and contributes less than 0.6% to G_p. On the other hand, $G_{\uparrow\downarrow}$ contributes up to 29% to G_{ap} and adds to the decrease in TMR for low Co concentrations. $G_{\uparrow\uparrow}$ shows a moderate decrease with the Co concentration to 82% of its maximal value, which can be attributed to a decrease in the $\Delta_1^\uparrow$ density with increasing energy. Noteworthy, the slight maximum in $G_{\uparrow\uparrow}$ is the result of a relatively large diffusive contribution (not shown), which decreases for higher Co concentration.

In general, it is difficult to compare calculated TMR values at finite bias voltage to experimental results, since the latter always include inelastic contributions (e.g. from electron-magnon scattering) even at low temperature. Moreover, a systematic investigation of the Co-concentration dependence at large bias has not been published. Although it is not the equilibrium structure, metastable cobalt in bcc structure has been successfully grown and deployed in tunnel junctions [148]. This investigation also shows that the TMR with Co leads decreases faster with increasing bias voltage than for Fe in agreement with our results.

We briefly comment on the symmetry relations between the spin channels at finite bias voltage. Considering a general junction containing n_L (n_R) monolayers in the left (right) ferromagnetic slab we rotate the system by 180° around the x- or y-axis. This yields a similar system at the negative bias voltage (the simultaneous rotation of the magnetizations has no effect). We obtain the relation

$$G_{\sigma\sigma'}^{n_L n_R}(+V) = G_{\sigma'\sigma}^{n_R n_L}(-V), \tag{4.5}$$

thus for a symmetric or the averaged junction we have $G_{\uparrow\downarrow}(+V) = G_{\downarrow\uparrow}(-V)$ and $G_{\uparrow\uparrow}$, $G_{\downarrow\downarrow}$, G_p, and G_{ap} are symmetric in V.

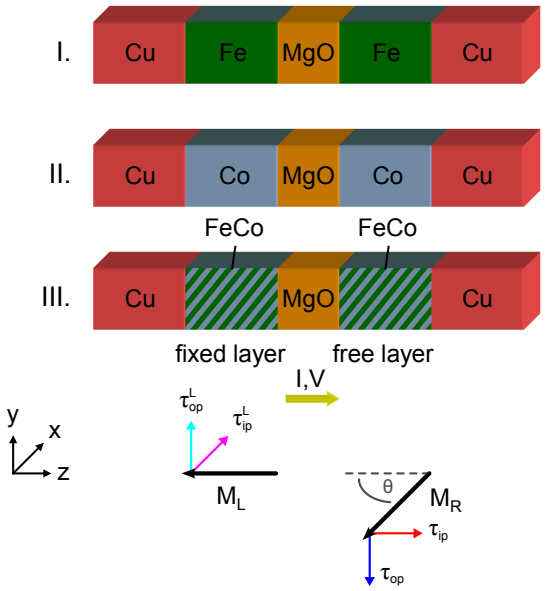

$\vec{e}_L$	$\vec{e}_R$	$\vec{e}_{op} = \vec{e}_{op}^{R} = -\vec{e}_{op}^{L}$	$\vec{e}_{ip} = \vec{e}_{ip}^{R}$	$\vec{e}_{ip}^{L}$
$-\vec{e}_z$	$-\vec{e}(\theta)$	$\frac{\vec{e}_R \times \vec{e}_L}{\lvert\vec{e}_R \times \vec{e}_L\rvert}$	$\vec{e}_R \times \vec{e}_{op}^{R}$	$\vec{e}_L \times \vec{e}_{op}^{L}$
$\begin{pmatrix} 0 \\ 0 \\ -1 \end{pmatrix}$	$-\begin{pmatrix} \sin(\theta) \\ 0 \\ \cos(\theta) \end{pmatrix}$	$\begin{pmatrix} 0 \\ -1 \\ 0 \end{pmatrix}$	$\begin{pmatrix} -\cos(\theta) \\ 0 \\ \sin(\theta) \end{pmatrix}$	$\begin{pmatrix} 1 \\ 0 \\ 0 \end{pmatrix}$
$-\vec{e}_z$	$-\vec{e}_x$	$-\vec{e}_y$	$\vec{e}_z$	$\vec{e}_x$

Figure 5.1: (Top) Sketch of the different MTJs considered in this section.
(Middle) Orientations of the magnetizations and the torque components.
(Bottom) The table gives the directions of the (equilibrium) magnetic moments $\vec{M}_{eq}^{L/R} = M_s^{L/R}\,\vec{e}_{L/R}$ and for the decomposition of the torque (eq. (5.2c)) for a general angle θ and for $\theta = 90°$.
(figure modified from [A5])

5 Results – Spin-transfer torque

5.1 Introduction and method

In the preceding sections we only considered collinear (P or AP) alignments of the magnetizations in the ferromagnetic leads of the MTJs. For non-collinear alignments, i.e. configurations with an arbitrary angle θ between the magnetizations, new effects develop. To generate non-collinear configurations in our calculations we start from self-consistent potentials for P alignment and rotate the exchange field (i.e. the spin-dependent part of the Hamiltonian, see eq. (2.10)) for lattice sites right of the center of the barrier in the x-z-plane from[15] $-\vec{e}_z$ to $\vec{e}_R = -\vec{e}(\theta)$; the directions are illustrated in figure 5.1. In practice, this is accomplished by rotating the combined spin-dependent t-matrix in spin space [28]. We remind that in our non-relativistic calculations only the relative angle between the magnetizations is important; thus, the other two degrees of freedom of a general rotation can be disregarded. Further, no correlations between the orientations in real space and spin space (e.g. from spin-orbit interaction) need to be considered.

For an infinite barrier the magnetization in the right lead would follow the rotation of the

[15]Note that (because of the sign in eq. (2.10b)) the magnetization and exchange field are anti-parallel to the spin polarization/majority-spin direction.

exchange field; thus, for the net magnetic moment on site i we expect $\vec{M}^i_{eq} = M^i_s \, \vec{e}_R$, where $M^i_s = \left| \int_{V_i} \mathrm{d}\vec{r} \, \vec{m}_{eq}(\vec{r}) \right|$ is the (equilibrium) saturation magnetic moment. However, in the non-collinear MTJ we obtain a small part of the magnetization in the right lead $\delta\vec{m}$, which is not aligned with the exchange field; the different contributions to $\delta\vec{m}$ are discussed later. The exchange field exerts a torque on this magnetization [5, 52]

$$\delta\dot{\vec{m}} = -\gamma_S \, \delta\vec{m} \times \vec{\Delta}, \tag{5.1}$$

which leads to a (counterclockwise) precession of $\delta\vec{m}$ around $\vec{\Delta}$, analogous to the Larmor precession in a magnetic field. Conversely, by conservation of angular momentum, this means that $\delta\vec{m}$ exerts an equal and opposite torque on the local magnetic moment $\vec{M}^i$, which is the source of the exchange field; for site i we obtain the spin-transfer torque [57, 59] (STT)

$$\vec{\tau}^i = \dot{\vec{M}}^i \Big|_{\mathrm{STT}} = -\int_{V_i} \mathrm{d}\vec{r} \, \delta\dot{\vec{m}}(\vec{r}) \tag{5.2a}$$

$$= \gamma_S \int_{V_i} \mathrm{d}\vec{r} \, \delta\vec{m}(\vec{r}) \times \vec{\Delta}(\vec{r}) \tag{5.2b}$$

$$= \tau^i_{ip} \, \vec{e}_{ip} + \tau^i_{op} \, \vec{e}_{op}. \tag{5.2c}$$

Note that in this work the torque has units of change in magnetization (not angular momentum) per time.

The STT enters as a driving term in the Landau-Lifshitz-Gilbert(-Slonczewski) (LLG) equation [83, 48, 124], a differential equation of motion for the magnetization in a ferromagnet, which is widely used in micromagnetics (see e.g. [110]). The LLG equation describes rotations of the direction of the magnetization $\vec{M}$ while its magnitude $|\vec{M}| = M_s$ is assumed to be fixed to the saturation magnetization M_s[16]. The LLG equation can include terms describing the inter-atomic exchange (Heisenberg exchange) and other coupling mechanisms, a phenomenological damping, and external and internal magnetic fields. It may further include spin-orbit related terms (e.g. anisotropy), finite-temperature effects, and others [22]. The required parameters can often be obtained by *ab initio* calculations [87, 5, 41]. The LLG equation usually assumes a continuous magnetization but can also (with some modifications) be applied to discrete (e.g. atomic) magnetic moments, which basically results in an extended classical Heisenberg model. In the macrospin approximation one can also treat larger collinear parts of the magnetization as a single magnetic moment.

Eq. (5.1) is equivalent to the motion of a localized, isolated spin in an external magnetic field $\vec{\Delta}$. In contrast, here the spins are carried by itinerant, interacting electrons and eq. (5.1) is obtained from the electronic equation of motion [5, 52]. Furthermore, we need to take into account that $\vec{\Delta}$ is itself a functional of the electronic density and magnetization. Therefore, the derivation of eq. (5.1) relies on the adiabatic approximation [5, 15, 52]: the slow motion of the magnetization (more precisely of the direction of the magnetization) can be separated from the fast electronic motion. The electronic Hamiltonian contains the orientations as parameters; conversely, the torque acting on the magnetization is determined by the electronic system. This is analogous to the Born-Oppenheimer approximation for the slow motion of the atomic nuclei. The adiabatic approximation is justified by comparing magnetic energies (inter-atomic exchange parameters) with electronic energies (exchange splitting, bandwidth) [5]. Additionally, we can use $\delta\vec{m} \ll \vec{m}_{eq}$ to justify using the equilibrium exchange field in eq. (5.1) [52]. The derivation in refs. [52, 103] actually focuses on a change $\delta\vec{\Delta}$ in the exchange field created by the non-collinear magnetization $\delta\vec{m}$, which acts on the equilibrium magnetization $\vec{m}_{eq}$. They find $\delta\vec{\Delta} = \frac{\Delta}{m_{eq}} \, \delta\vec{m}$, thus this equivalent point of view yields the same result.

There are two contributions to the non-collinear magnetization in the right lead. First, there are electrons tunneling from the left, which are spin-polarized in the direction of $\vec{e}_L$. Additionally, electrons coming from the right which are reflected at the barrier can become non-collinear to

[16] The somewhat similar Bloch-Torrey equation [138] includes diffusion, relaxation, and dephasing of the magnetization and can be used e.g. to describe injected spin currents in a non-magnetic material.

$\vec{e}_R$. Because of the non-collinear alignment of the leads, the transmission and reflection of the barrier are non-diagonal in spin space. Consequently, in both cases the electrons can become non-collinear. For both contributions the driving force can be an applied bias voltage or diffusion. In the latter case, electrons below the Fermi-energy (or the lower limit of the energy window created by the bias voltage) tunnel in both directions; their charge currents cancel but they can still create a torque on the layers.

From the previous sections on TMR we know that the current is dominated by Δ_1-like electrons whenever these states are present in both leads. This is always the case for non-collinear magnetizations, since the majority states in both leads always have a finite overlap. Thus, the majority $\Delta_1^\uparrow$ states provide the dominant contribution to the torque. The non-collinear states contributing to $\delta\vec{m}$ are linear combinations of majority and minority states. Thus, the observed precession is a result of interference between both components [59] and is caused by the difference in their wave vectors, which in turn is a consequence of the exchange splitting. For most states one of the spin components is evanescent, in particular the minority component for the Δ_1 states at E_F. These components decay exponentially away from the barrier. This also means that the electrons become polarized along a collinear direction (majority for Δ_1 states). Thus, the contributions to the torque decay away from the barrier. This is important since without the decay the contributions would mostly average to zero. This is different in junctions with a metallic spacer instead of a tunnel barrier (GMR structure). In this case also a decay occurs, but it results from dephasing between contributions with different precession frequencies and the decay is slower [59].

We assume that the magnitude of the magnetic moments remains unchanged; therefore, the torque must be perpendicular to the magnetic moment on which it acts. In eq. (5.2c) we have introduced a decomposition of the torque in the right lead into two components. The *in-plane* (IP or damping-like) component lies in the plane spanned by $\vec{e}_L$ and $\vec{e}_R$ and rotates $\vec{M}^R$ in that plane towards or away from $\vec{e}_L$. The *out-of-plane* (OP or field-like) component is perpendicular to this plane and causes a precession of $\vec{M}^R$ around $\vec{e}_L$, which leaves θ unchanged. The definition of the directions is given in figure 5.1. Despite their similar origins, we find that the two components behave quite differently.

In the following sections we mostly focus on the net torque exerted on the right ferromagnetic slab $\vec{\tau}^R = \sum_{i\in R} \vec{\tau}^i$. In a macrospin picture we can assume that the total magnetic moment of the right lead rotates under the influence of $\vec{\tau}^R$.

5.2 Spin-transfer torque from spin currents

In this section we introduce an alternative method to calculate the in-plane component of the STT developed by Slonczewski [121]. It is based on (global) conservation of angular momentum and the evaluation of spin currents. Since the latter are related to currents which have already been discussed, this approach is very useful to understand the results obtained via eq. (5.1). Additionally, it allows to obtain some general relations for the torques.

As explained above, most non-collinear contributions to the transport decay away from the barrier. Thus, we can assume that at some point in the left/right lead the current is completely polarized along $\vec{e}_{L/R}$ and can be decomposed into majority and minority component $I^{L/R} = I_\uparrow^{L/R} + I_\downarrow^{L/R}$. (As usual, $\uparrow$ and $\downarrow$ indicate the local majority and minority spin.) We define the spin current at this point as [128, 123]

$$\vec{I}_S^{L/R} = (I_\uparrow^{L/R} - I_\downarrow^{L/R})\,\vec{e}_{L/R} = I_S^{L/R}\,\vec{e}_{L/R}, \tag{5.3}$$

which describes the polarization of the current. Note that the sign of I_S depends on whether the current is majority- or minority-dominated ($|I_\uparrow| \gtrless |I_\downarrow|$) and also on the sign of the bias voltage and currents. In contrast to other definitions in the literature, this spin current is usually accompanied by a charge current. Unlike the charge currents, the spin currents in both leads can differ in magnitude (and of course orientation). Assuming angular momentum conservation, the net torque on both leads must be equal to the difference between $\vec{I}_S^R$ and $\vec{I}_S^L$. Thus, we obtain

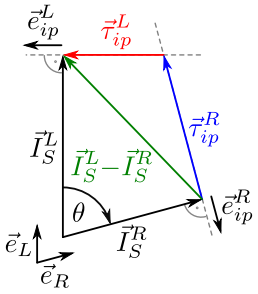

Figure 5.2: Relation between the in-plane torques and the spin currents implied by eq. (5.4) for an arbitrary angle θ (assuming the electrons are tunneling from left to right and $I_S^{L/R} > 0$); the prefactor is suppressed.

[121] (considering the direction of the electrons)

$$\vec{\tau}^R + \vec{\tau}^L \overset{V\geq 0}{=} \frac{\mu_B}{e}\left(\vec{I}_S^R - \vec{I}_S^L\right) \overset{V\leq 0}{=} \frac{\mu_B}{e}\left((-\vec{I}_S^L) - (-\vec{I}_S^R)\right), \tag{5.4}$$

where the prefactor converts from charge to magnetization. By assumption, both spin currents and thus the right-hand side of eq. (5.4) lie in the plane spanned by $\vec{e}_L$ and $\vec{e}_R$. Hence, considering the perpendicular direction (along $\vec{e}_{op}$, figure 5.1) we obtain a general relation

$$\vec{\tau}^R_{op} + \vec{\tau}^L_{op} = 0 \tag{5.5}$$

relating the OP components (eq. (5.2c)) on both sides. This means that the OP component describes an exchange of angular momentum, i.e. a coupling, between both leads. Note that it is nonetheless strongly influenced by the bias voltage and currents. On the other hand, the IP component describes a torque which is induced by the current. At zero bias the currents, spin currents, and the right-hand side of eq. (5.4) vanish and we find that the IP components vanish

$$V = 0 \quad \Rightarrow \quad \vec{\tau}^R_{ip} + \vec{\tau}^L_{ip} = 0 \quad \Rightarrow \quad \tau^R_{ip} = \tau^L_{ip} = 0, \tag{5.6}$$

since the directions of $\vec{\tau}^R_{ip}$ and $\vec{\tau}^L_{ip}$ are linearly independent for non-collinear alignment. This is not the case for the OP component, which can have finite contributions from diffusing electrons without a net charge current. In the presence of spin currents the IP components are the vector decomposition of the net spin current $\vec{I}_S^R - \vec{I}_S^L$ into the junction; this is illustrated in figure 5.2 (the signs and directions are discussed in the next section). By projecting eq. (5.4) onto the direction $\vec{e}_L$ we obtain an explicit expression for τ^R_{ip}

$$-\tau^R_{ip}\sin(\theta) = \frac{\mu_B}{e}(I_S^R\cos(\theta) - I_S^L), \tag{5.7}$$

where we used $\vec{\tau}^L \perp \vec{e}_L$ and relations between the different unit vectors introduced in figure 5.1. For $\theta = 90°$ this simplifies to (including the analogous projection onto $\vec{e}_R$)

$$\tau^R_{ip}(90°) = \frac{\mu_B}{e} I_S^L(90°) \quad \text{and} \quad \tau^L_{ip}(90°) = -\frac{\mu_B}{e} I_S^R(90°). \tag{5.8}$$

The spin currents depend on the bias voltage and the angle θ. To proceed we introduce four currents $i_{\sigma\sigma'}$ connecting the spins on either side of the barrier in an equivalent circuit [121] via

$$\begin{aligned} I^L_\sigma &= i_{\sigma\uparrow} + i_{\sigma\downarrow} \qquad I^R_{\sigma'} = i_{\uparrow\sigma'} + i_{\downarrow\sigma'} \qquad I^L = i_{\uparrow\uparrow} + i_{\downarrow\downarrow} + i_{\downarrow\uparrow} + i_{\uparrow\downarrow} = I^R = I \\ I^L_S &= i_{\uparrow\uparrow} + i_{\uparrow\downarrow} - i_{\downarrow\downarrow} - i_{\downarrow\uparrow} \qquad I^R_S = i_{\uparrow\uparrow} + i_{\downarrow\uparrow} - i_{\downarrow\downarrow} - i_{\uparrow\downarrow}. \end{aligned} \tag{5.9}$$

Using the assumption that the states on either side are coupled only indirectly via the coherent, non-magnetic barrier (compare section 4.5), one can obtain explicit θ dependences for these currents [121] from the rotation transformation in spin space

$$i_{\uparrow\uparrow}, i_{\downarrow\downarrow} \propto \cos^2(\theta/2) \quad \text{and} \quad i_{\uparrow\downarrow}, i_{\downarrow\uparrow} \propto \sin^2(\theta/2).$$

These remain valid in the collinear limits P ($\theta = 0$) and AP ($\theta = 180°$), where we can identify the currents introduced in eq. (4.2); we obtain

$$\begin{aligned} i_{\uparrow\uparrow}(\theta) &= I_{\uparrow\uparrow} \cos^2(\theta/2) \quad i_{\downarrow\downarrow}(\theta) = I_{\downarrow\downarrow} \cos^2(\theta/2) \\ i_{\uparrow\downarrow}(\theta) &= I_{\uparrow\downarrow} \sin^2(\theta/2) \quad i_{\downarrow\uparrow}(\theta) = I_{\downarrow\uparrow} \sin^2(\theta/2). \end{aligned} \tag{5.10}$$

This means that the full angular dependence (at a fixed bias voltage) can be recovered from the four collinear currents. Using this we simplify the angular dependence of the various currents

$$I(\theta) = \frac{I_p + I_{ap}}{2} + \frac{I_p - I_{ap}}{2} \cos(\theta) \qquad (I_S^{L/R} \text{ and } I_\sigma^{L/R} \text{ analogous}) \tag{5.11}$$

and the in-plane torque given in eq. (5.7)

$$\tau_{ip}^R(\theta) = \frac{\mu_B}{e} \left((i_{\uparrow\uparrow} - i_{\downarrow\downarrow}) \tan(\theta/2) + (i_{\uparrow\downarrow} - i_{\downarrow\uparrow}) \cot(\theta/2) \right) \tag{5.12a}$$

$$= \frac{1}{2} \frac{\mu_B}{e} \left(I_{\uparrow\uparrow} - I_{\downarrow\downarrow} + I_{\uparrow\downarrow} - I_{\downarrow\uparrow} \right) \sin(\theta) \tag{5.12b}$$

$$= \frac{\mu_B}{e} I_S^L(90°) \sin(\theta) = \frac{\mu_B}{e} \frac{I_{S,p}^L + I_{S,ap}^L}{2} \sin(\theta) \tag{5.12c}$$

$$\text{with} \quad I_{S,p}^L = I_{\uparrow\uparrow} - I_{\downarrow\downarrow} = I_{S,p}^R \quad \text{and} \quad I_{S,ap}^L = I_{\uparrow\downarrow} - I_{\downarrow\uparrow} = -I_{S,ap}^R. \tag{5.12d}$$

Thus, as a result of the combination of the θ dependence of the (spin) currents and the vector decomposition (figure 5.2), the IP torque has a simple $\sin(\theta)$ dependence and can be obtained from the spin current at $\theta = 90°$ in the other lead, which in turn is the average of the collinear spin currents.

As noted above, the OP component describes an interfacial coupling between the ferromagnetic slabs and is therefore often called interlayer exchange coupling (IEC) [23, 53]. It can be considered as the result of a Heisenberg-like coupling between the magnetizations [120]

$$H_{iec} = -J \vec{M}^L \vec{M}^R = -J M^L M^R \cos(\theta) \tag{5.13a}$$

$$\Rightarrow \quad \vec{\tau}_{op}^R = \vec{\tau}_{iec}^R = -\gamma_s J \vec{M}^R \times \vec{M}^L = -\gamma_s J M^R M^L \sin(\theta) \vec{e}_{op}^R = -\vec{\tau}_{iec}^L. \tag{5.13b}$$

The coefficient J may depend on the bias voltage but not on the angle θ. Thus, τ_{op} has the same angular dependence as τ_{ip}. For positive (negative) J this coupling energetically favors the P (AP) state and leads to a counterclockwise (clockwise) rotation of the magnetizations around each other. From the perspective of the free layer it is equivalent to a (homogeneous) external magnetic field $J \vec{M}^L$. In eq. (5.13a) we only consider the lowest-order coupling; higher orders correspond to repeated tunneling between both leads and only matter for very thin barriers.

Until now, no symmetry of the junction has been assumed and the above results remain valid for asymmetric junctions. For a symmetric junction we find additional relations by considering a rotation of the junction (compare section 4.5). We obtain (with the directions defined in figure 5.2)

$$\tau_{ip}^L(+V) = \tau_{ip}^R(-V) \quad \text{and} \quad \tau_{op}^L(+V) = \tau_{op}^R(-V) \quad \text{for a symmetric junction.} \tag{5.14a}$$

By combining the latter relation with eq. (5.5) we find that the OP component is symmetric in V

$$\tau_{op}^R(+V) = \tau_{op}^R(-V) \quad \text{for a symmetric junction,} \tag{5.14b}$$

when eq. (5.4) is applicable. Note that no similar relation holds for τ_{ip} as discussed below.

5.3 Bias-voltage dependence of the STT

In this section we discuss the bias dependence of the STT in junctions with pure Fe, $Fe_{50}Co_{50}$, and pure Co leads. The net torque on the free (right) layer is calculated using eq. (5.2) for an

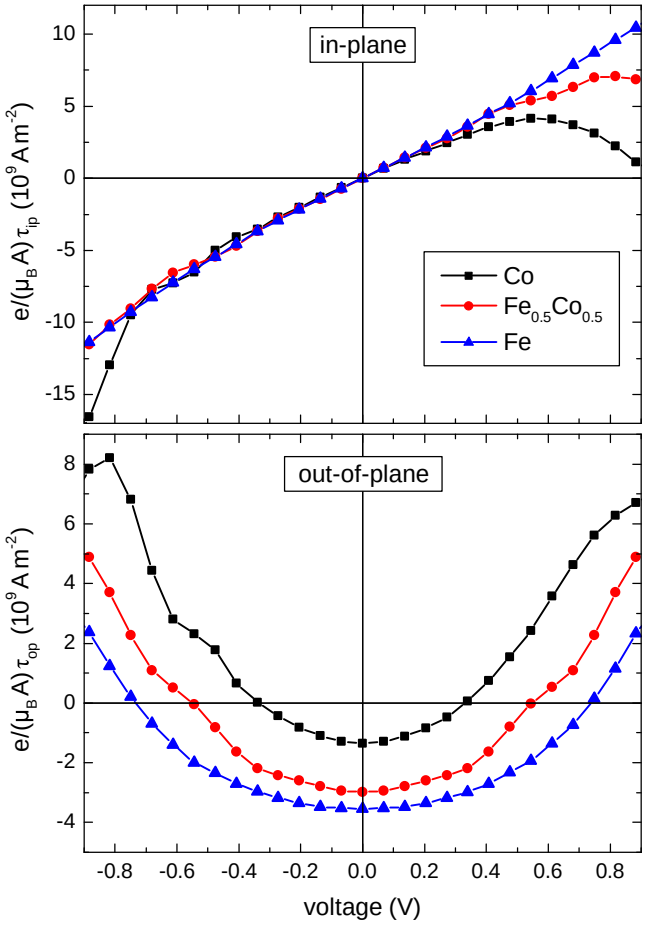

Figure 5.3: Net spin-transfer torque (per junction area) exerted on the free layer as a function of the bias voltage calculated using eq. (5.2) for junctions with Fe, $Fe_{50}Co_{50}$, and Co ferromagnetic slabs and a six-monolayer MgO barrier for an angle $\theta = 90°$ between the magnetizations. A thickness averaging is performed for the Fe and Co slabs; for $Fe_{50}Co_{50}$ 20 monolayers are considered. The prefactor e/μ_B converts the units from 'change in magnetization' to charge current. [A5]
The calculations for the pure material were performed by M. Czerner [29].

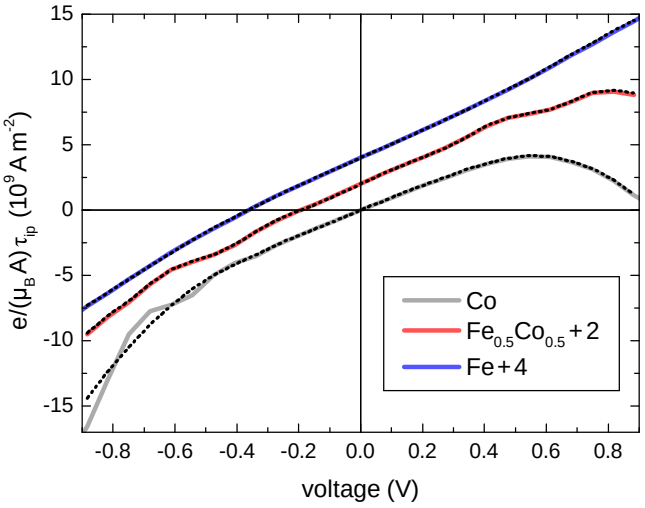

Figure 5.4: Bias-voltage dependence of the in-plane component of the STT from figure 5.3 (solid, colored) compared to the result calculated from spin currents via eq. (5.12) (dashed, black) for the same setup. The curves for different lead materials are shifted to improve visibility. [A5]

angle $\theta = 90°$ between the non-collinear magnetizations in both leads; the results are shown in figure 5.3.

The energy integration required to obtain $\delta\vec{m}$ splits into two parts: In the energy window $[\mu_L, \mu_R]$ created by the bias voltage only states for one direction are occupied (assuming zero temperature) and the contributions to $\delta\vec{m}$ are calculated from NEGFs (section 2.4). In the energy range $(-\infty, \min(\mu_L, \mu_R)]$ both directions are occupied and the contributions can be calculated from equilibrium GFs using a complex-energy contour integration [150]. This part describes diffusion in both directions without a net charge current and only contributes to τ_{op}. Calculating vertex corrections for the non-collinear system (for the NEGF part for FeCo leads) is computationally very expensive; therefore, we omit the thickness averaging for the junction with FeCo alloys. In this case, the quantum-well states cause some weak oscillations, which are visible in the results.

In addition to the result via $\delta\vec{m}$ we calculate the IP component of the STT from spin currents using eq. (5.12), where we can reuse the bias-dependent conductances from section 4.5 (figure 4.23). This is compared to the result from eq. (5.2) in figure 5.4. Except for Co leads at large negative bias we find perfect agreement between both methods; thus, the spin-current approach can be used in explanations. One can show that STT via $\delta\vec{m}$ is equivalent to local conservation of angular momentum [52, 114]. Since we do not consider spin scattering, we have global conservation of angular momentum, which explains the perfect agreement (the deviation for Co are discussed later). Note that, since all magnetizations within one lead are aligned, the disorder scattering for FeCo alloys does not lead to a scattering between both spins.

We start by discussing the IP component of the STT. At zero bias τ_{ip} vanishes. At small bias $\tau_{ip}(V)$ is linear with a similar slope for all three materials. This can be understood from the spin currents via eq. (5.12b). For sufficiently small bias voltages all conductances are basically constant (figure 4.23) leading to linear (spin) currents. In particular, the dominating $G_{\uparrow\uparrow}$ is independent of the bias and also of the Co concentration (see also next section). To understand the direction of τ_{ip} we consider the case of electrons tunneling from left to right and majority-dominated spin currents in both leads, which is illustrated in figure 5.2. (By our convention this corresponds to a negative bias voltage and currents, and the artificial sign in eq. (5.4, $V < 0$) is included in the spin currents.) We find that the torque is oriented to rotate the free layer $\vec{M}^R$ in the $\vec{e}_{L/R}$-plane towards the direction of the fixed layer $\vec{M}^L$ (which by our convention for $\vec{e}_{ip}$ corresponds to a negative value of τ_{ip}). The net magnetization of the current tunneling into the

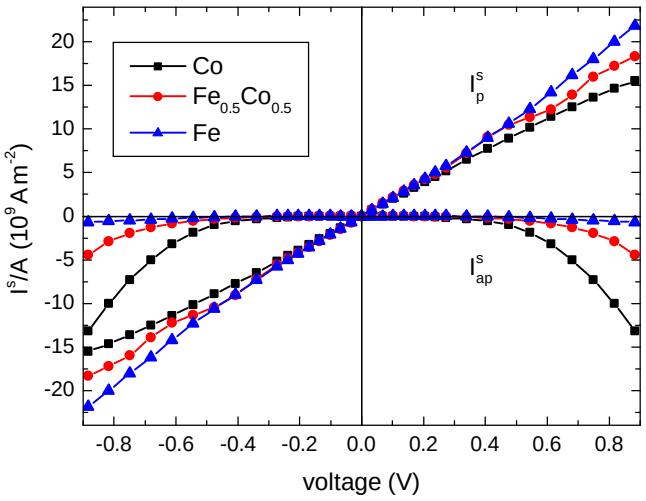

Figure 5.5: Bias-voltage dependence of the spin currents in the left lead (i.e. the fixed layer) for P and AP alignment (eq. (5.12d)), which control the in-plane torque in the right lead (eq. (5.12c)). Note that $I^L_{S,p}$ is always majority-dominated but $I^L_{S,ap}$ is minority- (majority-)dominated for positive (negative) bias. [A5]

right lead is oriented along $\vec{e}_L$ and rotates $\vec{M}^R$ towards that direction. In contrast, the torque on the fixed layer is oriented to rotate $\vec{M}^L$ away from $\vec{M}^R$ (figure 5.2, eq. (5.8)), i.e. to increase θ. This torque is created by a decaying spin current of reflected electrons in the left lead, which have their magnetic moments oriented along $-\vec{e}_R$ to compensate for the spin current in the right lead (oriented along $+\vec{e}_R$). By analogy (or eq. (5.14a)) this explains the IP torque on the free layer for positive bias voltages.

For larger bias voltages we observe a deviation from the simple linear dependence, which is asymmetric in V and becomes more pronounced with increasing Co concentration. It leads to a reduction (enhancement) of τ_{ip} for large positive (negative) bias. For pure Co it even leads to an inversion of the direction of the torque at large positive bias (at 0.97 V, outside the plot range). This can be explained from the collinear spin currents, which contribute to τ_{ip} via eq. (5.12c); these are shown in figure 5.5. From the symmetry of the collinear conductance channels (eq. (4.5)) we can infer the symmetry of the spin currents (for symmetric junctions)

$$I^{L/R}_{S,p}(-V) = I^{L/R}_{S,p}(+V) \quad \text{and} \quad I^{L/R}_{S,ap}(-V) = -\,I^{L/R}_{S,ap}(+V), \tag{5.15}$$

which means that it is different for $I^L_{S,p}$ and $I^L_{S,ap}$; hence, the IP torque is asymmetric, since it is proportional to the sum of both. For negative bias both contributions add up while for positive bias they cancel each other. For AP alignment and sufficiently large negative bias (Fe: $V \lesssim -0.3$ V; FeCe, Co: $V < 0$ V) the spin current in the left lead is majority-dominated and increases with the negative bias voltage because of an increase in $G_{\uparrow\downarrow}$. Concurrently, the spin current in the right lead is minority-dominated ($I^R_{S,ap} = -I^L_{S,ap}$, eq. (5.12d)) and the same effect leads to an increase in the negative polarization. For non-collinear alignment these spin currents mix with the majority-dominated P spin currents $I^{L/R}_{S,p}$ (eq. (5.12c)), which leads to an enhancement (attenuation) in the left (right) lead. For $\theta = 90°$ the net spin currents in both leads remain majority-dominated for all considered materials and shown bias voltages. Since the IP torque is proportional to the spin current at $\theta = 90°$ (eq. (5.12c)), the discussion above (in combination with eq. (5.14a)) explains the observed bias dependence. The increase in $G_{\uparrow\downarrow}$ is a result of minority $\Delta_1^\downarrow$ states which shift into the bias window at large bias or large Co concentration as explained in section 4.5. Thus, we can understand the bias voltage and Co composition dependence of τ_{ip} from the corresponding discussion in that section.

Next, we discuss the OP component of the torque (figure 5.3). For all three compositions

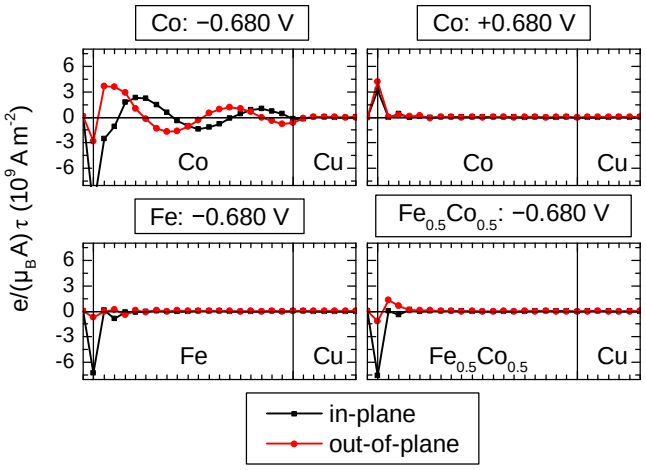

Figure 5.6: Layer-resolved spin-transfer torque in the free layer for different lead materials and bias voltages. [A5]

the OP torque is negative at zero bias and increases to positive values for positive and negative bias voltages. For Fe and FeCo the bias dependence is symmetric as expected from eq. (5.14b). However, for Co we observe a deviation from this symmetry; from the smoothness of the curve for positive bias we may assume that the deviations originate at negative bias, just as for the IP component. Unfortunately, the method using spin currents discussed in section 5.2 does not provide the means to calculate the OP component. This would require knowledge of the OP component of the spin currents inside the barrier [120, 128], which cannot be obtained from the four collinear conductance channels. We can use the interpretation as an IEC (eq. (5.13)) to understand the physical significance of the OP component. The negative value at zero bias $\tau_{op}(0)$ implies that the coupling coefficient J is positive, which means that the IEC favors the P state. The IEC can also be obtained from total (band-)energy calculations by calculating the energy of the junction as a function of θ and fitting the angular dependence from eq. (5.13a). We have verified for several cases that this yields the same $\tau_{op}(0)$ and that the P state has indeed the lowest energy (not shown). For all three materials the OP torque changes sign at a certain (positive and negative) bias voltage; thus for larger bias the IEC favors the AP state. Because of a reduction in $|\tau_{op}(0)|$ and an increased curvature the necessary bias voltage reduces with the Co concentration from ± 0.74 V for Fe to ± 0.34 V for Co.

To understand the bias dependence we may assume that eq. (5.5) holds separately for each energy and direction of the tunneling electrons ($L \rightleftarrows R$). As a result, for a symmetric junction at zero bias the contributions for both directions are equal. In the limit of vanishing bias we can neglect the bias dependence of $\tau_{op}(E;V)$. Then, when applying a small bias voltage, the additional contributions above $\bar{\mu} = (\mu_L + \mu_R)/2$ for one direction are largely canceled by removing the contributions for the other direction below $\bar{\mu}$. For all three materials, the energy-resolved contributions to the OP torque in the vicinity of the Fermi-energy (not shown) are positive and show an increase with energy, which leads to the observed positive curvature of the bias dependence. For iron we find a rather simple bias dependence, which can be well described by a biquadratic polynomial ($\tau_{op}(V) \approx a + bV^2 + cV^4$) with positive coefficients $b \approx c > 0$ (with c scaled by 1 V^2). For FeCo a similar dependence is superimposed with oscillations from quantum-well states; the curve is narrower than for Fe ($0 < c < b$). For Co (considering only positive bias) the curve is still narrower and the curvature changes sign at a large bias voltage. In a biquadratic approximation we find $c < 0 < b$ and $|c| < |b|$. It seems plausible that the origin of this concentration dependence is related to the same effects that govern the IP component.

We still need to explain the deviations of the STT for Co at negative bias from the behavior predicted in section 5.2. For the IP component this is observed as a deviation from the result via

spin currents (figure 5.4), while for the OP component it results in an asymmetry in the bias-voltage dependence (figure 5.3). In both cases, the deviations oscillate and increase in amplitude and 'wavelength' with the negative bias voltage. The origin of these deviations is identified by investigating the layer-resolved torque, which is shown in figure 5.6 for different cases. In all cases, both components of the torque oscillate and decay away from the barrier as expected from the discussion in section 5.1. For Fe and FeCo and also for Co at positive bias the decay is very rapid and extends only over few (≈ 5) monolayers. On the other hand, for Co at negative bias the decay is slow and not completed within the finite-width Co slab. This means that the current emitted into the right copper lead is (and remains) incompletely polarized along $\vec{e}_R$. Thus, in this case the assumption in section 5.2 that the current becomes completely polarized sufficiently far from the barrier cannot be fulfilled and the predictions may be violated. Some angular momentum is lost via the emitted current and does not contribute to the torque. Since the OP torques on both leads are not equal, an interpretation as IEC is not valid in this case (the emitted angular momentum is not exchanged between both leads). Note that neither polarizing an unpolarized incoming current nor emitting a polarized current into a non-magnetic lead causes a torque. In the introduction, the decay of the STT was explained from an exponential decay of evanescent states for one spin. However, for Co the minority spin $\Delta_1^\downarrow$ states are close above the Fermi-energy and contribute at increased negative bias via the $\uparrow\downarrow$ channel (section 4.5). These states and their contribution to the torque do not decay. Thus, a decay of the torque can only occur due to dephasing. This decay is much slower, in particular since the relevant contributions are strongly localized in $\vec{k}_\parallel$-space (figure 4.24), which explains the decay observed in figure 5.6. The contribution of minority $\Delta_1^\downarrow$ states increases with the negative bias voltage, which explains the observed bias dependence of the deviations.

5.4 Material dependence of the STT

In this section we systematically investigate the dependence of the STT on the FeCo-alloy composition in the ferromagnetic slabs. We analyze the torque at $\theta = 90°$ for small bias voltages by calculating a Taylor expansion around zero bias. The results are given in figure 5.7, which shows the torque and its first and second derivative with respect to the bias voltage at zero bias for the IP and OP component. These coefficients are discussed separately.

The IP component of the torque $\tau_{ip}(0)$ vanishes at zero bias for all concentrations in accordance with eq. (5.6). This remains true for asymmetric junctions. One can show [114] that in equilibrium $\delta\vec{m}$ lies in the plane spanned by $\vec{e}_{L/R}$; thus, this result is more general than eq. (5.4) and also holds for the layer-resolved torque. The OP component $\tau_{op}(0)$ is negative for all concentrations and constitutes an (equilibrium) IEC which favors the P state. It shows a decrease in negative value with the Co concentration to 38% at Co of its value at Fe. The dependence is somewhat similar to the Slater-Pauling curve, i.e. a transition from a (slight) increase at low concentrations to a linear decrease at high concentrations. This OP torque includes large oscillating contributions in the energy range where the oxygen-2p-like states render the MgO barrier metallic. Thus, $\tau_{op}(0)$ is largely based on cancellation and we make no attempt to rationalize the observed dependence. Because of these complicated contributions, $\tau_{op}(0)$ may be sensitive to the computational details.

The first derivative of the torque with respect to the bias voltage $\vec{\tau}' = \frac{\mathrm{d}\vec{\tau}}{\mathrm{d}V}$ is called torkance [122]. Since the OP component is symmetric in V for a symmetric junction (eq. (5.14b)), the OP torkance $\tau'_{op}(0)$ must vanish at zero bias, which is fulfilled for all concentrations. The IP torkance $\tau'_{ip}(0)$ is almost independent of the Co concentration; it shows only a small decrease of 6% from Fe to Co and some weak fluctuations. This concentration dependence is very different from the one of the TMR (figure 4.16). As explained in section 4.4 the TMR is governed by the AP conductance, while the P conductance is basically independent of the Co concentration (and also the bias voltage). Since $G_{\uparrow\downarrow}(0) = G_{\downarrow\uparrow}(0)$ for symmetric junctions (eq. (4.5)), the contribution of the AP spin current to the IP torkance vanishes at zero bias and remains small until one of the AP channels dominates the AP transport (figure 5.5). More general, the much larger P contribution outweighs a small AP contribution to τ_{ip}, unlike for TMR where the AP

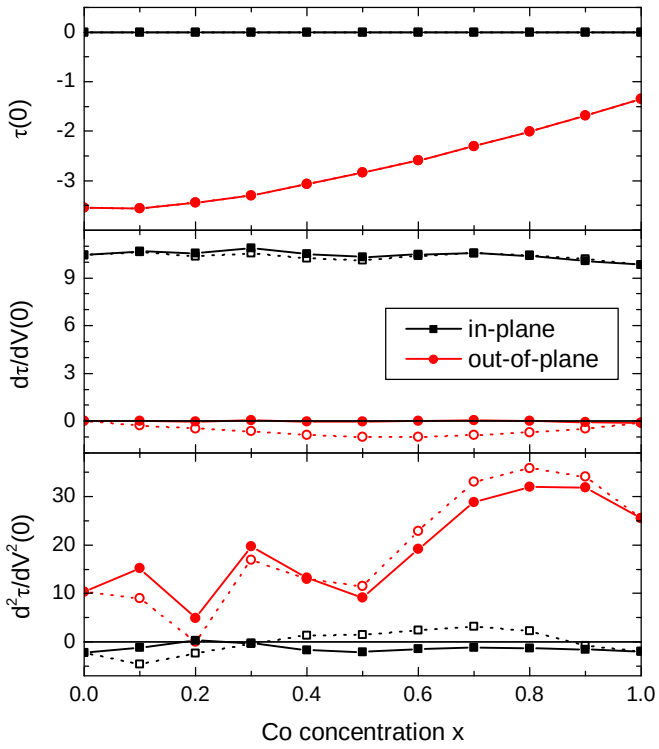

Figure 5.7: Cobalt-concentration dependence of the spin-transfer torque exerted on the free layer at $\theta = 90°$ for small bias voltages. The figure shows the coefficients of a Taylor expansion around $V = 0$: $\tau(V) \approx \tau(0) + \frac{\mathrm{d}\tau}{\mathrm{d}V}(0)\ V + \frac{1}{2}\frac{\mathrm{d}^2\tau}{\mathrm{d}V^2}(0)\ V^2$ for the in-plane and out-of-plane component. The coefficients include a prefactor $\frac{e}{\mu_B}$ and their units are 10^9 Am^{-2} for $\frac{e}{\mu_B}\,\tau$, 10^9 $\Omega^{-1}\mathrm{m}^{-2}$ for $\frac{e}{\mu_B}\,\frac{\mathrm{d}\tau}{\mathrm{d}V}$, and 10^9 $\Omega^{-1}\mathrm{V}^{-1}\mathrm{m}^{-2}$ for $\frac{e}{\mu_B}\,\frac{\mathrm{d}^2\tau}{\mathrm{d}V^2}$; they are calculated via a quadratic fit (or a finite difference method) from data points at 0 V and ±68 mV. The thickness averaging for the FeCo slabs is included in this calculation. The dashed lines indicate the result obtained neglecting vertex corrections. Note that $\tau(0)$ is calculated from equilibrium GFs only and contains no vertex corrections. [A5]

conductance appears in the denominator. Since $G_{\uparrow\uparrow} \gg G_{\downarrow\downarrow}$, the IP torkance is governed by the $\uparrow\uparrow$ channel, which explains the weak concentration dependence (compare figure 4.17). One might expect a contribution from the minority IRS for pure iron, which leads to a relatively large $G_{\downarrow\downarrow}(0)$ and thus reduces the P spin current. However, since this contribution diminishes rapidly at finite bias, it is not observed in our result based on data points at finite bias. It could be recovered via linear-response calculations [59] or by calculating the IP torkance from the conductance channels via eq. (5.12). The latter approach yields a torkance $\tau'_{ip}(0) = 9.11 \cdot 10^9\ \Omega^{-1}\mathrm{m}^{-2}$ for iron, which is smaller than the Co value.

As observed in section 5.3, the IP torque is linear at small bias; thus, the second derivative at zero bias $\tau''_{ip}(0)$ is expected to be small (but not necessarily zero). This is confirmed by the results, which show a small negative value. By taking the second derivative of eq. (5.12b) and using the symmetry relations eq. (4.5) we find that only the AP channels contribute to $\tau''_{ip}(0)$ for symmetric junctions. The exponential increase for some of the AP spin currents has little effect at small bias. Of course, the symmetry argument only holds for symmetric junctions; some of the asymmetric junctions entering in the thickness averaging show a considerable $\tau''_{ip}(0)$ comparable to the OP component. The second derivative for the OP component $\tau''_{op}(0)$ is positive for all concentrations and shows an increase with the Co concentration. For Co it has almost 2.5 times the value at Fe. This increase has already been noted in section 5.3, where we found that the bias dependence becomes narrower with increasing Co concentration. We also found that concurrently the fourth derivative decreases with the Co concentration, which is not calculated here. The concentration dependence shows a rather complicated structure; however, this might be an artifact from quantum-well states, which has not been removed by the thickness averaging.

Figure 5.7 also shows the result which would be obtained if diffusive contributions (i.e. the vertex corrections) were neglected. Since calculating the vertex corrections for this case is computationally expensive, it might be tempting to simply neglect this contribution. At first sight, the deviations for this case seem not very significant; in particular the important IP torkance is well reproduced (because the dominating majority Δ_1 states are only weakly affected by the disorder). However, on closer consideration one notes that the OP torkance $\tau'_{op}(0)$ obtains a finite value in violation of the symmetry of the junction. This is also observed in the full bias dependence of the OP component $\tau_{op}(V)$ for $Fe_{0.5}Co_{0.5}$, which becomes asymmetric (not shown). Furthermore, $\tau''_{ip}(0)$ obtains a positive sign for some concentrations, which implies the wrong curvature of the bias dependence for the IP torque compared to the full results. Thus, neglecting the vertex corrections leads to qualitatively wrong and even 'unphysical' results.

5.5 Discussion and experimental results

For the IP component of the STT the expression in terms of spin currents (eq. (5.12)) allows for a clear and comprehensive understanding. In the previous sections we showed that the IP torque is completely determined by Δ_1 states, which dominate the relevant (spin) currents. The other, small contributions, which are important for the TMR, have little influence on the IP torque. Thus, we could further simplify the discussion by neglecting conductance channels without Δ_1 contributions, i.e. the $\downarrow\downarrow$ channel and the $\uparrow\downarrow$ ($\downarrow\uparrow$) channel for $V > 0$ ($V < 0$). This corresponds to assuming an ideal, large-gap half-metal for the leads, whose band gap corresponds to the Δ_1-half-metallic region in our case. In this case the collinear spin currents and thus the IP torque could be obtained directly from the P and AP conductance. In experiments, inelastic scattering and other effects create additional contributions, which can affect all spin channels and can partially cancel for the spin currents; thus this approximation is only limitedly applicable. Conversely, if the torque and the conductances can be accurately measured, this allows to draw conclusions about these additional effects [122].

A major application of the STT is switching the magnetization of the free layer [35], which benefits from large torques. For the P spin current the maximal contribution to the IP torque is obtained if the $\downarrow\downarrow$ channel vanishes (which means that the P current is completely polarized). For the AP contribution the case is less clear. For a symmetric junction the AP spin current always leads to a reduction of τ_{ip} for one direction of the current (eq. (5.15)), which is unfavorable, since

switching is required for both directions. Thus, if large bias voltages are required for switching, our results favor small Co concentrations, since in this case the AP (spin) currents remain small. One might try to engineer an asymmetric junction in such a way that $G_{\uparrow\downarrow} \gg G_{\downarrow\uparrow}$ for both bias voltage polarities, which optimizes the IP torque on the free layer. Since we additionally require a large TMR at small bias, $G_{\uparrow\downarrow}$ should strongly increase above a convenient threshold voltage for both polarities and $G_{\downarrow\uparrow}$ should remain small. This way one can increase the IP torque on the free layer by an AP contribution while reducing the torque on the fixed layer, nearly obtain the optimal IP torque per current $\tau_{ip}/I_\perp \lesssim 1$ (eq. (5.16) below), and avoid an asymmetric bias dependence. If we retain the MgO barrier and choose e.g. an iron fixed layer, this would require a ferromagnetic free-layer material which has a small minority $\Delta_1^\downarrow$ band gap that is symmetric about the Fermi-energy. Of course, this discussion based on band engineering neglects other effects which are important, in particular the crystal and interface quality attainable for a chosen material combination.

Unlike the IP component of the STT, which directly rotates $\vec{M}^R$ towards or away from $\vec{e}_L$, the OP torque only causes a rotation of $\vec{M}^R$ around $\vec{e}_L$ and hence cannot directly contribute to the switching for the considered geometry. Nevertheless, in combination with damping it can have an impact on the angle θ. The IEC (eq. (5.13)) determines an energetically preferred collinear state and the damping should lead to a relaxation towards this alignment. However, the IEC energy is very small, e.g. for iron we have $\frac{e}{\mu_B}\tau_{op}(0) = -3.54 \cdot 10^9$ Am^{-2}, which corresponds to a coupling energy $J\,M^L\,M^R = 1.14 \cdot 10^{-6}$ Jm$^{-2} = (E_{ap} - E_p)/2$. This contribution competes with other energies like magnetocrystalline anisotropy energy (from spin-orbit interaction) or shape anisotropy energy (from magnetic dipole-dipole interaction), which can be considerably larger [A9]. The complicated interplay of the different effects can be investigated by micromagnetic simulations [22]. For cases where the OP component is important, our results indicate that the Co concentration can be used for tuning; in particular the offset at zero bias $\tau_{op}(0)$ and the sign changes can be controlled in a wide range.

The STT has been extensively studied in experiments. One method to measure the STT is via spin-transfer-driven ferromagnetic resonance [132] (ST-FMR). In these experiments, first an initial angle between the magnetizations is created by an external magnetic field. Then, a current with a microwave-frequency component is applied to the MTJ, which creates a time-dependent STT. This torque induces a small-amplitude precession around the initial orientation and the time-varying angle is measured via the resistance of the junction. The frequency is swept through a resonance of the induced precession of the magnetization. From the resulting signal the STT is extracted by fitting a macrospin-model equation obtained from the LLG equation. This procedure is quite intricate, which has led to misinterpreted results in some cases ([82], see [140]). Usually, these experiments measure a DC signal generated by mixing the oscillating current and resistance. In a more recent experiment [141] a time-dependent signal reflected by the sample is recorded and evaluated. The authors claim that this approach remains valid at high bias voltages [141], where the usual method suffers from strong artifacts [140]; at small bias they still use the DC method.

When comparing our results to experimental ones, one should keep in mind that some aspects are strongly influenced by the chosen symmetry of the junction. On the other hand, real junctions are not perfectly symmetric even if the same material and thickness is used for both ferromagnetic slabs, in particular since one layer has to be magnetically 'fixed' [17] and also because the interface quality at the barrier depends on the growth sequence. Additionally, the experimental junctions have a much smaller TMR, in particular since most STT experiments are carried out at room temperature; typical TMR values in this case are 80–150% depending on the barrier thickness, which means that I_{ap} is 56–40% of I_p. Since the IP torque is proportional to the currents, one needs to factor in the conductance for a quantitative comparison. Thus, a convenient quantity is the 'torque per current'

$$`\,\tau_{ip}/I_\perp\,' = \frac{\tau_{ip}(V, 90°)/\mu_B}{I(V, 90°)/e} \quad \text{or} \quad \frac{\tau'_{ip}(0, 90°)/\mu_B}{G(0, 90°)/e} \quad \text{at zero bias,} \tag{5.16}$$

[17] Typically, the layer is fixed by coupling it antiferromagnetically (via a metallic interlayer) to another ferromagnetic layer, which in turn is pinned by exchange bias (coupling to an antiferromagnet).

where one may replace $I(90°) = (I_p + I_{ap})/2$ and $\tau_{ip}(90°) = \tau_{ip}(\theta)/\sin(\theta)$ because of eqs. (5.11, 5.12c). Since each electron carries a magnetic moment of $1\,\mu_B$, the torque per current is bounded $|\tau_{ip}/I_\perp| \leq 1$ and obtains its maximum only in the idealized cases discussed above. For symmetric junctions at zero bias the AP channels do not contribute to τ_{ip}; thus, one can also consider '$\tau_{ip}/(I_p/2)$' $= \frac{\tau'_{ip}(90°)/\mu_B}{G_p/(2e)}$ instead, which becomes one for a completely polarized I_p. However, $\tau_{ip}/(I_p/2)$ may exceed one for asymmetric junctions (or finite bias voltages). Note that for symmetric junctions at zero bias this gives the polarization of the P conductance $\frac{\tau'_{ip}(90°)/\mu_B}{G_p/(2e)} = \frac{G_{\uparrow\uparrow}-G_{\downarrow\downarrow}}{G_{\uparrow\uparrow}+G_{\downarrow\downarrow}}$. From our results we find $\tau_{ip}/I_\perp > 91\%$ and $\tau_{ip}/(I_p/2) > 94\%$ at zero bias for all Co concentrations [18]. For negative bias $\tau_{ip}/I_\perp$ gets even closer to one, whereas for positive bias the value reduces with bias and Co concentration.

Of course, these idealized values are not obtained in experiments. As an example, we discuss the experimental results presented in ref. [115]. The considered junction contains $Fe_{0.25}Co_{0.75}$ leads (disregarding boron), a 1.25 nm MgO barrier, and shows a TMR of 154% at room temperature; it is remarkably symmetric (visible in $I'(V) \approx I'(-V)$ and $\tau'_{op}(0) \approx 0$). For this junction the STT is measured via ST-FMR at room temperature. From the presented results we obtain $\tau_{ip}/I_\perp = 60\%$ and $\tau_{ip}/(I_p/2) = 83\%$ at zero bias. The reason for these small values is related to the low TMR, which implies large AP and $\downarrow\downarrow$ currents and also a low polarization of the currents (i.e. small spin currents). The measured bias dependence of the IP torkance shows a slight linear decrease, which is superimposed by some oscillations. The linear decrease can be approximated by $\tau'_{ip}(V) \approx \tau'_{ip}(0)\,(1 + b\,V)$ for $|V| < 0.3$ V with $b = -0.27$ V^{-1}. This value might be underestimated due to neglected correction terms [140]. Taking into account these corrections, a larger value $b = -0.58$ V^{-1} is obtained for a similar junction [140]. This can be compared with the small negative $\tau''_{ip}(0)$ in figure 5.7, which yields values for b between -0.21 V^{-1} and -0.12 V^{-1} for Co concentrations $x \geq 40\%$. However, these numerical second-order derivatives are not very accurate. From a linear fit to $\tau'_{ip}(V)$ calculated via spin currents for $|V| < 0.3$ V we obtain $b = -0.29$ V^{-1} for pure Co, which is still smaller than the (corrected) experimental value (for Fe and $Fe_{0.5}Co_{0.5}$ $\tau'_{ip}(V)$ does not allow a credible linear approximation in that bias range). Possible reasons for this discrepancy include a slight asymmetry of the junction and additional contributions to the (spin) currents via inelastic scattering, which also lead to a quicker decrease of the TMR. For a junction with a very thin barrier and low TMR=92%, a smaller $\tau_{ip}/I_\perp = 40\%$, $\tau_{ip}/(I_p/2) = 61\%$, and a larger $b = 1$ V^{-1} were obtained in ref. [140]. The bias range where experimental results based on the DC ST-FMR method are accurate is too small to include clear signs of the non-linear contributions to τ_{ip} observed in our calculations for large Co concentrations. Using the time-resolved method STT measurements in a larger bias range $|V| < 0.6$ V were reported in ref. [141]. Unfortunately, the considered junctions have a very thin barrier, a low TMR, and also a relatively high asymmetry ($I'(V) \not\approx I'(-V)$). Because of the asymmetry, they obtain a strong decrease of $\tau'_{ip}(V)$ ($b = 8.8$ V^{-1}) at small bias $|V| < 0.2$ V, where the DC method is applied. Unexpectedly, this linear decrease flattens quite abruptly into a constant dependence at larger bias, where the time-resolved method is applied. This is in contradiction to our results, which predict a non-linear enhancement of the decrease. The reason for this discrepancy is unclear, but it might be related to the asymmetry. The experimental bias dependence might also include effects of quantum-well states in the thin FeCo slabs, which in our calculations cause a quite strong structure before the thickness averaging on a similar bias-voltage scale, which can obscure the expected increase. Thus, the experiment should be repeated with symmetric, high-TMR junctions with different FeCo-layer thicknesses, different Co concentrations, and at low temperature.

The ST-FMR experiments also measure the OP component of the STT. For τ_{op} we have no simple relation to the (spin) currents; however, one may assume that the bias-dependent part $\tau_{op}(V) - \tau_{op}(0)$ has a similar dependence on e.g. the barrier thickness as the current, since the coupling is transmitted by the conduction electrons. To cancel out this dependence we divide

[18] Here we neglect the contribution of the interface resonance state to the $\downarrow\downarrow$ channel for pure iron; including this effect in τ_{ip} and G reduces the torque per current to $\tau_{ip}/I_\perp = 76\%$ and $\tau_{ip}/(I_p/2) = 77\%$; however, it is likely that the effect is overestimated compared to experiments (see section 4.4.1).

by the IP torkance. All experiments discussed above measure a linear bias dependence of the OP torkance at small bias with $\tau'_{op}(0) \approx 0$. From the slope one obtains $\tau''_{op}(0)$, which determines the quadratic dependence of τ_{op} at small bias. For junctions similar to ours with high Co concentrations experimental values $\tau''_{op}(0)/\tau'_{ip}(0) = 1.3\ \mathrm{V}^{-1}$ [115] or $\tau''_{op}(0)/\tau'_{ip}(0) = 1.6\ \mathrm{V}^{-1}$ [140] were measured. These values can be compared with $\tau''_{op}(0)/\tau'_{ip}(0)$ calculated from the concentration-dependent data in figure 5.7, which yields values 0.46–3.2 V^{-1} with a similar concentration dependence as $\tau''_{op}(0)$ in fair agreement with the experiments. In the discussed experiments using the DC method, the linear dependence is retained up to 0.6 V, although this might be outside the range where this method is valid. From our calculations clear deviations are expected only for larger bias voltages. Using the time-resolved method a flattening of $\tau'_{op}(V)$ is observed for $|V| > 0.2$ V in [141], which is similar to the dependence observed for the IP component and may have similar reasons.

The ST-FMR method determines the torkance $\vec{\tau}'$; thus, the offset $\tau_{op}(0)$ at zero bias cannot be determined by this method. The equilibrium IEC can be investigated by measuring the hysteresis loop e.g. via the magneto-optical Kerr effect. For the barrier thickness considered in this work experiments obtain a small positive coupling and the result in [71] for Fe leads agrees with our value stated above. For thinner barriers the experiments find a strong increase of the IEC; however, different experiments yield very different results [71, 119] (including different signs), which may be attributed to different preparation conditions (leading to oxygen-vacancies, pinholes, etc.).

Eqs. (5.12b) and (5.13b) predict a simple $\sin(\theta)$ dependence of the STT on the relative angle θ between the magnetizations. This corresponds to the lowest-order coupling of the states entering the barrier from the ferromagnetic slabs [120, 121]. It has been shown in experiments [115, 140] and *ab initio* calculations [59] that this dependence is accurately fulfilled for the barrier thickness considered in this work. Since this dependence is a result of the barrier, we expect no deviations due to alloys in the leads and an investigation of the angular dependence is omitted.

6 Conclusions/Outlook

In this work we have investigated various transport properties of coherent magnetic tunnel junctions (MTJ), including tunnel magnetoresistance (TMR) and spin-transfer torque (STT), using advanced *ab initio* methods. The primary focus lies on the impact of different lead materials, i.e. the composition of the $Fe_{1-x}Co_x$ alloys. However, to provide a solid basis for the explanations, we have also discussed the prototypical system with iron leads in great detail, illustrating many important effects, in particular the symmetry/spin filtering in the MgO barrier, which is the central effect in this class of coherent MTJs. Although this system has been extensively studied in the literature, this consistent treatment proves to be very beneficial because of the great sensitivity to details in the computations. On this basis, the observed results can be traced back to the underlying physical effects and contributing states. This discussion greatly benefits from the combination of several advanced techniques including methods for treating alloys (CPA), transport (NEGF), and spatial symmetry (via IRRs). This allows for a profound understanding of the origin of the calculated results like the alloy-composition and bias-voltage dependence of TMR and STT.

The concentration dependence of the TMR at zero bias voltage shows a steep drop from pure Fe and Co to finite concentrations but remains about constant in between. This striking result suggests the assumption that the decrease is related to the disorder induced by alloying. This causes disorder scattering, which interferes with the coherent tunneling. However, the detailed analysis reveals a more complicated interplay of different effects. At small Co concentrations the TMR is mostly controlled by interface resonance states, which increase the conductance for anti-parallel alignment; these are strongly affected by the disorder. For intermediate concentrations this contribution is superseded by two kinds of contributions, which both tunnel via the Δ_1-like complex band in MgO that provides the smallest decay rate. First, there are bulk states which couple efficiently to this complex band and become available via band filling. The second contribution results from the disorder scattering but is very specific to the considered FeCo alloy: the disorder leads to a very strong broadening of the minority $\Delta_1^\downarrow$ band resulting in a finite density of these states at the Fermi-energy. This effect constitutes an interesting interplay between symmetry and disorder. These specific contributions dominate compared to the more general effects of disorder-induced scattering, which creates additional conductance channels between different symmetries and $\vec{k}_\parallel$-points (diffusive transport). Furthermore, the large TMR for pure Co is actually a consequence of the Cu leads and not reproduced with semi-infinite Co leads. Nonetheless, our results demonstrate that (as expected) disorder has a strong impact on the coherent tunneling.

The TMR decreases with the bias voltage for all compositions of the FeCo alloys, but the decrease is much faster for higher Co concentrations. This dependence is explained from the contributing states. In particular, at high Co concentrations the minority $\Delta_1^\downarrow$ states give the dominating contribution and lead to the fast decrease for pure Co. At intermediate concentrations, details in the voltage dependence are smeared out by the alloy broadening leading to a smooth decay.

The STT is discussed separately for the in-plane and out-of-plane component, which are quite different in behavior and physical effect. The in-plane component induces a rotation of the magnetizations in their common plane and can directly change their relative alignment. It is linear at small bias voltages (and vanishes at zero bias) but shows a non-linear and asymmetric deviation at large bias. This deviation becomes more pronounced with increasing Co concentration and even leads to an inversion of the direction of the torque at a high (positive) bias voltage for pure Co. At negative bias it leads to an enhancement of the torque. The in-plane component can be markedly well described by a model in terms of spin currents. Since the latter can be calculated from the conductance channels for the collinear alignments, this allows for an explanation in terms of effects already discussed for the TMR. In particular, the non-linear deviations are mainly caused by the minority $\Delta_1^\downarrow$ contributions. On the other hand, some contributions which affect the TMR via small currents for anti-parallel alignment have no significant impact on the STT, which is governed by the large Δ_1-like contributions. This explains why the in-plane

component at small bias is basically independent of the Co concentration.

Unlike the in-plane component, the out-of-plane component of the STT is usually non-zero at zero bias. It constitutes a coupling between the layers, the interlayer exchange coupling, and leads to a rotation of the magnetizations around each other for non-collinear alignment. For symmetric junctions it is (usually) an even function of the bias voltage. We find that it is negative at zero bias for all concentrations and increases to positive values with the bias voltage. Its (negative) value at zero bias reduces with Co concentration, while the bias dependence becomes narrower.

The yield for the STT in experiments is smaller than the theoretical predictions, i.e. the torque per current is lower than our results and the fundamental maximum value. This is expected and results from loss mechanisms (e.g. scattering) which are not included in the calculations. For the TMR a comparison between calculated and experimental results is more difficult and usually shows a deviation of almost an order of magnitude, even for low-temperature measurements. This notorious deviation is observed in our results, in particular for the pure materials, but also for the alloys the calculated value is considerably larger than typical experimental results. Further, the concentration dependence differs from experimental results, which show a maximum at about 25% Co. This observation might be explained from the available bulk states in the FeCo alloys, however in our calculations this effect is obscured by interface resonance states; the latter in turn might be quenched by interface roughness in the experiments. The common deviation between experimental and calculated TMR values results form a larger conductance for anti-parallel alignment in experiments and has inspired a broad, prolonged investigation. Although many different possible reasons have been proposed and investigated, no clear explanation has been found, among other things because of the multitude of candidates. Since most of the proposed effects are related to structural imperfections in the experimental junction, in order to make progress a systematic and detailed experimental investigation of the structure of 'typical' junctions appears to be called for, with special regard to large-scale reproducibility, device-to-device variability, and dependence on growth conditions and barrier thickness. Such a study might also investigate the interface resonance states and the band alignment. This considerable effort can be justified not only by the direct application of MTJs as magnetic sensors (or in MRAM) but also by the great importance of tunnel contacts in the growing, active field of spintronics. The next step is to systematically include the most relevant effects in theoretical investigations; here, suitable models might be necessary and in particular alloy analogies would be beneficial. Eventually, one might also include inelastic effects to improve agreement at finite temperatures and high bias voltages. The detailed view and profound explanations provided by *ab initio* calculations can help to identify new approaches to improve the spin-currents, TMR, and STT.

A Appendix I

A.1 Abbreviations

ASA Atomic-sphere approximation, appendix A.2

BSF Bloch spectral density, section 3.6

CPA Coherent potential approximation, section 3.1

DFT Density functional theory, section 2.1

GF Green's function, section 2.2

G/TMR Giant/tunnel magnetoresistance, sections 1, 4.2

(g/T)DOS (generalized/Tunneling) Density of states, sections 2.2, 4.2.1

IEC Interlayer exchange coupling, section 5.2

IP/OP In-plane/out-of-plane component of STT, section 5.1

IRR Irreducible representation of a symmetry group, section 2.5

IRS Interface resonance state, section 4.2.2

KKR Korringa-Kohn-Rostoker method, appendix A.2

LLG Landau-Lifshitz-Gilbert equation, section 5

L(S)DA Local-(spin)-density approximation, section 2.1

MTJ Magnetic tunnel junction, section 4.2

MRAM Magnetic random-access memory, section 1

NEGF Non-equilibrium GF, section 2.2

NECPA Non-equilibrium coherent potential approximation, appendix B.2

P/AP Parallel/anti-parallel alignment of the magnetizations in a MTJ, section 4.2

SSA Single-site approximation, section 3.1

ST-FMR Spin-transfer-driven ferromagnetic resonance, section 5.5

STT Spin-transfer torque, section 5.1

VC Vertex correction, section 3.3

VCA Virtual crystal approximation, section 3.1 and appendix A.4

A.2 The Korringa-Kohn-Rostoker (KKR) method

The KKR method was introduced in [A3]. Here, we only repeat the most important expressions for reference. It is necessary to introduce cell-centered coordinates, i.e. a local coordinate system for each atom (or empty sphere), which in turn requires partitioning real space into individual cells. Throughout this work we use the atomic-sphere approximation (ASA), where a spherical volume is assigned to each atom and the potential is assumed to be spherically symmetric inside this region [A3]. A real-space vector $\vec{r}$ inside the domain V_i of atom i is decomposed as

$$\vec{r} = \vec{R}_i + \vec{r}_i = \vec{T}_i + \vec{S}_i + \vec{r}_i, \tag{A.1}$$

where $\vec{R}_i$ is the center of atom i, $\vec{T}_i$ is a lattice vector, and $\vec{S}_i$ is part of the basis.

In the KKR method the real-space one-electron GF is written in the basis of scattering solutions of the atomic potentials. For convenience, we introduce different notations for the KKR-GF [150, A3]

$$\begin{aligned}\langle\vec{r}|G(z)|\vec{r}'\rangle = G(z;\vec{r},\vec{r}') &= G(z;\vec{R}_i+\vec{r}_i,\vec{R}'_j+\vec{r}'_j) = G^{ij}(z;\vec{r}_i,\vec{r}'_j)\\ &= R^i(z;\vec{r}_i)\,g^{ij}(z)\,R^j(z;\vec{r}'_j)^\times + \delta_{ij}\,G^i_{sc}(z;\vec{r}_i,\vec{r}'_i) \qquad \text{(A.2a)}\\ &= Y(\hat{\vec{r}}_i)^T\,\tilde{R}^i(z;r_i)\,g^{ij}(z)\,\tilde{R}^j(z;r'_j)\,Y(\hat{\vec{r}}'_j)^* + \delta_{ij}\,Y(\hat{\vec{r}}_i)^T\,\tilde{G}^i_{sc}(z;r_i,r'_i)\,Y(\hat{\vec{r}}'_i)^*, \qquad \text{(A.2b)}\end{aligned}$$

where G^i_{sc} is the single-scatterer GF

$$\begin{aligned}G^i_{sc}(z;\vec{r}_i,\vec{r}'_i) &= R^i(z;\vec{r}_i)\,H^i(z;\vec{r}'_i)^\times\,\Theta(r'_i-r_i) + H^i(z;\vec{r}_i)\,R^i(z;\vec{r}'_i)^\times\,\Theta(r_i-r'_i) \qquad \text{(A.2c)}\\ &= Y(\hat{\vec{r}}_i)^T\left(\tilde{R}^i(z;r_i)\,\tilde{H}^i(z;r'_i)\,\Theta(r'_i-r_i) + \tilde{H}^i(z;r_i)\,\tilde{R}^i(z;r'_i)\,\Theta(r_i-r'_i)\right)Y(\hat{\vec{r}}'_i)^*. \qquad \text{(A.2d)}\end{aligned}$$

Here, R^i and H^i are the regular and irregular scattering solution for the isolated potential of atom i [150]. $g=\{g^{ij}\}$ is the structural GF and describes contributions from multiple scattering between the atoms. It is obtained by solving the multiple-scattering equation (or algebraic Dyson equation)

$$g = \left(g_0^{-1}-t\right)^{-1}, \qquad \text{(A.3)}$$

where g_0 is the structural GF for the empty system, which describes the free propagation between the atomic sites (free structure constants), and $t=\{\delta_{ij}\,t_i\}$ is the t-matrix [150] and describes the scattering of the atoms. All these quantities are matrices (or vectors) in angular momentum (possibly incl. spin) indices. The KKR method results in a separation of the atomic properties and the crystal structure. Instead of calculating g directly from g_0, one can introduce intermediate systems (e.g. a screened reference system [150]); this possibility is an important advantage of the KKR method.

The derivation of the quantum transport equations in section 2.4 relies on a decomposition of the Hamiltonian into leads, middle region, and their couplings (figure 2.1). To create such a separation in the KKR method, one can introduce artificial, repulsive potential barriers V^l_{dc} between the leads and the middle region, which are added to the Hamiltonian and approximately decouple the different regions [64, 57]. By considering the Dyson equation relating the decoupled and coupled system (i.e. with and without decoupling potential), one can extract an expression for the lead self-energy [A4]

$$\Sigma^{r/a}_l = V^l_{dc}\,G^{r/a}_{dc}\,V^l_{dc}, \qquad \text{(A.4)}$$

where $G^{r/a}_{dc}$ is the GF for the decoupled system. Since $G^{r/a}_{dc}$ decays exponentially in the decoupling barriers, $\Sigma^{r/a}_l$ can be clipped to a thin slab adjacent to lead l (decoupling region). This expression can be translated to the KKR scheme [29, A4]. For the transport equations one obtains expressions in terms of the structural GFs which are analogous to their operator form in section 2.4. For the density of occupied states originating from lead l one obtains (compare eq. (2.8a,2.19))

$$n^n_l(E,\vec{R}_i+\vec{r}_i) = \frac{1}{2\pi}R^{r,i}(E;\vec{r}_i)\,g^{n,ii}_l(E)\,R^{a,i}(E;\vec{r}_i)^\times \quad \text{with} \quad g^n_l = f_l\,g^r\,\gamma_l\,g^a, \qquad \text{(A.5)}$$

which is valid in the part of the middle region where Σ_l is zero. For the transmission (compare eq. (2.22)) one obtains

$$\bar{T}_{l\leftarrow l'} = \mathrm{Tr}\left[\gamma_l\,g^r\,\gamma_{l'}\,g^a\right], \qquad \text{(A.6)}$$

where the trace is over angular momentum indices and sites where $\gamma_{l/l'}$ (or $\Sigma^{r/a}_{l/l'}$) is non-zero. Here, γ_l is the KKR version of Γ_l (eq. (2.18a)); for an explicit expression and a detailed derivation of the formulas above we refer to the literature [64, 57, 1, A4].

$l=0$	$Y_{00}=1$
$l=1$	$Y_{11}^s=y,\ Y_{10}=z,\ Y_{11}^c=x$
$l=2$	$Y_{22}^s=x\,y,\ Y_{21}^s=y\,z,\ Y_{20}=3z^2-1,\ Y_{21}^c=x\,z,\ Y_{22}^c=x^2-y^2$
$l=3$	$Y_{33}^s=3x^2\,y-y^3,\ Y_{32}^s=x\,y\,z,\ Y_{31}^s=y\,(5z^2-1),\ Y_{30}=5z^3-3z$ $Y_{31}^c=x\,(5z^2-1),\ Y_{32}^c=(x^2-y^2)\,z,\ Y_{33}^c=x^3-3x\,y^2$

Table 5: Real spherical harmonics (unnormalized);
$\hat{\vec{r}}=\{x,y,z\}=\{\cos(\phi)\,\sin(\theta),\sin(\phi)\,\sin(\theta),\cos(\theta)\}$ is a point on the unit sphere.

Δ_1	$Y_{00},\ Y_{10},\ Y_{20},\ Y_{30}$
Δ_2	$Y_{22}^c,\ Y_{32}^c$
Δ_2'	$Y_{22}^s,\ Y_{32}^s$
Δ_5	$\{Y_{11}^c,Y_{11}^s\},\ \{Y_{21}^c,Y_{21}^s\},\ \{Y_{31}^c,Y_{31}^s\},\ \{Y_{33}^c,-Y_{33}^s\}$

Table 6: Basis functions for the point group C_{4v} (or $4mm$) for $l\leq 3$ in terms of the real spherical harmonic given in table 5; note that the lowest basis function for Δ_1' has $l=4$.

A.3 Basis functions for C_{4v} and O_h

In order to find all required basis functions for the point group C_{4v}, we start from the basis functions given in table 3 in section 2.5, which were take from [38]. We can easily find higher order polynomials that transform in the same way. These polynomials are then expressed in terms of spherical harmonics. It is always possible to find linear combinations that result in spherical harmonics with the same l. It is convenient to express the basis functions using real spherical harmonics, defined as [20]

$$Y_{lm}^r=\begin{cases} i\left(Y_{lm}-(-1)^m\,Y_{l-m}\right)/\sqrt{2}=Y_{l-m}^s & \text{if} \quad m<0 \\ Y_{l0} & \text{if} \quad m=0 \\ \left((-1)^m\,Y_{lm}+Y_{l-m}\right)/\sqrt{2}=Y_{lm}^c & \text{if} \quad m>m \end{cases}, \tag{A.7}$$

which are also orthonormal. We assume the Condon-Shortley phase convention for Y_{lm}. The real spherical harmonics for $l\leq 3$ are given in table 5. We obtain all basis function for C_{4v} for $l\leq 3$. They are listed in table 6. The basis functions obtained here are in agreement with those given in [20].

For the group O_h describing the full cubic symmetry we proceed analogous. We start from the character table and the basis functions given in [38]. They are reproduced in table 7. For $l\leq 3$ we only need one additional set of basis functions for Γ_{15}. The resulting basis functions are given in table 7. Apart from an arbitrary sign they agree with [20, 3].

A.4 Results – Virtual crystal approximation

The VCA provides an alternative description of substitutional disordered alloys, which however neglects the effects of disorder scattering (see section 3.1). Conversely, we can use the VCA to investigate the effects of band filling without the additional effects of disorder; this is more reliable than simply shifting the Fermi-energy starting from the pure materials. We obtain a straightforward VCA for $Fe_{1-x}Co_x$ alloys by considering a material with the fractional atomic number $Z(x)=26+x$, which is treated self-consistently by DFT. Using this model, we investigate the TMR for MTJs with semi-infinite VCA FeCo leads in the full concentration range. (10 monolayers of FeCo on each side of the barrier are included in the middle region.) The results are summarized in figure A.1; they are similar to the ones in ref. [130]. At low Co concentrations

O_h	1	$3\,C_2$	$6\,C_4$	$3\,\sigma_v$	$6\,\sigma_d$	i	
Γ_1	1	1	1	1	1	1	1
Γ_{12}	2	2	0	2	0	2	$\{x^2-y^2, 3z^2-1\}$
Γ'_{25}	3	-1	-1	-1	1	3	$\{x\,y, y\,z, z\,x\}$
Γ'_2	1	1	-1	-1	1	-1	$x\,y\,z$
Γ_{15}	3	-1	1	1	1	-3	$\{x, y, z\}$
Γ_{25}	3	-1	-1	1	-1	-3	$\{(x^2-y^2)\,z, \ldots\}$

Γ_1	Y_{00}
Γ_{12}	$\{Y^c_{22}, Y_{20}\}$
Γ'_{25}	$\{Y^s_{22}, Y^s_{21}, Y^c_{21}\}$
Γ'_2	Y^s_{32}
Γ_{15}	$\{Y^c_{11}, Y^s_{11}, Y_{10}\},\ \{-s\,Y^c_{31}+c\,Y^c_{33}, -s\,Y^s_{31}-c\,Y^s_{33}, Y_{30}\}$
Γ_{25}	$\{Y^c_{32}, -c\,Y^c_{31}-s\,Y^c_{33}, c\,Y^s_{31}-s\,Y^s_{33}\}$

Table 7: Cubic symmetry group O_h (or $m3m$).
(Top) Character table [38]. We only show the relevant irreducible representations and symmetry elements. The basis functions for Γ_{25} are $\{(x^2-y^2)\,z, x\,(y^2-z^2), y\,(z^2-x^2)\}$.
(Bottom) Basis functions for $l \leq 3$. $c = \sqrt{5/8}$ and $s = \sqrt{3/8}$.

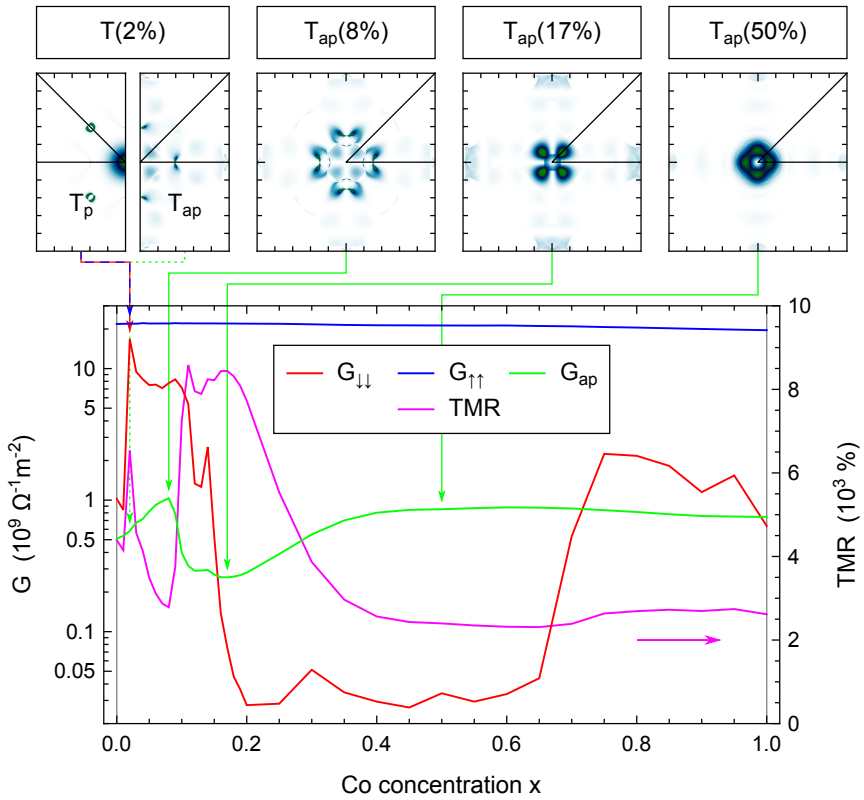

Figure A.1: Conductance and TMR as a function of the Co concentration in a MTJ with $Fe_{1-x}Co_x$ leads and a six-monolayer MgO barrier, where the disordered alloys are treated within VCA. Note the different scales for G and TMR. Additionally, the $\vec{k}_\parallel$-resolved transmission is shown for selected concentrations and conductance channels.

the results agree well with those obtained by simply shifting the Fermi-energy in a MTJ with pure iron leads (section 4.2.4, figure 4.12) and the discussion is analogous.

At low Co concentrations the TMR shows a quite complicated concentration dependence. It shows an abrupt increase between zero and 2%, which is caused by the IRS directly above the Fermi-energy along the $\bar{\Sigma}$ line for Fe (figure 4.11). This gives a large contribution to $G_{\downarrow\downarrow}$ but is largely blocked for G_{ap}. However, the IRS contributes to G_{ap} along the $\bar{\Delta}$-line, which leads to a subsequent increase in G_{ap} up to ca. 8% Co and consequently a decrease in the TMR. For higher concentrations the IRS no longer contributes and G_{ap} decreases, which leads to a very large TMR. The states available at the Fermi-energy couple only weakly to the Δ_1-like complex band in MgO along the $\bar{\Sigma}$-line leading to a small transmission. At higher concentrations new states become available around $\bar{\Gamma}$ (already visible for 17%), which couple more efficiently along the $\bar{\Delta}$-line and lead to an increase in G_{ap}; consequently, the TMR decreases. The new contributions saturate and the TMR remains roughly constant at around 2500% for $x \gtrsim 40\%$.

This dependence is quite different from the one predicted by the CPA (figure 4.16 in section 4.4). The TMR for both pure materials is smaller than the CPA result; in particular, it does not show an increase towards pure Co. This difference is a result of the additional Cu leads, which were included in the CPA calculations. More interestingly, the large maximum around 15% Co is not observed in the CPA results. As explained in section 4.4 the AP conductance in this concentration range is dominated by contributions from IRSs (figure 4.19), which are already below the Fermi-energy in the VCA description. Thus, the maximum is not observed due to the disorder broadening of the IRS, which shows the importance of both: the IRSs and the effects of disorder. Finally, the increase in G_{ap} after the minimum is much weaker than the one observed in the energy-dependent transmission for pure iron leads (figure 4.12). This shows that simply shifting the Fermi-energy in pure materials is not a good approximation for larger concentrations even compared to the VCA.

A.5 Numerical parameters and convergence

The various *ab initio* calculations presented in this work involve several numerical parameters, which have to be carefully chosen. Most of these parameters were introduced in [A3] and are briefly summarized below.

- Energy integration:

  Complex energy contour: For equilibrium quantities the energy integration over the valence bands along the real axis is deformed into a contour in the complex energy plane using analytic properties of the retarded GF. The contour consists of three lines sampled by N_{E1}, N_{E2}, N_{E3} energy points via Gaussian quadrature (see [A3]). Additionally, the GF has to be calculated at the Matsubara poles [150] of the cut-off Fermi-function [A3]; thus the total number of energy points is $N_{E1} + N_{E2} + N_{E3} + N_P$. Note that the $\vec{k}$-mesh is chosen individually for the complex energy points depending on the imaginary part $\operatorname{Im} z$, thus the computational costs can be very different.

  Real energy integration: Non-equilibrium quantities must be calculated on the real energy axis and integrated over the energy window created by a bias voltage; only a very small imaginary part is added to facilitate convergence of the other parameters. In this case a simple trapezoidal rule with N_{E2} points is used for the numerical integration.

  Imaginary part of the complex energy $\operatorname{Im} z$: For the complex contour integration the maximum imaginary part is given by $\operatorname{Im} z = 2\pi\, k_B\, T\, N_P$, where T is the 'temperature' in the cut-off Fermi-function; for the integration (or energy-resolved quantities) along the real axis the small imaginary part (artificial broadening) is parameterized by $\operatorname{Im} z = \pi\, k_B\, T$.

- $\vec{k}$-point mesh: For DFT self-consistent calculations the (maximal) $\vec{k}$-mesh contains $N_{\vec{k}} = N_{k1}\, N_{k2}\, N_{k3}$ $\vec{k}$-points, which are equally spaced along the reciprocal lattice vectors. However, for the long supercells (along z) containing a tunnel barrier considered in this work we can choose $N_{k3} = N_{kz} = 1$. For transport calculations the $\vec{k}_{\parallel}$-mesh contains $N_{k1}\, N_{k2} =$

	energy-mesh		$\vec{k}$-mesh	ref. sys.	CPA
	N_E	T, N_P, Im z	$N_{kx}\,N_{ky}$	R_{cl}, N_{cl}	$\epsilon_{\tilde{x}}$
DFT sc.	$2+20+2+10$	800 K, 10, 0.318 Ry	24^2	$1.5\,a_{\mathrm{Fe}}$, 27	10^{-3}
STT equ.	$5+70+5+40$	100 K, 40, 0.159 Ry	30^2	$2.8\,a_{\mathrm{Fe}}$, 169	10^{-6}
non-equ.	$N_{E2}(V)$	0.2 K, – , 3.98 μRy	200^2	$2.8\,a_{\mathrm{Fe}}$, 169	10^{-6}

Table 8: Convergence parameters which were used in the main calculations: DFT self-consistent calculations (DFT sc.) to obtain the potentials, the equilibrium part of STT calculations (STT equ.) and the non-equilibrium (non-equ.) calculations. The same parameters were used in the non-equilibrium calculations for STT and TMR.
For equilibrium calculations N_E is given as $N_{E1}+N_{E2}+N_{E3}+N_P$; for non-equilibrium calculations N_E is given as a function of the bias voltage $N_{E2}(V) = e\,|V|/1$ mRy $+\,1$, which means that the bias window $[\mu_L, \mu_R]$ is sampled in steps of 1 mRy.
N_{cl} is given for the bcc metals, it is up to three times larger inside the MgO barrier.
In STT equ. calculations the full $\vec{k}_{\parallel}$-mesh is used for all energy points regardless of Im z.
For the decimation technique a block size of four layers is used.
The given values are lower bounds, higher values have been used in some calculations (see also text).
1 Ry = 13.6 eV

$N_{kx}\,N_{ky}$ points, while the z-direction is treated by decimation technique [150]. The $\vec{k}$-mesh is reduced to the irreducible Brillouin zone making use of space group symmetries (section 2.5).

- Reference system: A system with repulsive muffin-tin step potentials with a hight of 8 Ry placed on all atomic and empty-sphere sites is chosen as reference system. The reference GF is calculated in real space [150] on spherical clusters with cut-off radius R_{cl} containing N_{cl} sites.

- Coherent potential approximation: The CPA introduces an additional convergence parameter $\epsilon_{\tilde{x}}$, which determines if the CPA self-consistent iteration is converged. For comparability to [A3] this is defined by[19] $\sum_i \|\tilde{x}^i\|/N_{CPA} < \epsilon_{\tilde{x}}$ where $\tilde{x}^i = (\bar{t}^i)^{-1}\,\bar{x}^i\,(\bar{t}^i)^{-1}$ and $\|\cdot\|$ is the Frobenius matrix norm. Additionally, a similar convergence parameter occurs if the vertex corrections are calculated iteratively; however, since this iteration is outside the $\vec{k}$-integration and computationally cheap it can be easily converged and need not be discussed.

Throughout this work we use an angular momentum cut-off $l_{max} = 3$ in all calculations resulting in 16×16 matrices (32×32 for non-collinear) per atom. All calculations are spin-polarized and non-relativistic. Convergence of DFT self-consistent calculations with CPA alloys has been thoroughly discussed in [A3]. These calculations add relatively little to the total computational costs and transport results are rather insensitive to details of the potentials. Thus, the relevant parameters need not be discussed in detail and are stated in table 8. Note that the oxygen 2s states in MgO are treated as semi-core states (i.e. included in the valence bands), thus the energy integration extends over a range of almost 2 Ry. The lattice structure is described in section 4.2; empty spheres are placed inside the MgO barrier and at the FeCo/MgO interfaces and are excluded in determining the 'muffin-tin zero' energy.

The convergence parameters for transport calculations are more difficult to choose, since computational costs can quickly increase prohibitively. The values used in this work are summarized in table 8. The choice of the small imaginary part of the energy Im z is particularly intricate. Unlike in the complex contour integration for equilibrium quantities where it is mathematically justified, this artificial broadening poses an unphysical approximation (see section 4.2.4) and

[19] $\tilde{x}$ is the excess scattering matrix in Z-J basis, see section 3.2.

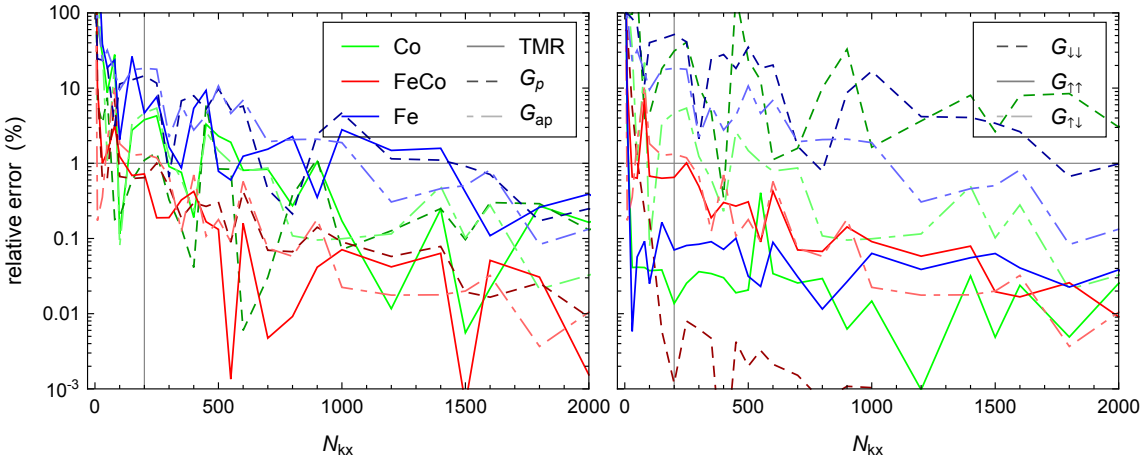

Figure A.2: Convergence of TMR (in linear response) and conductances (at E_F) with respect to the $\vec{k}_\parallel$-mesh in a MTJ with 20-monolayer ferromagnetic slabs of Co, $Fe_{0.5}Co_{0.5}$, and Fe. The figures show the relative deviation $|x(N_{kx}) - x_\infty|/x_\infty$ from a reference value x_∞ obtained for a much larger N_{kx} outside the plot range.
(Left) TMR and total conductance for P and AP alignment.
(Right) Conductances in the different channels; note that $G_{\uparrow\downarrow} = G_{\downarrow\uparrow}$.

should be chosen as small as possible. On the other hand, a larger $\mathrm{Im}\, z$ strongly facilitates the convergence of most other parameters. Here, we adopt the choice from [56], where it has been shown that this value provides a sensible compromise between accuracy and computational costs for comparable transport calculations. For a given $\mathrm{Im}\, z$ the cluster radius R_{cl} for the reference system should be chosen carefully, since an insufficient value can lead to unphysical results [A3]. It was shown in [56] that the present value is sufficient for MTJs with Fe leads; we have verified that this also holds for the FeCo leads considered in this work. Since the CPA self-consistent calculations are computationally relatively cheap, the value for $\epsilon_{\tilde{x}}$ has been chosen well beyond the necessary accuracy.

The $\vec{k}_\parallel$-mesh convergence depends strongly on the particular system and quantity under consideration, which makes a systematic study quite complex. We discuss this for conductance and TMR in more detail. Clearly, the convergence of the conductance depends on the structure of the $\vec{k}_\parallel$-resolved transmission (e.g. figure 4.21 in section 4.4). Sharply localized contributions e.g. from IRSs or quantum-well states are difficult to sample, whereas the broad Δ_1-peak is easily converged. This is illustrated in figure A.2, which shows the convergence of TMR and conductance in different channels for MTJs with Co, $Fe_{0.5}Co_{0.5}$, and Fe leads. The figure is slightly crowded but still gives a clear picture. It also shows that the convergence is superimposed by large fluctuations, which impede the convergence study. The convergence is quite similar for TMR, P, and AP conductance but different for the three lead materials. For the FeCo alloy it is much faster than for the pure materials, since disorder broadening smears out the structure in the $\vec{k}_\parallel$-resolved transmission. For Fe leads it is slowest because of sharply localized contributions from the IRS. This is more clearly visible in the separate spin channels: for the pure materials $G_{\uparrow\uparrow}$ converges rapidly but $G_{\downarrow\downarrow}$ shows a very slow convergence. Only because $G_{\downarrow\downarrow}$ is much smaller than $G_{\uparrow\uparrow}$, their sum G_p converges more quickly. Interestingly, for the FeCo alloy it is opposite: $G_{\downarrow\downarrow}$ converges rapidly because of the very strong broadening, whereas $G_{\uparrow\uparrow}$ converges rather slowly, which is related to the convergence of the effective medium[20].

This study shows that the chosen $\vec{k}_\parallel$-mesh ($N_{kx} = 200$, table 8) is sufficient to converge the results for $Fe_{0.5}Co_{0.5}$ to a residual error of about 2% and we have verified that it is sufficient for all considered finite concentrations (10% – 90% Co). However, this 'standard' $\vec{k}_\parallel$-mesh is too

[20] Because of the strong scattering, the effective medium for the minority spin converges slower with the CPA iterations than the majority one but more quickly with the $\vec{k}$-mesh.

coarse for the pure materials. The data in figure A.2 is obtained for a fixed thickness of the ferromagnetic slabs; yet in most calculations we apply a thickness averaging, which could reduce the error. Additionally, for finite bias voltages the energy integration induces an averaging over N_E energy points. Assuming independent random errors, the combination of both could reduce the error by a factor of about $0.4/\sqrt{N_E - 1}$ (taking into account the weights). To improve the convergence for pure lead materials we use increased parameters for TMR calculations from the standard values in table 8: at zero bias we use a denser $\vec{k}_\parallel$-mesh with $N_{\vec{k}} = 1000^2$ points and for small bias voltages we increase the E-mesh to at least $N_E \geq 20$ points (with the standard $\vec{k}_\parallel$-mesh).

As shown in section 5 the STT is mostly determined by Δ_1-like contributions. Since the latter are easily converged, the standard parameters are sufficient for STT calculations for all considered materials.

B Appendix II – Coherent potential approximation

B.1 Restricted averages via projection operators

In this section we need to introduce the occupation variables η, which are sometimes used to describe the alloy configuration [150, 73]

$$\eta_\alpha^i = \begin{cases} 1 & \text{if site } i \text{ is occupied by species } \alpha \\ 0 & \text{else.} \end{cases} \tag{B.1}$$

They obey some useful identities

$$\sum_\alpha \eta_\alpha^i = 1 \qquad \eta_\alpha^i \, \eta_\beta^i = \delta_{\alpha\beta} \, \eta_\alpha^i \tag{B.2a}$$

$$\langle \eta_\alpha^i \rangle = c_\alpha^i \qquad \langle \eta_\alpha^i \, \eta_\beta^j \rangle = \delta_{ij} \, \delta_{\alpha\beta} \, c_\alpha^i + \left(1 - \delta_{ij}\right) c_\alpha^i \, c_\beta^j \qquad \dots \tag{B.2b}$$

With the occupation variables we can write configuration-dependent quantities, e.g. the t-matrix, as

$$t^i = \sum_\alpha \eta_\alpha^i \, t_\alpha^i. \tag{B.3}$$

Because of eq. (B.2a), η_α^i may be used as a projection operator, since $\eta_\alpha^i \, (\cdot)$ vanishes for any expression $(\cdot)$ if site i is not occupied with α. In particular, we can write the restricted averages as

$$\langle (\cdot) \rangle = \sum_\alpha \langle \eta_\alpha^i (\cdot) \rangle = \sum_\alpha c_\alpha^i \langle (\cdot) \rangle_{i=\alpha}, \quad \text{i.e.} \quad \langle (\cdot) \rangle_{i=\alpha} = \frac{1}{c_\alpha^i} \langle \eta_\alpha^i (\cdot) \rangle. \tag{B.4}$$

One may recognize the form of a conditional expectation value. For the special case of a binary alloy with components A and B ($c_B^i = 1 - c_A^i$), η_A^i and η_B^i may be written as [73]

$$\begin{aligned} \eta_A^i &= \left(t_B^i - t_A^i\right)^{-1} \left(t_B^i - t^i\right) \\ \eta_B^i &= \left(t_A^i - t_B^i\right)^{-1} \left(t_A^i - t^i\right). \end{aligned} \tag{B.5}$$

Note that these are on-site matrices; they can be trivially extended to the full scalar matrices via $\eta_A^i \otimes 1$, etc. By taking the average of the Dyson equation (3.4) we find $\langle t \, g \rangle = \bar{t} \, \bar{g}$ and in particular $\langle t^i \, g^{ii} \rangle = \bar{t}^i \, \bar{g}^{ii}$. In agreement with the SSA we can disregard indirect effects of η_α^i via the other sites (see section 3.4). With this we can evaluate the restricted averages of the GF [73]

$$\begin{aligned} \bar{g}_A^{ii} = \langle g^{ii} \rangle_{i=A} &= \frac{1}{c_A^i} \langle \eta_A^i \, g^{ii} \rangle &&= \frac{1}{c_A^i} \left(t_B^i - t_A^i\right)^{-1} \left(t_B^i - \bar{t}^i\right) \bar{g}^{ii} \\ \bar{g}_B^{ii} = \langle g^{ii} \rangle_{i=B} &= \frac{1}{c_B^i} \langle \eta_B^i \, g^{ii} \rangle &&= \frac{1}{c_B^i} \left(t_A^i - t_B^i\right)^{-1} \left(t_A^i - \bar{t}^i\right) \bar{g}^{ii}. \end{aligned} \tag{B.6}$$

Similarly, we can calculate the restricted averages for the two-particle expression $g^< = g \, A \, g$. We suppress the energy arguments and the operator $((\cdot)_A)$ index (see section 3.3). Using the Dyson equation and the definition of the vertex corrections (eq. (3.14)) we find

$$\begin{aligned} \langle g^< \rangle = \langle g \, A \, g \rangle &= \Big\langle \left(\bar{g} + \bar{g} \, (t - \bar{t}) \, g\right) A \, g \Big\rangle \\ &= \bar{g} \, A \, \bar{g} + \bar{g} \, \langle t \, g \, A \, g \rangle - \bar{g} \, \bar{t} \, \langle g \, A \, g \rangle = \bar{g} \, (A + \Omega) \, \bar{g} = \bar{g}^< \\ \Rightarrow \quad \langle t \, g^< \rangle = \langle t \, g \, A \, g \rangle &= \bar{t} \, \langle g \, A \, g \rangle + \Omega \, \bar{g} = \bar{t} \, \bar{g}^< + \Omega \, \bar{g} \end{aligned}$$

and in particular $\langle t^i \, g^{<,ii} \rangle = \bar{t}^i \, \bar{g}^{<,ii} + \Omega^i \, \bar{g}^{ii}$. With this we obtain the restricted averages [73]

$$\begin{aligned} \bar{g}_A^{<,ii} = \frac{1}{c_A^i} \langle \eta_A^i \, g^{<,ii} \rangle &= \frac{1}{c_A^i} \left(t_B^i - t_A^i\right)^{-1} \Big(\left(t_B^i - \bar{t}^i\right) \bar{g}^{<,ii} - \Omega^i \, \bar{g}^{ii} \Big) \\ \bar{g}_B^{<,ii} = \frac{1}{c_B^i} \langle \eta_B^i \, g^{<,ii} \rangle &= \frac{1}{c_B^i} \left(t_A^i - t_B^i\right)^{-1} \Big(\left(t_A^i - \bar{t}^i\right) \bar{g}^{<,ii} - \Omega^i \, \bar{g}^{ii} \Big). \end{aligned} \tag{B.7}$$

Before we show the equivalence of these expressions to the general formulas, we derive some useful identities for the case of a binary alloy. In this case, the CPA condition

$$0 = \langle x^i \rangle = c_A^i \, x_A^i + \left(1 - c_A^i\right) x_B^i \quad \Leftrightarrow \quad x_B^i = \frac{c_A^i}{c_A^i - 1} x_A^i \tag{B.8}$$

can be solved for $\bar{g}^{ii}$

$$\bar{g}^{ii} = \left(1 - c_A^i\right) \left(t_A^i - \bar{t}^i\right)^{-1} + c_A^i \left(t_B^i - \bar{t}^i\right)^{-1}. \tag{B.9}$$

Inserting this in the general expressions in section 3.2 we obtain

$$D_A^i = \frac{1}{c_A^i} \left(t_B^i - t_A^i\right)^{-1} \left(t_B^i - \bar{t}^i\right) \qquad \tilde{D}_A^i = \frac{1}{c_A^i} \left(t_B^i - \bar{t}^i\right) \left(t_B^i - t_A^i\right)^{-1} \tag{B.10a}$$

$$D_B^i = \frac{1}{c_B^i} \left(t_A^i - t_B^i\right)^{-1} \left(t_A^i - \bar{t}^i\right) \qquad \tilde{D}_A^i = \frac{1}{c_B^i} \left(t_A^i - \bar{t}^i\right) \left(t_A^i - t_B^i\right)^{-1} \tag{B.10b}$$

$$x_A^i = \frac{1}{c_A^i} \left(\left(t_A^i - \bar{t}^i\right)^{-1} - \left(t_B^i - \bar{t}^i\right)^{-1} \right)^{-1} \qquad = \frac{c_A^i - 1}{c_A^i} \, x_B^i. \tag{B.10c}$$

Using eq. (B.10a) and (B.10b) we obtain $\bar{g}_\alpha^{ii}$ in eq. (B.6) directly from the general expression eq. (3.10b). To verify the two-particle expression we first note that for a binary alloy the equation for the vertex corrections (eq. (3.16c)) can be written (using eq. (B.8))

$$\Omega^n = - \, x_A^n \left(\bar{g}^{<,nn} - \bar{g}^{nn} \, \Omega^n \, \bar{g}^{nn}\right) x_B^n = - \, x_B^n \left(\bar{g}^{<,nn} - \bar{g}^{nn} \, \Omega^n \, \bar{g}^{nn}\right) x_A^n. \tag{B.11}$$

We rewrite the general expression for $\bar{g}_\alpha^{<,ii}$ eq. (3.34) (using eq. (3.10c))

$$\bar{g}_\alpha^{<,ii} = D_\alpha^i \left(\bar{g}^{<,ii} - \bar{g}^{ii} \, \Omega^i \, \bar{g}^{ii}\right) \tilde{D}_\alpha^i = D_\alpha^i \left(\bar{g}^{<,ii} - \bar{g}^{ii} \, \Omega^i \, \bar{g}^{ii} + \left(\bar{g}^{<,ii} - \bar{g}^{ii} \, \Omega^i \, \bar{g}^{ii}\right) x_\alpha^i \, \bar{g}^{ii} \right).$$

The last term is replaced using eq. (B.11)

$$\begin{aligned} \bar{g}_A^{<,ii} &= D_A^i \, \bar{g}^{<,ii} - D_A^i \left(\bar{g}^{ii} + (x_B^i)^{-1}\right) \Omega^i \, \bar{g}^{ii} \\ \bar{g}_B^{<,ii} &= D_B^i \, \bar{g}^{<,ii} - D_B^i \left(\bar{g}^{ii} + (x_A^i)^{-1}\right) \Omega^i \, \bar{g}^{ii} \end{aligned}$$

and using eqs. (B.9) and (B.10) we obtain eq. (B.7). Thus, we find that for binary alloys the restricted averages obtained via projection operators are equivalent to the general expressions. However, this method is difficult to generalize to more components. The generalization for the projection operator e.g. for three components would be

$$\eta_A^i = \frac{t_B^i - t^i}{t_B^i - t_A^i} \, \frac{t_C^i - t^i}{t_C^i - t_A^i}, \qquad \text{etc.} \tag{B.12}$$

This leads to terms like $\langle t^2 \, g \rangle$, which are difficult to calculate.

B.2 Non-equilibrium coherent potential approximation (NECPA)

In this section we discuss an alternative approach for combining NEGF and CPA. The idea is to introduce the CPA directly for 'contour' GFs rather than taking the alloy average of the Keldysh equation as in sections 3.3 and 3.5. This has been proposed in [70, 155]. Our derivation is similar to [155]; however, we use a Keldysh matrix notation [75, 88] rather than working with actual contour quantities [75, 55], which simplifies the derivation.

We start by combining the Dyson equation for the retarded and advanced GF (2.13) and the Keldysh equation (2.14a) (exemplary for the lesser GF) to a single matrix equation

$$\begin{aligned} g_1^c &= g_0^c + g_0^c \, \Sigma^c \, g_1^c \qquad \text{where} \\ g_i^c &= \begin{pmatrix} 0 & g_i^a \\ g_i^r & g_i^< \end{pmatrix} \quad \text{and} \quad \Sigma^c = \begin{pmatrix} \Sigma^< & \Sigma^r \\ \Sigma^a & 0 \end{pmatrix}. \end{aligned} \tag{B.13}$$

We call the combined matrix g^c contour GF[21]. The advantage of the contour GF is that we can treat retarded, advanced, and lesser component simultaneously. Note that the retarded and advanced component do not mix with the others. The Dyson equation for the contour GF has the same form as the one for the retarded GF. Thus, we can repeat the derivation of the CPA from section 3.2 in terms of the contour GF (in place of the retarded GF), which automatically leads to the correct lesser component (i.e. including vertex corrections).

As an example we calculate $g^<$ using the explicit form of the Dyson equation (2.13)

$$g_1^< = \left[\left((g_0^c)^{-1} - \Sigma^c\right)^{-1}\right]^< = g_1^r \left((g_0^r)^{-1} g_0^< (g_0^a)^{-1} + \Sigma^<\right) g_1^a \tag{B.14a}$$

$$= \left(1 + g_1^r \Sigma^r\right) g_0^< \left(1 + \Sigma^a g_1^a\right) + g_1^r \Sigma^< g_1^a, \tag{B.14b}$$

where we used the inverse of contour quantities

$$(g^c)^{-1} = \begin{pmatrix} -(g^r)^{-1} g^< (g^a)^{-1} & (g^r)^{-1} \\ (g^a)^{-1} & 0 \end{pmatrix} \qquad \text{and} \tag{B.15a}$$

$$(\Sigma^c)^{-1} = \begin{pmatrix} 0 & (\Sigma^a)^{-1} \\ (\Sigma^r)^{-1} & -(\Sigma^r)^{-1} \Sigma^< (\Sigma^a)^{-1} \end{pmatrix} \tag{B.15b}$$

and the usual Dyson equation (2.13).

To derive the NECPA we treat the non-equilibrium condition (i.e. the self-energy of the leads Σ^c) and the disorder simultaneously. We obtain the Dyson equation for the effective medium contour GF (compare eq. (3.3))

$$\bar{g}^c = \left((g_0^c)^{-1} - \Sigma^c - \bar{t}^c\right)^{-1} \quad \text{where} \quad \bar{t}^c = \begin{pmatrix} \Omega^< & \bar{t}^r \\ \bar{t}^a & 0 \end{pmatrix}. \tag{B.16}$$

Using $g_0^< = 0$ we find $\bar{g}^< = \left[\bar{g}^c\right]^< = \bar{g}^r \Sigma^< \bar{g}^a + \bar{g}^r \Omega^< \bar{g}^a$, which is identical to eq. (3.14) if $\Omega^<$ are the vertex corrections from section 3.3 associated with the operator $\Sigma^<$. To obtain the CPA condition we repeat the steps leading to eq. (3.9) for the contour quantities and find

$$\langle x^{c,i} \rangle = \sum_\alpha c_\alpha^i \, x_\alpha^{c,i} = 0 \qquad \text{where} \tag{B.17}$$

$$x_\alpha^{c,i} = \left(\left(t_\alpha^{c,i} - \bar{t}^{c,i}\right)^{-1} - \bar{g}^{c,ii}\right)^{-1} \quad \text{and} \quad t_\alpha^{c,i} = \begin{pmatrix} 0 & t_\alpha^{r,i} \\ t_\alpha^{a,i} & 0 \end{pmatrix}.$$

We evaluate the lesser component and obtain

$$x_\alpha^{<,i} = \left[x_\alpha^{c,i}\right]^< = x_\alpha^{r,i} \left(\bar{g}^{<,ii} - (\Delta t_\alpha^{r,i})^{-1} \, \Omega^{<,i} \, (\Delta t_\alpha^{a,i})^{-1}\right) x_\alpha^{a,i} = x_\alpha^{r,i} \, \bar{g}^{<,ii} \, x_\alpha^{a,i} - \tilde{D}_\alpha^{r,i} \, \Omega^{<,i} \, D_\alpha^{a,i}. \tag{B.18}$$

Using $\sum_\alpha c_\alpha^i \, \tilde{D}_\alpha^{r,i} \, (\cdot) \, D_\alpha^{a,i} = (\cdot) + \sum_\alpha c_\alpha^i \, x_\alpha^{r,i} \, \bar{g}^{r,ii} \, (\cdot) \, \bar{g}^{a,ii} \, x_\alpha^{a,i}$ analogous to eq. (3.36), we obtain eq. (3.16c) (with $A \to \Sigma^<$ and $\Omega_A \to \Omega^<$). Thus, we find that the NECPA is equivalent to CPA plus vertex corrections.

We can also obtain the (one-site) component GF using eq. (3.20) or (3.10b)

$$\begin{aligned} g_\alpha^{<,i} &= \left[\bar{g}^{c,ii} + \bar{g}^{c,ii} \, x_\alpha^{c,i} \, \bar{g}^{c,ii}\right]^< = \left[\left((\bar{g}^{c,ii})^{-1} - \Delta t_\alpha^{c,i}\right)^{-1}\right]^< \\ &= \left((\bar{g}^{r,ii})^{-1} - \Delta t_\alpha^{r,i}\right)^{-1} \left((\bar{g}^{r,ii})^{-1} \, \bar{g}^{<,ii} \, (\bar{g}^{a,ii})^{-1} - \Omega^{<,i}\right) \left((\bar{g}^{a,ii})^{-1} - \Delta t_\alpha^{a,i}\right)^{-1} \\ &= D_\alpha^{r,i} \left(\bar{g}^{<,ii} - \bar{g}^{r,ii} \, \Omega^{<,i} \, \bar{g}^{a,ii}\right) \tilde{D}_\alpha^{a,i}, \end{aligned} \tag{B.19}$$

which is equivalent to eq. (3.34). Comparing this derivation with the one in section 3.5 reveals some advantage of the NECPA approach. Finally we consider the two-site component GF. We start from eq. (3.27)

$$g_{\alpha\beta}^{c,ij} = D_\alpha^{c,i} \, \bar{g}^{c,ij} \, \tilde{D}_\beta^{c,j}, \tag{B.20a}$$

[21] These matrices represent contour quantities [88, 75, 55]; we can perform calculations 'on the contour' by using these matrices and then obtain the usual (real-time) GFs by taking the corresponding element of the matrix (analytic continuation).

where we define and simplify

$$D_\alpha^{c,i} = \left(\begin{smallmatrix}1&0\\0&1\end{smallmatrix}\right) + \bar{g}^{c,ii}\, x_\alpha^{c,i} = \begin{pmatrix} D_\alpha^{a,i} & 0 \\ D_\alpha^{<,i} & D_\alpha^{r,i} \end{pmatrix} \quad \text{with} \tag{B.20b}$$

$$D_\alpha^{<,i} = \bar{g}^{r,ii}\, x_\alpha^{<,i} + \bar{g}^{<,ii}\, x_\alpha^{a,i} = D_\alpha^{r,i} \left(\bar{g}^{<,ii}\, x_\alpha^{a,i} - \bar{g}^{r,ii}\, \Omega^{<,i}\, D_\alpha^{a,i}\right)$$

$$\tilde{D}_\beta^{c,j} = \left(\begin{smallmatrix}1&0\\0&1\end{smallmatrix}\right) + x_\beta^{c,j}\, \bar{g}^{c,jj} = \begin{pmatrix} \tilde{D}_\beta^{r,j} & \tilde{D}_\beta^{<,j} \\ 0 & \tilde{D}_\beta^{a,j} \end{pmatrix} \quad \text{with} \tag{B.20c}$$

$$\tilde{D}_\beta^{<,j} = x_\beta^{r,j}\, \bar{g}^{<,jj} + x_\beta^{<,j}\, \bar{g}^{a,jj} = \left(x_\beta^{r,j}\, \bar{g}^{<,jj} - \tilde{D}_\beta^{r,j}\, \Omega^{<,j}\, \bar{g}^{a,jj}\right) \tilde{D}_\beta^{a,j}.$$

Note that we could use D^c to obtain $g_\alpha^{<,i} = \left[D_\alpha^{c,i}\, \bar{g}^{c,ii}\right]^<$ or $g_\alpha^{<,i} = \left[\bar{g}^{c,ii}\, \tilde{D}_\alpha^{c,i}\right]^<$, which yield eq. (3.34). With this we obtain

$$g_{\alpha\beta}^{<,ij} = \left[D_\alpha^{c,i}\, \bar{g}^{c,ij}\, \tilde{D}_\beta^{c,j}\right]^< = D_\alpha^{r,i}\, \bar{g}^{r,ij}\, \tilde{D}_\beta^{<,j} + D_\alpha^{r,i}\, \bar{g}^{<,ij}\, \tilde{D}_\beta^{a,j} + D_\alpha^{<,i}\, \bar{g}^{a,ij}\, \tilde{D}_\beta^{a,j}. \tag{B.21}$$

B.3 Numerical verification

The necessary equations to calculate equilibrium and non-equilibrium quantities within the CPA are derived analytically in section 3 and appendix B.2. In addition, in this section we aim to verify these equations and their implementation by numerical test calculations. One possibility is to compare CPA results to supercell calculations (section 3.1). In [A3] this has been used to verify the CPA results for various equilibrium properties of FeCo alloys. In section 4.1 we use this method to check the (equilibrium) BSF via unfolding of the supercell density. Here, we aim to verify the non-equilibrium quantities (transmission function, density, and BSF) and in particular the vertex corrections.

We start by comparing the CPA result for the transmission to supercell calculations. We consider a test system consisting of a 10-monolayer slab of FeCo alloy, which is embedded in copper. As usual, we use the bcc lattice structure of iron for all metals and the materials are stacked along the [001] direction. For this system we calculate the transmission in z-direction for several concentrations (in steps of 1/8) using a 4×4 in-plane supercell (16 atoms per layer). The concentration is enforced individually in each layer and we use CPA potentials to construct the supercells. We use numerical parameters similar to table 8 but with an increased broadening of $\mathrm{Im}\, z = 20\,\mu\mathrm{Ry}$ and an appropriately reduced $\vec{k}_\parallel$-mesh for the supercells [A4]. The transmission is calculated for 10 random configurations for each concentration and compared to the CPA result; this is shown in figure B.1. We find an excellent agreement between both methods. Despite the large supercells (160 alloy sites) the supercell results show a considerable spread around the CPA result. Figure B.1 also shows CPA results neglecting vertex corrections. The contribution of the vertex corrections is particularly large for the spin-down channel as a result of the strong disorder scattering for this spin, which is also visible in several other calculations in this work.

A similar test could be used to verify the non-equilibrium density (eq. (2.8a)). However, a more convenient and more accurate test is to compare the non-equilibrium to the equilibrium density: if all states in all leads are fully occupied ($f_l = 1$ for all leads l and energies), the non-equilibrium density should equal the equilibrium one ($n^L + n^R = n^{eq}$). Effectively, this amounts to testing eqs. (2.1a) and (2.14c), i.e. $i\left(G^r - G^a\right) = A = G^r\, \Gamma\, G^a$. An example is shown in figure B.1 for an $Fe_{0.3}Co_{0.7}$ slab. This shows a very good agreement; the small remaining difference is a consequence of the finite artificial broadening. The figure also shows results where the vertex corrections are calculated iteratively with different numbers of iterations. This shows a quick and steady convergence; for 100 iterations the result is basically indistinguishable from the one via inversion (not shown). These results are obtained with the alternative method for restricted averages introduced in appendix B.1, which is applicable only for binary alloys. We have checked that the general method derived in section 3.5 (and appendix B.2) yields the same result. We also use this test for the component-resolved density. This is shown in figure B.2 for a similar system with an $Fe_{0.5}Co_{0.5}$ slab. Here, we additionally assume an interdiffusion of 25% between the layers adjacent to the interfaces. This corresponds to the thickness averaging used in most calculations in this work (see section 4.3) and introduces a ternary FeCoCu alloy,

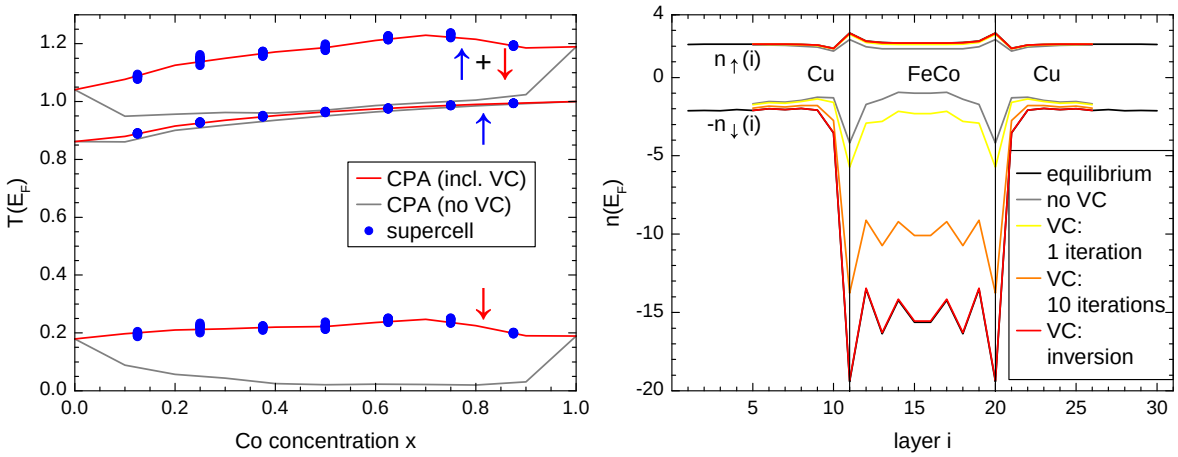

Figure B.1: (Left) Transmission through a thin slab of $Fe_{1-x}Co_x$ alloy embedded in Cu at the Fermi-energy as a function of the Co concentration for both spins separately and their sum; we compare results calculated for supercells, with CPA, and with CPA neglecting vertex corrections (VC).
(Right) Layer-resolved density of states for an $Fe_{0.3}Co_{0.7}$ slab at the Fermi-energy for both spins calculated via equilibrium and non-equilibrium GFs. For the non-equilibrium density we show several stages in the calculation of the vertex corrections. Note that the non-equilibrium density cannot be calculated in the outermost layers (decoupling region). Modified from [A4].

which requires application of the general restricted averages. Finally, we test the non-equilibrium BSF; this is shown in figure B.2 for the same system for the $\bar{\Gamma}$-point. This figure also shows the symmetry-resolved density, i.e. resolved with respect to the IRRs of the symmetry group for this $\vec{k}_{\parallel}$-point. Note that Cu has only Δ_1-states at $\bar{\Gamma}$ at the Fermi-energy; thus the other symmetries are restricted to the vicinity of the alloy slab, where, moreover, the majority spin has only very small densities for these states. We have also checked the density resolved with respect to other quantum numbers, e.g. the angular momentum indices, and for the full two-dimensional Brillouin zone; in all cases we find the same perfect agreement observed in the figures.

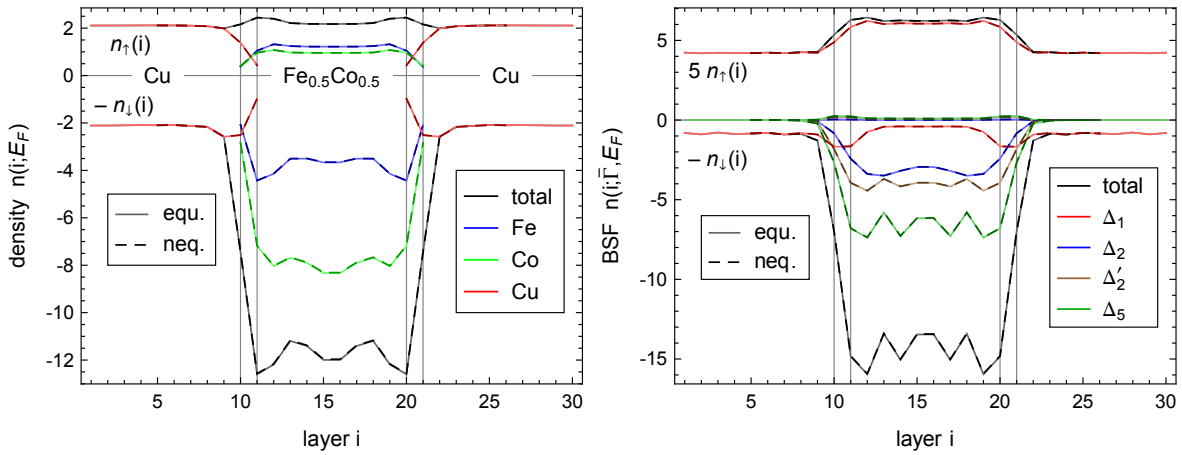

Figure B.2: (Left) Component-resolved and total density of states at the Fermi-energy in an $Fe_{0.5}Co_{0.5}$ slab embedded in Cu with a thin interdiffusion layer; for each density the equilibrium (equ.) and non-equilibrium (neq.) result is shown.
(Right) Symmetry-resolved and total Bloch spectral density in the same system at the Fermi-energy and $\bar{\Gamma}$-point. Note the scaling of the majority density.

References

[1] Steven Achilles, Michael Czerner, Jürgen Henk, Ingrid Mertig, and Christian Heiliger. Nonequilibrium Green's functions and Korringa-Kohn-Rostoker method: Open planar junctions. *Physical Review B*, 88(12):125411, 2013.

[2] S. L. Altmann and C. J. Bradley. Lattice harmonics II. Hexagonal close-packed lattice. *Reviews of Modern Physics*, 37(1):33–45, 1965.

[3] S. L. Altmann and A. P. Cracknell. Lattice harmonics I. Cubic groups. *Reviews of Modern Physics*, 37(1):19–32, 1965.

[4] S. Andrieu, F. Bonell, T. Hauet, F. Montaigne, L. Calmels, E. Snoeck, P. Lefevre, and F. Bertran. Magnetotransport in MgO-based magnetic tunnel junctions grown by molecular beam epitaxy. *Journal of Applied Physics*, 115(17):172610, 2014.

[5] V. P. Antropov, M. I. Katsnelson, B. N. Harmon, M. van Schilfgaarde, and D. Kusnezov. Spin dynamics in magnets: Equation of motion and finite temperature effects. *Physical Review B*, 54(2):1019–1035, 1996.

[6] David Awschalom and Nitin Samarth. Spintronics without magnetism. *Physics*, 2:50, 2009.

[7] David D. Awschalom and Michael E. Flatté. Challenges for semiconductor spintronics. *Nature Physics*, 3(3):153–159, 2007.

[8] David D. Awschalom, Daniel Loss, and Nitin Samarth, editors. *Semiconductor Spintronics and Quantum Computation*. Springer, Berlin Heidelberg, 2002.

[9] S. D. Bader and S. S. P. Parkin. Spintronics. *Annual Review of Condensed Matter Physics*, 1(1):71–88, 2010.

[10] Supriyo Bandyopadhyay and Marc Cahay. *Introduction to Spintronics*. CRC Press, March 2008.

[11] Supriyo Bandyopadhyay and Marc Cahay. Electron spin for classical information processing: a brief survey of spin-based logic devices, gates and circuits. *Nanotechnology*, 20(41):412001, 2009.

[12] Gerrit E. W. Bauer, Eiji Saitoh, and Bart J. van Wees. Spin caloritronics. *Nature Materials*, 11(5):391–399, 2012.

[13] K. D. Belashchenko, Julian Velev, and Evgeny Y. Tsymbal. Effect of interface states on spin-dependent tunneling in Fe/MgO/Fe tunnel junctions. *Physical Review B*, 72(14):140404, 2005.

[14] B. Belhadji and L. Calmels. Bulk electron states with Δ symmetry in disordered Fe-based alloys for magnetic tunnel junctions. *Physical Review B*, 83(9):092401, 2011.

[15] Gustav Bihlmayer. Non-collinear magnetism: Exchange parameter and T_C. In Johannes Grotendorst, Stefan Blügel, and Dominik Marx, editors, *Computational Nanoscience: Do it Yourself*, volume 31 of *NIC Series*, pages 447–467. John von Neumann Institute for Computing, Jülich, 2006.

[16] Lapo Bogani and Wolfgang Wernsdorfer. Molecular spintronics using single-molecule magnets. *Nature Materials*, 7(3):179–186, 2008.

[17] F. Bonell, S. Andrieu, A. M. Bataille, C. Tiusan, and G. Lengaigne. Consequences of interfacial Fe-O bonding and disorder in epitaxial Fe/MgO/Fe(001) magnetic tunnel junctions. *Physical Review B*, 79(22):224405, 2009.

[18] F. Bonell, S. Andrieu, C. Tiusan, F. Montaigne, E. Snoeck, B. Belhadji, L. Calmels, F. Bertran, P. Le Fèvre, and A. Taleb-Ibrahimi. Influence of misfit dislocations on the magnetoresistance of MgO-based epitaxial magnetic tunnel junctions. *Physical Review B*, 82(9):092405, 2010.

[19] F. Bonell, T. Hauet, S. Andrieu, F. Bertran, P. Le Fèvre, L. Calmels, A. Tejeda, F. Montaigne, B. Warot-Fonrose, B. Belhadji, A. Nicolaou, and A. Taleb-Ibrahimi. Spin-polarized electron tunneling in bcc FeCo/MgO/FeCo(001) magnetic tunnel junctions. *Physical Review Letters*, 108(17):176602, 2012.

[20] Christopher John Bradley and Arthur P. Cracknell. *The Mathematical Theory of Symmetry in Solids: Representation Theory for Point Groups and Space Groups.* Clarendon Press Oxford, 1972.

[21] Arne Brataas, Andrew D. Kent, and Hideo Ohno. Current-induced torques in magnetic materials. *Nature Materials*, 11(5):372–381, 2012.

[22] William Fuller Brown. *Micromagnetics.* Number 18. Interscience Publishers New York, 1963.

[23] P. Bruno. Theory of intrinsic and thermally induced interlayer magnetic coupling between ferromagnetic films separated by an insulating layer. *Physical Review B*, 49(18):13231–13234, 1994.

[24] W. H. Butler. Theory of electronic transport in random alloys: Korringa-Kohn-Rostoker coherent-potential approximation. *Physical Review B*, 31(6):3260–77, 1985.

[25] W. H. Butler, X.-G. Zhang, T. C. Schulthess, and J. M. MacLaren. Spin-dependent tunneling conductance of Fe|MgO|Fe sandwiches. *Physical Review B*, 63(5):054416, 2001.

[26] K. Carva, I. Turek, J. Kudrnovskỳ, and O. Bengone. Disordered magnetic multilayers: Electron transport within the coherent potential approximation. *Physical Review B*, 73(14):144421, 2006.

[27] Claude Chappert, Albert Fert, and Frédéric Nguyen Van Dau. The emergence of spin electronics in data storage. *Nature Materials*, 6(11):813–823, 2007.

[28] Michael Czerner. *Beiträge zur Theorie des Elektronentransports in Systemen mit nichtkollinearer magnetischer Ordnung.* PhD thesis, Martin-Luther-Universität Halle-Wittenberg, 2009.

[29] Michael Czerner. private communication, 2010.

[30] Michael Czerner, Michael Bachmann, and Christian Heiliger. Spin caloritronics in magnetic tunnel junctions: *Ab initio* studies. *Physical Review B*, 83(13):132405, 2011.

[31] S. Datta. *Electronic Transport in Mesoscopic Systems.* Cambridge: Cambridge University Press, 1999.

[32] Supriyo Datta and Biswajit Das. Electronic analog of the electro-optic modulator. *Applied Physics Letters*, 56(7):665–667, 1990.

[33] John H. Davies, Selman Hershfield, Per Hyldgaard, and John W. Wilkins. Current and rate equation for resonant tunneling. *Physical Review B*, 47(8):4603–4618, 1993.

[34] Massimiliano Di Ventra. *Electrical transport in nanoscale systems.* Cambridge University Press, Cambridge, August 2008.

[35] Zhitao Diao, Zhanjie Li, Shengyuang Wang, Yunfei Ding, Alex Panchula, Eugene Chen, Lien-Chang Wang, and Yiming Huai. Spin-transfer torque switching in magnetic tunnel junctions and spin-transfer torque random access memory. *Journal of Physics: Condensed Matter*, 19(16):165209, 2007.

[36] A. Díaz-Ortiz, R. Drautz, M. Fähnle, H. Dosch, and J. M. Sanchez. Structure and magnetism in bcc-based iron-cobalt alloys. *Physical Review B*, 73(22):224208, 2006.

[37] Tomasz Dietl and Hideo Ohno. Dilute ferromagnetic semiconductors: Physics and spintronic structures. *Reviews of Modern Physics*, 86(1):187–251, 2014.

[38] Mildred S. Dresselhaus, Gene Dresselhaus, and Ado Jorio. *Group Theory.* Springer, 2008.

[39] Volker Drewello, J. Schmalhorst, Andy Thomas, and Günter Reiss. Evidence for strong magnon contribution to the TMR temperature dependence in MgO based tunnel junctions. *Physical Review B*, 77(1):014440, 2008.

[40] H. Ebert, S. Mankovsky, K. Chadova, S. Polesya, J. Minár, and D. Ködderitzsch. Calculating linear-response functions for finite temperatures on the basis of the alloy analogy model. *Physical Review B*, 91(16):165132, 2015.

[41] Hubert Ebert, Sergiy Mankovsky, Diemo Ködderitzsch, and P. J. Kelly. Ab initio calculation of the Gilbert damping parameter via the linear response formalism. *Physical Review Letters*, 107(6):066603, 2011.

[42] Eleftherios N. Economou. *Green's Functions in Quantum Physics.* Number 7 in Springer Series in Solid-State Sciences. Springer, 3 edition, 2006.

[43] Jaroslav Fabian, Alex Matos-Abiague, Christian Ertler, Peter Stano, and Igor Žutić. Semiconductor spintronics. *Acta Physica Slovaca. Reviews and Tutorials*, 57(4-5):565–907, 2007.

[44] Sergey V. Faleev, Oleg N. Mryasov, and Mark van Schilfgaarde. Effect of correlations on electronic structure and transport across (001) Fe/MgO/Fe junctions. *Physical Review B*, 85(17):174433, 2012.

[45] J. S. Faulkner and G. M. Stocks. Calculating properties with the coherent-potential approximation. *Physical Review B*, 21(8):3222–3244, 1980.

[46] Claudia Felser and Gerhard H. Fecher, editors. *Spintronics: From Materials to Devices.* Springer Netherlands, 2013.

[47] Albert Fert. Nobel lecture: Origin, development, and future of spintronics. *Reviews of Modern Physics*, 80(4):1517–1530, 2008.

[48] T. L. Gilbert. A Lagrangian formulation of the gyromagnetic equation of the magnetization field. *Physical Review*, 100:1243, 1955.

[49] B. Ginatempo and J. B. Staunton. The electronic structure of disordered alloys containing heavy elements — an improved calculational method illustrated by a study of a copper-gold alloy. *Journal of Physics F: Metal Physics*, 18(8):1827–1837, 1988.

[50] Rudolf Gross and Achim Marx. *Vorlesungsskript zur Vorlesung "Spinelektronik"*. Walther-Meißner-Institut, Garching, 2004.

[51] Theo Hahn, editor. *International Tables for Crystallography*, volume A: Space-Group Symmetry. Springer, 5 edition, 2005.

[52] P. M. Haney, D. Waldron, R. A. Duine, A. S. Núñez, H. Guo, and A. H. MacDonald. Current-induced order parameter dynamics: Microscopic theory applied to Co/Cu/Co spin valves. *Physical Review B*, 76(2):024404, 2007.

[53] Paul M. Haney, Christian Heiliger, and Mark D. Stiles. Bias dependence of magnetic exchange interactions: Application to interlayer exchange coupling in spin valves. *Physical Review B*, 79(5):054405, 2009.

[54] Moosa Hatami, Gerrit E. W. Bauer, Qinfang Zhang, and Paul J. Kelly. Thermal spin-transfer torque in magnetoelectronic devices. *Physical Review Letters*, 99(6):066603, 2007.

[55] H. Haug and A.-P. Jauho. *Quantum Kinetics in Transport and Optics of Semiconductors*, volume 123 of *Springer Series in Solid-State Sciences*. Berlin, Heidelberg: Springer, 2008.

[56] Christian Heiliger. *Elektronentransport durch planare Tunnelkontakte: Eine* ab initio *Beschreibung*. PhD thesis, Martin-Luther-Universität Halle-Wittenberg, 2007.

[57] Christian Heiliger, Michael Czerner, Bogdan Yu. Yavorsky, Ingrid Mertig, and Mark D. Stiles. Implementation of a nonequilibrium Greens function method to calculate spin-transfer torque. *Journal of Applied Physics*, 103(7):07A709, 2008.

[58] Christian Heiliger, Martin Gradhand, Peter Zahn, and Ingrid Mertig. Tunneling magnetoresistance on the subnanometer scale. *Physical Review Letters*, 99(6):066804, 2007.

[59] Christian Heiliger and M. D. Stiles. *Ab Initio* studies of the spin-transfer torque in magnetic tunnel junctions. *Physical Review Letters*, 100(18):186805, 2008.

[60] Christian Heiliger, Peter Zahn, and Ingrid Mertig. Microscopic origin of magnetoresistance. *Materials Today*, 9(11):46–54, 2006.

[61] Christian Heiliger, Peter Zahn, Bogdan Yu. Yavorsky, and Ingrid Mertig. Influence of the interface structure on the bias dependence of tunneling magnetoresistance. *Physical Review B*, 72(18):180406, 2005.

[62] Christian Heiliger, Peter Zahn, Bogdan Yu. Yavorsky, and Ingrid Mertig. Interface structure and bias dependence of Fe/MgO/Fe tunnel junctions: *Ab initio* calculations. *Physical Review B*, 73(21):214441, 2006.

[63] Christian Heiliger, Peter Zahn, Bogdan Yu. Yavorsky, and Ingrid Mertig. Thickness dependence of the tunneling current in the coherent limit of transport. *Physical Review B*, 77(22):224407, 2008.

[64] J. Henk, A. Ernst, K. K. Saha, and P. Bruno. Computing conductances of tunnel junctions by the Korringa-Kohn-Rostoker method: formulation and test of a Green function approach. *Journal of Physics: Condensed Matter*, 18(8):2601, 2006.

[65] Atsufumi Hirohata and Koki Takanashi. Future perspectives for spintronic devices. *Journal of Physics D: Applied Physics*, 47(19):193001, 2014.

[66] P. Hohenberg and W. Kohn. Inhomogeneous electron gas. *Physical Review*, 136(3B):B864–B871, 1964.

[67] Ron Jansen. Silicon spintronics. *Nature Materials*, 11(5):400–408, 2012.

[68] Michel Jullière. Tunneling between ferromagnetic films. *Physics Letters A*, 54(3):225–226, 1975.

[69] Tomas Jungwirth, Jörg Wunderlich, and Kamil Olejník. Spin hall effect devices. *Nature Materials*, 11(5):382–390, 2012.

[70] Alan V. Kalitsov, Mairbek G. Chshiev, and Julian P. Velev. Nonequilibrium coherent potential approximation for electron transport. *Physical Review B*, 85(23):235111, 2012.

[71] T. Katayama, S. Yuasa, Julian Velev, M. Ye. Zhuravlev, Sitaram S. Jaswal, and Evgeny Y. Tsymbal. Interlayer exchange coupling in Fe/MgO/Fe magnetic tunnel junctions. *Applied Physics Letters*, 89(11):112503–112503, 2006.

[72] Takayuki Kawahara, Kenchi Ito, Riichiro Takemura, and Hideo Ohno. Spin-transfer torque RAM technology: Review and prospect. *Microelectronics Reliability*, 52(4):613–627, 2012.

[73] Youqi Ke. *Theory of Non-equilibrium Vertex Correction*. PhD thesis, McGill University, Montréal, 2010.

[74] Youqi Ke, Ke Xia, and Hong Guo. Disorder scattering in magnetic tunnel junctions: Theory of nonequilibrium vertex correction. *Physical Review Letters*, 100(16):166805, 2008.

[75] L. V. Keldysh. Diagram technique for nonequilibrium processes. *Soviet Physics — Journal of Experimental and Theoretical Physics (JETP)*, 20(4):1018–26, 1965.

[76] Furrukh S. Khan, John H. Davies, and John W. Wilkins. Quantum transport equations for high electric fields. *Physical Review B*, 36(5):2578–2597, 1987.

[77] S. I. Kiselev, J. C. Sankey, I. N. Krivorotov, N. C. Emley, R. J. Schoelkopf, R. A. Buhrman, and D. C. Ralph. Microwave oscillations of a nanomagnet driven by a spin-polarized current. *Nature*, 425(6956):380–383, 2003.

[78] W. Kohn. Nobel lecture: Electronic structure of matter-wave functions and density functionals. *Reviews of Modern Physics*, 71(5):1253–1266, 1999.

[79] W. Kohn and L. J. Sham. Self-consistent equations including exchange and correlation effects. *Physical Review*, 140(4A):A1133–A1138, 1965.

[80] M. Krawczyk and D. Grundler. Review and prospects of magnonic crystals and devices with reprogrammable band structure. *Journal of Physics: Condensed Matter*, 26(12):123202, 2014.

[81] V. V. Kruglyak, S. O. Demokritov, and D. Grundler. Magnonics. *Journal of Physics D: Applied Physics*, 43(26):264001, 2010.

[82] Hitoshi Kubota, Akio Fukushima, Kay Yakushiji, Taro Nagahama, Shinji Yuasa, Koji Ando, Hiroki Maehara, Yoshinori Nagamine, Koji Tsunekawa, David D. Djayaprawira, Naoki Watanabe, and Yoshishige Suzuki. Quantitative measurement of voltage dependence of spin-transfer torque in MgO-based magnetic tunnel junctions. *Nature Physics*, 4(1):37–41, 2008.

[83] Lew Dawidowitsch Landau and Evgeny Mikhailovich Lifshitz. On the theory of the dispersion of magnetic permeability in ferromagnetic bodies. *Phys. Z. Sowjetunion*, 8(153):101–114, 1935.

[84] Y. M. Lee, J. Hayakawa, S. Ikeda, F. Matsukura, and H. Ohno. Effect of electrode composition on the tunnel magnetoresistance of pseudo-spin-valve magnetic tunnel junction with a MgO tunnel barrier. *Applied Physics Letters*, 90(21):212507–212507, 2007.

[85] Benjamin Lenk, Henning Ulrichs, Fabian Garbs, and Markus Münzenberg. The building blocks of magnonics. *Physics Reports*, 507(4):107–136, 2011.

[86] M. Levy. Electron densities in search of Hamiltonians. *Physical Review A*, 26(3):1200–1208, 1982.

[87] A. I. Liechtenstein, M. I. Katsnelson, V. P. Antropov, and V. A. Gubanov. Local spin density functional approach to the theory of exchange interactions in ferromagnetic metals and alloys. *Journal of Magnetism and Magnetic Materials*, 67(1):65–74, 1987.

[88] Evgenii Mikhailovich Lifshitz, Lev Petrovich Pitaevskii, and Lev Davidovich Landau. *Physikalische Kinetik*. Number 10 in Lehrbuch der theoretischen Physik; L. D. Landau, E. M. Lifschitz. Akademie-Verlag Berlin, 1990.

[89] Nicolas Locatelli, Vincent Cros, and Julie Grollier. Spin-torque building blocks. *Nature Materials*, 13(1):11–20, 2014.

[90] Y. Lu, H.-X. Yang, C. Tiusan, M. Hehn, M. Chshiev, A. Duluard, B. Kierren, G. Lengaigne, D. Lacour, C. Bellouard, and F. Montaigne. Spin-orbit coupling effect by minority interface resonance states in single-crystal magnetic tunnel junctions. *Physical Review B*, 86(18):184420, 2012.

[91] A. H. MacDonald, P. Schiffer, and N. Samarth. Ferromagnetic semiconductors: moving beyond (Ga,Mn)As. *Nature Materials*, 4(3):195–202, 2005.

[92] X. Marti, I. Fina, C. Frontera, Jian Liu, P. Wadley, Qing He, R. J. Paull, J. D. Clarkson, J. Kudrnovský, I. Turek, J. Kuneš, D. Yi, J.-H. Chu, C. T. Nelson, L. You, E. Arenholz, S. Salahuddin, J. Fontcuberta, T. Jungwirth, and R. Ramesh. Room-temperature antiferromagnetic memory resistor. *Nature Materials*, 13(4):367–374, 2014.

[93] Richard M. Martin. *Electronic Structure: Basic Theory and Practical Methods*. Cambridge University Press, 2008.

[94] J. Mathon and A. Umerski. Theory of tunneling magnetoresistance of an epitaxial Fe/MgO/Fe(001) junction. *Physical Review B*, 63(22):220403, 2001.

[95] Ph. Mavropoulos, N. Papanikolaou, and P. H. Dederichs. Complex band structure and tunneling through ferromagnet/insulator/ferromagnet junctions. *Physical Review Letters*, 85(5):1088–1091, 2000.

[96] Yigal Meir and Ned S. Wingreen. Landauer formula for the current through an interacting electron region. *Physical Review Letters*, 68(16):2512, 1992.

[97] I. Mertig, E. Mrosan, and P. Ziesche. *Multiple scattering theory of point defects in metals: Electronic properties*. Teubner, 1987.

[98] H. L. Meyerheim, R. Popescu, N. Jedrecy, M. Vedpathak, M. Sauvage-Simkin, R. Pinchaux, B. Heinrich, and J. Kirschner. Surface x-ray diffraction analysis of the MgO/Fe(001) interface: Evidence for an FeO layer. *Physical Review B*, 65(14):144433, 2002.

[99] H. L. Meyerheim, R. Popescu, J. Kirschner, N. Jedrecy, M. Sauvage-Simkin, B. Heinrich, and R. Pinchaux. Geometrical and compositional structure at metal-oxide interfaces: MgO on Fe(001). *Physical Review Letters*, 87(7):076102, 2001.

[100] G. X. Miao, Young Ju Park, J. S. Moodera, M. Seibt, G. Eilers, and M. Münzenberg. Disturbance of tunneling coherence by oxygen vacancy in epitaxial Fe/MgO/Fe magnetic tunnel junctions. *Physical Review Letters*, 100(24):246803, 2008.

[101] Robert Mills, L. J. Gray, and Theodore Kaplan. Analytic approximation for random muffin-tin alloys. *Physical Review B*, 27(6):3252, 1983.

[102] Wolfgang Nolting. *Grundkurs Theoretische Physik 7: Viel-Teilchen-Theorie*. Number 7 in Grundkurs Theoretische Physik. Springer, 2005.

[103] Alvaro S. Núñez and Allan H. MacDonald. Theory of spin transfer phenomena in magnetic metals and semiconductors. *Solid State Communications*, 139(1):31–34, 2006.

[104] S. S. P. Parkin, K. P. Roche, M. G. Samant, P. M. Rice, R. B. Beyers, R. E. Scheuerlein, E. J. OSullivan, S. L. Brown, J. Bucchigano, D. W. Abraham, Yu Lu, M. Rooks, P. L. Trouilloud, R. A. Wanner, and W. J. Gallagher. Exchange-biased magnetic tunnel junctions and application to nonvolatile magnetic random access memory. *Journal of Applied Physics*, 85(8):5828–5833, 1999.

[105] Stuart S. P. Parkin, Christian Kaiser, Alex Panchula, Philip M. Rice, Brian Hughes, Mahesh Samant, and See-Hun Yang. Giant tunnelling magnetoresistance at room temperature with MgO (100) tunnel barriers. *Nature Materials*, 3(12):862–867, 2004.

[106] Robert G. Parr and Weitao Yang. *Density-Functional Theory of Atoms and Molecules*. International Series of Monographs on Chemistry 16. Oxford University Press, 1994.

[107] Dmytro Pesin and Allan H. MacDonald. Spintronics and pseudospintronics in graphene and topological insulators. *Nature Materials*, 11(5):409–416, 2012.

[108] L. Plucinski, Yuan Zhao, C. M. Schneider, B. Sinkovic, and E. Vescovo. Surface electronic structure of ferromagnetic Fe(001). *Physical Review B*, 80(18):184430, 2009.

[109] Voicu Popescu and Alex Zunger. Effective band structure of random alloys. *Physical Review Letters*, 104(23):236403, 2010.

[110] D. C. Ralph and Mark D. Stiles. Spin transfer torques. *Journal of Magnetism and Magnetic Materials*, 320(7):1190–1216, 2008.

[111] E. I. Rashba. Theory of electrical spin injection: Tunnel contacts as a solution of the conductivity mismatch problem. *Physical Review B*, 62(24):R16267–R16270, 2000.

[112] Alexandre R. Rocha, Victor M. Garcia-Suarez, Steve W. Bailey, Colin J. Lambert, Jaime Ferrer, and Stefano Sanvito. Towards molecular spintronics. *Nature Materials*, 4(4):335–339, 2005.

[113] Ivan Rungger, Oleg Mryasov, and Stefano Sanvito. Resonant electronic states and I-V curves of Fe/MgO/Fe(100) tunnel junctions. *Physical Review B*, 79(9):094414, 2009.

[114] Sayeef Salahuddin, Deepanjan Datta, and Supriyo Datta. Spin transfer torque as a non-conservative pseudo-field. *arXiv preprint*, page arXiv:0811.3472, 2008.

[115] Jack C. Sankey, Yong-Tao Cui, Jonathan Z. Sun, John C. Slonczewski, Robert A. Buhrman, and Daniel C. Ralph. Measurement of the spin-transfer-torque vector in magnetic tunnel junctions. *Nature Physics*, 4(1):67–71, 2008.

[116] F. Schleicher, U. Halisdemir, D. Lacour, M. Gallart, S. Boukari, G. Schmerber, V. Davesne, P. Panissod, D. Halley, H. Majjad, Y. Henry, B. Leconte, A. Boulard, D. Spor, N. Beyer, C. Kieber, E. Sternitzky, O. Cregut, M. Ziegler, F. Montaigne, E. Beaurepaire, P. Gilliot, M. Hehn, and M. Bowen. Localized states in advanced dielectrics from the vantage of spin- and symmetry-polarized tunnelling across MgO. *Nature Communications*, 5:4547, 2014.

[117] G. Schmidt, D. Ferrand, L. W. Molenkamp, A. T. Filip, and B. J. Van Wees. Fundamental obstacle for electrical spin injection from a ferromagnetic metal into a diffusive semiconductor. *Physical Review B*, 62(8):R4790–R4793, 2000.

[118] Jairo Sinova and Igor Žutić. New moves of the spintronics tango. *Nature Materials*, 11(5):368–371, 2012.

[119] Witold Skowroński, Tomasz Stobiecki, Jerzy Wrona, Karsten Rott, Andy Thomas, Günter Reiss, and Sebastiaan van Dijken. Interlayer exchange coupling and current induced magnetization switching in magnetic tunnel junctions with MgO wedge barrier. *Journal of Applied Physics*, 107(9):093917, 2010.

[120] J. C. Slonczewski. Conductance and exchange coupling of two ferromagnets separated by a tunneling barrier. *Physical Review B*, 39(10):6995, 1989.

[121] J. C. Slonczewski. Currents, torques, and polarization factors in magnetic tunnel junctions. *Physical Review B*, 71(2):024411, 2005.

[122] J. C. Slonczewski and J. Z. Sun. Theory of voltage-driven current and torque in magnetic tunnel junctions. *Journal of Magnetism and Magnetic Materials*, 310(2):169–175, 2007.

[123] John Slonczewski. Theory of spin-polarized current and spin-transfer torque in magnetic multilayers. In Helmut Kronmüller and Stuart Parkin, editors, *Spintronics and Magnetoelectronics*, volume 5 of *Handbook of Magnetism and Advanced Magnetic Materials*. John Wiley & Sons, Ltd, 2007.

[124] John C. Slonczewski. Current-driven excitation of magnetic multilayers. *Journal of Magnetism and Magnetic Materials*, 159(1):L1–L7, 1996.

[125] Robert L. Stamps, Stephan Breitkreutz, Johan Åkerman, Andrii V. Chumak, YoshiChika Otani, Gerrit E. W. Bauer, Jan-Ulrich Thiele, Martin Bowen, Sara A. Majetich, Mathias Kläui, Ioan Lucian Prejbeanu, Bernard Dieny, Nora M. Dempsey, and Burkard Hillebrands. The 2014 magnetism roadmap. *Journal of Physics D: Applied Physics*, 47(33):333001, 2014.

[126] Harold T. Stokes, Branton J. Campbell, and Dorian M. Hatch. FINDSYM version 4.2, ISOTROPY Software Suite. Software, 2014.

[127] Harold T. Stokes and Dorian M. Hatch. FINDSYM: program for identifying the space-group symmetry of a crystal. *Journal of Applied Crystallography*, 38(1):237–238, 2005.

[128] Ioannis Theodonis, Nicholas Kioussis, Alan Kalitsov, Mairbek Chshiev, and W. H. Butler. Anomalous bias dependence of spin torque in magnetic tunnel junctions. *Physical Review Letters*, 97(23):237205, 2006.

[129] William Thomson. On the electro-dynamic qualities of metals:–Effects of magnetization on the electric conductivity of nickel and of iron. *Proceedings of the Royal Society of London*, 8:546–550, 1856-1857.

[130] J. P. Trinastic, Yan Wang, and Hai-Ping Cheng. First-principles study of Co concentration and interfacial resonance states in $Fe_{1-x}Co_x$ magnetic tunnel junctions. *Physical Review B*, 88(10):104408, 2013.

[131] Evgeny Y. Tsymbal and Igor Žutić, editors. *Handbook of Spin Transport and Magnetism*. CRC press, 2011.

[132] A. A. Tulapurkar, Y. Suzuki, A. Fukushima, H. Kubota, H. Maehara, K. Tsunekawa, D. D. Djayaprawira, N. Watanabe, and S. Yuasa. Spin-torque diode effect in magnetic tunnel junctions. *Nature*, 438(7066):339–342, 2005.

[133] Julian P. Velev, Kirill D. Belashchenko, and Evgeny Y. Tsymbal. Comment on "destructive effect of disorder and bias voltage on interface resonance transmission in symmetric tunnel junctions". *Physical Review Letters*, 96(11):119601, 2006.

[134] B. Velický. Theory of electronic transport in disordered binary alloys: Coherent-potential approximation. *Physical Review*, 184(3):614–627, 1969.

[135] B. Velický, S. Kirkpatrick, and H. Ehrenreich. Single-site approximations in the electronic theory of simple binary alloys. *Physical Review*, 175(3):747–66, 1968.

[136] Ulf von Barth and Lars Hedin. A local exchange-correlation potential for the spin polarized case: I. *Journal of Physics C: Solid State Physics*, 5(13):1629, 1972.

[137] S. H. Vosko, L. Wilk, and M. Nusair. Accurate spin-dependent electron liquid correlation energies for local spin density calculations: a critical analysis. *Canadian Journal of Physics*, 58(8):1200–1211, 1980.

[138] Igor Žutić, Jaroslav Fabian, and S. Das Sarma. Spintronics: Fundamentals and applications. *Reviews of Modern Physics*, 76(2):323–410, 2004.

[139] Marvin Walter, Jakob Walowski, Vladyslav Zbarsky, Markus Münzenberg, Markus Schäfers, Daniel Ebke, Günter Reiss, Andy Thomas, Patrick Peretzki, Michael Seibt, Jagadeesh S. Moodera, Michael Czerner, Michael Bachmann, and Christian Heiliger. Seebeck effect in magnetic tunnel junctions. *Nature Materials*, 10(10):742–746, 2011.

[140] C. Wang, Y.-T. Cui, J. Z. Sun, J. A. Katine, R. A. Buhrman, and D. C. Ralph. Bias and angular dependence of spin-transfer torque in magnetic tunnel junctions. *Physical Review B*, 79(22):224416, 2009.

[141] Chen Wang, Yong-Tao Cui, Jordan A. Katine, Robert A. Buhrman, and Daniel C. Ralph. Time-resolved measurement of spin-transfer-driven ferromagnetic resonance and spin torque in magnetic tunnel junctions. *Nature Physics*, 7(6):496–501, 2011.

[142] Mark Winter. Webelements.

[143] S. A. Wolf, D. D. Awschalom, R. A. Buhrman, J. M. Daughton, S. von Molnár, M. L. Roukes, A. Yu. Chtchelkanova, and D. M. Treger. Spintronics: A spin-based electronics vision for the future. *Science*, 294(5546):1488–1495, 2001.

[144] D. Wortmann, H. Ishida, and S. Blügel. Ab initio Green-function formulation of the transfer matrix: Application to complex band structures. *Physical Review B*, 65(16):165103, 2002.

[145] B. D. Yu and J.-S. Kim. *Ab initio* study of ultrathin MgO films on Fe(001): Influence of interfacial structures. *Physical Review B*, 73(12):125408, 2006.

[146] S. Yuasa and D. D. Djayaprawira. Giant tunnel magnetoresistance in magnetic tunnel junctions with a crystalline MgO(0 0 1) barrier. *Journal of Physics D: Applied Physics*, 40(21):R337, 2007.

[147] Shinji Yuasa. *Tunneling Magnetoresistance: Experiment (MgO Magnetic Tunnel Junctions)*, chapter 11, pages 217–232. In Tsymbal and Žutić [131], 2011.

[148] Shinji Yuasa, Akio Fukushima, Hitoshi Kubota, Yoshishige Suzuki, and Koji Ando. Giant tunneling magnetoresistance up to 410% at room temperature in fully epitaxial Co/MgO/Co magnetic tunnel junctions with bcc Co(001) electrodes. *Applied Physics Letters*, 89(4):042505, 2006.

[149] Shinji Yuasa, Taro Nagahama, Akio Fukushima, Yoshishige Suzuki, and Koji Ando. Giant room-temperature magnetoresistance in single-crystal Fe/MgO/Fe magnetic tunnel junctions. *Nature Materials*, 3(12):868–871, 2004.

[150] Jan Zabloudil, Robert Hammerling, Laszlo Szunyogh, and Peter Weinberger. *Electron Scattering in Solid Matter: A Theoretical and Computational Treatise*, volume 147 of *Springer Series in Solid-State Sciences*. Springer, 2005.

[151] P.-J. Zermatten, G. Gaudin, G. Maris, M. Miron, A. Schuhl, C. Tiusan, F. Greullet, and M. Hehn. Experimental evidence of interface resonance states in single-crystal magnetic tunnel junctions. *Physical Review B*, 78(3):033301, 2008.

[152] X.-G. Zhang and W. H. Butler. Large magnetoresistance in bcc Co/MgO/Co and FeCo/MgO/FeCo tunnel junctions. *Physical Review B*, 70(17):172407, 2004.

[153] X.-G. Zhang, W. H. Butler, and Amrit Bandyopadhyay. Effects of the iron-oxide layer in Fe-FeO-MgO-Fe tunneling junctions. *Physical Review B*, 68(9):092402, 2003.

[154] Jian-Gang Jimmy Zhu and Chando Park. Magnetic tunnel junctions. *Materials Today*, 9(11):36–45, 2006.

[155] Yu Zhu, Lei Liu, and Hong Guo. Quantum transport theory with nonequilibrium coherent potentials. *Physical Review B*, 88(20):205415, 2013.

Publications

[A1] Alexander Böhnke, Marius Milnikel, Marvin von der Ehe, Christian Franz, Vladyslav Zbarsky, Michael Czerner, Karsten Rott, Andy Thomas, Christian Heiliger, Günter Reiss, and Markus Münzenberg. On/off switching of bit readout in bias-enhanced tunnel magneto-Seebeck effect. *Scientific Reports*, 5:8945, 2015.

[A2] F. Boschini, M. Mansurova, G. Mussler, J. Kampmeier, D. Grützmacher, L. Braun, F. Katmis, J. S. Moodera, C. Dallera, E. Carpene, C. Franz, M. Czerner, C. Heiliger, T. Kampfrath, and M. Münzenberg. Coherent ultrafast spin-dynamics probed in three dimensional topological insulators. *Scientific Reports*, 5:15304, 2015.

[A3] Christian Franz. *Ab initio* description of ferromagnetic alloys within the coherent potential approximation. Diploma thesis, Justus-Liebig-Universität Gießen, 2010.

[A4] Christian Franz, Michael Czerner, and Christian Heiliger. Implementation of non-equilibrium vertex corrections in KKR: transport through disordered layers. *Journal of Physics: Condensed Matter*, 25(42):425301, 2013.

[A5] Christian Franz, Michael Czerner, and Christian Heiliger. Influence of the magnetic material on tunneling magnetoresistance and spin-transfer torque in tunnel junctions: *Ab initio* studies. *Physical Review B*, 88(9):094421, 2013.

[A6] Christian Franz, Marcel Giar, Markus Heinemann, Michael Czerner, and Christian Heiliger. Band structure and effective masses of $Zn_{1-x}Mg_xO$. In *Materials Research Society (MRS) Proceedings*, volume 1494. Cambridge University Press, 2013.

[A7] Christian Heiliger, Christian Franz, and Michael Czerner. *Ab initio* studies of the tunneling magneto-Seebeck effect: Influence of magnetic material. *Physical Review B*, 87(22):224412, 2013.

[A8] Christian Heiliger, Christian Franz, and Michael Czerner. Thermal spin-transfer torque in magnetic tunnel junctions. *Journal of Applied Physics*, 115(17):172614, 2014.

[A9] Jia Zhang, Christian Franz, Michael Czerner, and Christian Heiliger. Perpendicular magnetic anisotropy in CoFe/MgO/CoFe magnetic tunnel junctions by first-principles calculations. *Physical Review B*, 90(18):184409, 2014.

Acknowledgment

At this point, I would like to thank all the people who supported me in writing this thesis.

First of all, I would like to thank my supervisor Christian Heiliger for giving me the opportunity to write this thesis in his group. His experience with the topic and many discussions and proposals were the starting point of this work. Also I would like to thank him for providing facilities, financial support and the opportunity to attend many national and international conferences.

I would like to thank Andy Thomas for providing a report, and him and the other examiners in advance for attending the disputation.

I would like to thank Michael Czerner for introducing me to the NEGF method and for providing the KKR-code. Also I would like to thank him for providing some initial data (lattice structure, STT results for pure lead materials). Further, I would like to thank him and the HPC team, in particular Michael Feldmann and Marcel Giar, for keeping the HPC clusters skylla and yacana up and running, and the CSC team for granting me access to the fuchs cluster.

I would like to thank all members of the AG Heiliger for many discussions and the good time, in particular at the many traditional group activities.

I would like to thank all people from the I. Physikalisches Institut for pleasant atmosphere. Special thanks go to whoever is in charge of the coffee machine in the blue saloon for providing the vital caffeine supply.

I would like to thank my family and in particular my parents for their support and my sister Martina for the spell-checking.

I acknowledge funding from the Justus-Liebig-Universität Gießen via the postgraduate scholarship (Graduiertenstipendium), from the federal state of Hessen via the LOEWE-program, and from the Deutsche Forschungsgemeinschaft.

Eidesstattliche Erklärung

gemäß §17 Absatz 2 der Promotionsordnung der Gemeinsamen Kommission Naturwissenschaften für die Naturwissenschaftlichen Fachbereiche der Justus-Liebig-Universität Gießen vom 4. Februar 2005

Ich erkläre:
Ich habe die vorgelegte Dissertation selbständig und ohne unerlaubte fremde Hilfe und nur mit den Hilfen angefertigt, die ich in der Dissertation angegeben habe. Alle Textstellen, die wörtlich oder sinngemäß aus veröffentlichten Schriften entnommen sind, und alle Angaben, die auf mündlichen Auskünften beruhen, sind als solche kenntlich gemacht. Bei den von mir durchgeführten und in der Dissertation erwähnten Untersuchungen habe ich die Grundsätze guter wissenschaftlicher Praxis, wie sie in der "Satzung der Justus-Liebig-Universität Gießen zur Sicherung guter wissenschaftlicher Praxis" niedergelegt sind, eingehalten.

Gießen, den 21.12.2015

Christian Franz